รายงานวิจัยฉบับสมบูรณ์

โครงการ
การศึกษาวัสดุแม่เหล็กความถี่สูงที่ใช้ในวงจรแปลงผันกระแสตรงแบบ Dual active bridge สำหรับระบบแปลงผันกำลังไฟฟ้าในอนาคต

โดย ผู้ช่วยศาสตราจารย์ ดร.ศักดา สมกุล และคณะ

เมษายน 2563

MRG 6080051

รายงานวิจัยฉบับสมบูรณ์

โครงการ การศึกษาวัสดุแม่เหล็กความถี่สูงที่ใช้ในวงจรแปลงผันกระแสตรงแบบ Dual active bridge สำหรับระบบแปลงผันกำลังไฟฟ้าในอนาคต

คณะผู้วิจัย	สังกัด
ผศ.ดร.ศักดา สมกุล	มหาวิทยาลัยนเรศวร
รศ.ดร.วิบูลย์ ชื่นแขก	มหาวิทยาลัยเทคโนโลยีพระจอมเกล้าพระนครเหนือ
Prof.Dr.Toshiro Sato	Shinshu University, Japan

สนับสนุนโดยสำนักงานคณะกรรมการการอุดมศึกษา และสำนักงานกองทุนสนับสนุนการวิจัย

(ความเห็นในรายงานนี้เป็นของผู้วิจัย สกอ. และ สกว. ไม่จำเป็นต้องเห็นด้วยเสมอไป)

บทคัดย่อ

รหัสโครงการ : MRG 6080051

ชื่อโครงการ : **การศึกษาวัสดุแม่เหล็กความถี่สูงที่ใช้ในวงจรแปลงผันกระแสตรงแบบ Dual active bridge สำหรับระบบแปลงผันกำลังไฟฟ้าในอนาคต**

ชื่อนักวิจัย : **ดร.ศักดา สมกุล[1] รองศาสตราจารย์ ดร.วิบูลย์ ชื่นแขก[2]**
และ Professor Dr. Toshiro Sato[3]

[1]วิทยาลัยพลังงานทดแทนและสมาร์ตกริดเทคโนโลยี มหาวิทยาลัยนเรศวร อีเมล์ sakdaso@nu.ac.th
[2]ภาควิชาวิศวกรรมไฟฟ้าและคอมพิวเตอร์ มหาวิทยาลัยเทคโนโลยีพระจอมเกล้าพระนครเหนือ
อีเมล์ viboon.c@eng.kmutnb.ac.th
[3]Department of Electronics and Information Systems Engineering, Faculty of Engineering, Shinshu University, email: labyam1@shinshu-u.ac.jp

ระยะเวลาโครงการ : 4 เมษายน 2560 ถึง 3 เมษายน 2562

วงจรแปลงผันกำลังไฟฟ้ามีบทบาทสำคัญในการเชื่อมต่อแหล่งพลังงานทดแทนและอุปกรณ์สะสมพลังงานกับระบบโครงข่ายไฟฟ้า วงจรแปลงผันกำลังไฟฟ้ากระแสตรงแบบ Dual active bridge (DAB) เป็นวงจรที่มีลักษณะน่าสนใจโดยได้รับจากแวดวงนักวิจัยในช่วงสิบปีที่ผ่านมา เนื่องจากความสามารถในการส่งกำลังไฟฟ้าได้สองทิศทาง ประสิทธิภาพสูง มีการแยกกราวด์ และเชื่อมต่อกับระดับแรงดันไฟฟ้าที่มีความแตกต่างกันมากได้

โครงการวิจัยนี้เป็นการศึกษาการประยุกต์ใช้วัสดุแกนเหล็กแบบเทปผลึกนาโนสำหรับใช้ในหม้อแปลงไฟฟ้าความถี่สูงของวงจรแปลงผันกำลังไฟฟ้าแบบ DAB ขนาด1.1 kW สำหรับแรงดันไฟฟ้า 48V/400V และเปรียบเทียบกับวัสดุเฟอร์ไรต์ที่นิยมกันทั่วไป วงจรแปลงผันกำลังไฟฟ้าแบบ DAB ถูกออกแบบสำหรับใช้งานร่วมกับแบตเตอรี่สำหรับสะสมพลังงานในบ้านพักอาศัยที่มีแรงดันไฟฟ้าอยู่ในย่าน 42-54 V แกนเหล็กแบบเทปผลึกนาโนที่เลือกใช้มีรูปร่างแบบวงแหวนโทรอยด์และแกนตัดเป็นรูปตัวซีสำหรับสร้างหม้อแปลงไฟฟ้าพิกัด 1.2-kVA ที่มีระดับแรงดันไฟฟ้า 48V/400V และความถี่ 20 kHz และได้เลือกแกนขนาด EE65 วัสดุเฟอร์ไรต์ MnZn เบอร์ N87 สำหรับใช้ในการเปรียบเทียบ

จากผลการทดลองพบว่าหม้อแปลงที่สร้างจากแกนเหล็กแบบเทปผลึกนาโนตัดเป็นรูปตัวซีมีประสิทธิภาพอยู่ระหว่าง 98.4% ถึง 99.1% มีสัดส่วนกำลังไฟฟ้าต่อปริมาตรเท่ากับ 9 W/cm^3 และมีอุณหภูมิสูงสุด 71.0°C ส่วนแกนเหล็กแบบเทปผลึกนาโนรูปทรงวงแหวนโทรอยด์มีประสิทธิภาพอยู่

ระหว่าง 97.6% ถึง 99.2% มีสัดส่วนกำลังไฟฟ้าต่อปริมาตรเท่ากับ 12 W/cm3 และมีอุณหภูมิสูงสุด 60.1℃ ส่วนหม้อแปลงไฟฟ้าที่สร้างจากแกนเฟอร์ไรต์มีประสิทธิภาพอยู่ระหว่าง 97.6% ถึง 98.8% มีสัดส่วนกำลังไฟฟ้าต่อปริมาตรเท่ากับ 6 W/cm^3 และมีอุณหภูมิสูงสุด 78.5℃

แกนเหล็กแบบเทปผลึกนาโนมีกำลังไฟฟ้าสูญเสียที่ต่ำและมีความหนาแน่นของเส้นแรงแม่เหล็กที่สูงกว่าเฟอร์ไรต์จึงทำให้หม้อแปลงมีขนาดเล็กลงซึ่งยังส่งผลให้ค่ากำลังไฟฟ้าสูญเสียมีค่าลดลงเนื่องจากขนาดที่ลดลงของขดลวด แกนเหล็กแบบเทปผลึกนาโนตัดเป็นรูปตัวซีมีความเหมาะสมสำหรับใช้งานในวงจรที่มีกำลังไฟฟ้าสูงเนื่องจากมีประสิทธิภาพที่สูงและยังสร้างเป็นหม้อแปลงได้ง่ายกว่า

คำหลัก : วงจรแปลงผันกำลังไฟฟ้ากระแสตรง แม่เหล็กไฟฟ้าความถี่สูง สมาร์ทกริด

Abstract

Project Code : MRG 6080051

Project Title : Investigation of High-Frequency Magnetic Materials used in Dual Active Bridge DC-DC Converters for the Next-Generation Power Conversion System

Investigator : Dr. Sakda Somkun[1], Associate Professor Dr. Viboon Chunkag[2] and Professor Dr. Toshiro Sato[3]

[1]School of Renewable Energy and Smart Grid Technology, Naresuan University email: sakdaso@nu.ac.th

[2]Department of Electrical and Computer Engineering, King Mongkut's University of Technology North Bangkok, email: viboon.c@kmutnb.ac.th

[3]Department of Electronics and Information Systems Engineering, Faculty of Engineering, Shinshu University, email: labyam1@shinshu-u.ac.jp

Project Period : April 4, 2017 to April 3, 2019

Power electronic converters now play the important role in interfacing renewable energy sources and energy storage devices with the utility grid. Dual active bridge DC-DC converters are the most promising topology that gain attention from research communities in the past ten years due to their bidirectional power transfer capability, high efficiency, galvanic isolation and ease of voltage matching.

This project investigates applications of tape-wound nanocrystalline materials for construction of high frequency transformer cores of a 1.1-kW 48V/400V dual active bridge (DAB) DC-DC converter and compared with the commonly-used ferrite cores. This converter is designed for connecting a home battery storage with the input voltage ranges from 42 V to 54 V. to a constant DC bus voltage of 400 V. A toroidal core and cut C-cores of tape-wound nanocrystalline materials were chosen for construction of 48V/400V 1.2-

kVA 20-kHz transformers. A set of EE65 cores of MnZn N87 ferrite was selected for comparison.

The cut C-core nanocrystalline transformer has efficiency between 98.4% to 99.1% with the nominal power density of 9 W/cm^3. The maximum operating temperature of 71.0°C. The toroidal nanocrystalline transformer has the efficiency range of 97.6%-99.2%, the power density of 12 W/ cm^3 and the maximum operating temperature of 60.1°C. The efficiency range, power density and the maximum operating temperature of the ferrite transformer were found to be 97.6%-98.8%, 6 W/ cm^3, and 78.5°C respectively.

The tape wound nanocrystalline material not only reduces the core loss, but also decreases the copper loss due to smaller copper windings. Nanocrystalline cut C-cores is suitable for high power applications due to the increased efficiency and ease of transformer manufacturing.

Keywords : DC-DC converter, High-frequency magnetics, Smart grid

บทสรุปสำหรับผู้บริหาร (Executive Summary)

โครงการวิจัยนี้เป็นการศึกษาการประยุกต์ใช้วัสดุแกนเหล็กแบบเทปผลึกนาโนสำหรับใช้ในหม้อแปลงไฟฟ้าความถี่สูงของวงจรแปลงผันกำลังไฟฟ้าแบบ DAB ซึ่งเป็นวงจรจะถูกนำมาใช้อย่างกว้างขวางในระบบสมาร์ตกริด โดยแกนเหล็กแบบเทปผลึกนาโนที่เลือกใช้มีรูปร่างแบบวงแหวนโทรอยด์และแกนตัดเป็นรูปตัวซีสำหรับสร้างหม้อแปลงไฟฟ้าพิกัด 1.2-kVA ที่มีระดับแรงดันไฟฟ้า 48V/400V และความถี่ 20 kHz และได้เลือกแกนขนาด EE65 วัสดุเฟอร์ไรต์ MnZn เบอร์ N87 สำหรับใช้ในการเปรียบเทียบ

ผลจากการวิจัยพบว่าแกนเหล็กแบบเทปผลึกนาโนมีกำลังไฟฟ้าสูญเสียที่ต่ำและมีความหนาแน่นของเส้นแรงแม่เหล็กที่สูงกว่าเฟอร์ไรต์จึงทำให้หม้อแปลงมีขนาดเล็กลงซึ่งยังส่งผลให้ค่ากำลังไฟฟ้าสูญเสียมีค่าลดลงเนื่องจากขนาดที่ลดลงของขดลวด โดยแกนเหล็กแบบเทปผลึกนาโนตัดเป็นรูปตัวซีมีความเหมาะสมสำหรับใช้งานในวงจรที่มีกำลังไฟฟ้าสูงเนื่องจากมีประสิทธิภาพที่สูงและยังสร้างเป็นหม้อแปลงได้ง่ายกว่า

โครงการวิจัยนี้สามารถใช้เป็นข้อมูลให้กับอุตสาหกรรมอิเล็กทรอนิกส์สำหรับพลังงานทดแทนเพื่อใช้ในการนำเอาแกนเหล็กแบบเทปผลึกนาโนไปประยุกต์ใช้ในผลิตภัณฑ์รุ่นใหม่ ซึ่งปัจจุบันแกนเหล็กแบบเทปผลึกนาโนมีราคาที่ถูกลงจากผู้ผลิตในประเทศจีนและอินเดีย

กิตติกรรมประกาศ

คณะผู้วิจัยขอขอบพระคุณ สำนักงานกองทุนสนับสนุนการวิจัยและมหาวิทยาลัยนเรศวร ที่ได้ทุนสนับสนุน ทุนส่งเสริมนักวิจัยรุ่นใหม่ สำหรับโครงการวิจัยนี้ ซึ่งเป็นส่วนสำคัญในการพัฒนาองค์ความรู้ใหม่ สร้างผลงานตีพิมพ์ในวารสารวิชาการระดับนานาชาติ และใช้ประกอบการเรียนการสอนในและทำวิจัยในระดับบัณฑิตศึกษา

คณะผู้วิจัยขอขอบพระคุณ วิทยาลัยพลังงานทดแทนและสมาร์ตกริดเทคโนโลยี มหาวิทยานเรศวร ที่ได้สนับสนุนเวลาและสถานที่ รวมคณะผู้บริหารและเจ้าหน้าที่ฝ่ายสนับสนุนทุกท่าน ตลอดระยะเวลาดำเนินงานของโครงการวิจัยนี้

สุดท้ายนี้คณะผู้วิจัยขอขอบคุณครอบครับของคณะผู้วิจัยที่อยู่เคียงข้างและเป็นกำลังใจจนกระทั่งโครงการนี้สำเร็จลุล่วงด้วยดี

ศักดา สมกุล
วิบูลย์ ชื่นแขก
Toshiro Sato

Table of Contents

Chapter 1 Introduction 1

1.1 Introduction to the Research Problem and Its Significance 1

1.2 Objective 4

1.3 Scope of Research 5

Chapter 2 Basic Theory and Literature Review 6

2.1 Basic Operation of the Dual Active Bridge (DAB) DC-DC Converter 6

2.2 Topologies and Modulation Strategies of the DAB DC-DC Converter 13

2.3 High-frequency Magnetic Materials and Their Application in Power Electronic Converters 22

Chapter 3 Design of High Frequency Transformer and AC Inductor 24

3.1 High Frequency Transformer Design Methodology 24

3.2 AC inductor Design Methodology 29

3.3 Design of Transformer for the DAB DC-DC Converter 31

3.4 Design of Auxiliary Inductor for the DAB DC-DC Converter 40

Chapter 4 Experimental Results 44

4.1 No-load Tests of the Prototype Transformers 44

4.2 On-load Tests of the Prototype Transformers 52

4.3 Discussion 77

Chapter 5 Conclusion 80

Table of Contents

5.1 Conclusion of the Findings 80

5.2 Future Works 81

References 82

Chapter 1
Introduction

1.1 Introduction to the Research Problem and Its Significance

Wide spread adoption of renewable energy has transformed electrical generation and distribution systems into the distributed generation system [1]. Generation sites are located based on the availability of renewable energy resources, e.g. wind, solar, small hydro, together with the conventional centralized power plants, e.g. natural gas, coal, nuclear etc. Energy storage devices such as batteries, hydrogen-fuel cells, pumped hydro storage systems etc. are commonly used to overcome the intermittency such renewable energy sources [2]. Battery electric vehicles (BEVs) and plug-in hybrid electric vehicles (PHEVs) are also integrated into the electricity grid to utilize the cleaner renewable energy sources [3]. In addition, energy stored in the BEVs and PHEVs can be used to support the grid when the demand is greater than the generation and reactive power injection for voltage regulation with the so-called *vehicle to grid* (*V2G*) operation [4]. The Smart grid system has been introduced to cope with the uncertainties of demand response and the variable generation of renewable energy sources [5]. One of the key characteristics of the smart grid is to accommodate of all power generation and storage options [5]. Thailand is also aware of the global context in the renewable generation and smart grid. According to the alternative energy development plan (AEDP2015) [6], Thailand has set up a target that the share

of renewable energy in the electricity production should increase from 9.87% in 2014 to 20.11% in 2036. Thailand smart grid development plan (2015 - 2036) has been also launched to ensure energy security, to improve system reliability and power quality, and increase energy efficiency. Several smart grid pilot projects will be implemented throughout the country [7]. EGAT, MEA and PEA are the key players in this smart grid plan.

Power electronic converters now play the vital role in the modern electric generation and distribution systems [8, 9]. They are used to converse the AC variable voltage variable frequency (VVVF) sources/storages (wind, hydro, flywheel, etc.) and DC variable voltage (VV) sources/storages (photovoltaic, fuel cell, electrolyzer, battery etc.) to AC constant voltage constant frequency (CVCF), for delivering power to the utility grid. The most commonly used circuits are the voltage source AC-DC converters and DC-DC converters [10]. Among these, dual active bridge (DAB) DC-DC converters shown in Figure 1-1 are the most promising topology that gains attention from research communities. The basic principle is each bridge generates a square wave voltage to the transformer windings and the power transfer is controlled by the phase difference between the two voltage waveforms. The advantages of the DAB converters can be listed below [11]:

- Bidirectional power transfer capability
- Zero voltage switching (ZVS) operation for efficiency enhancement
- Galvanic isolation through the high-frequency transformer
- High power density with the AC-link high-frequency voltage through the high-frequency transformer
- Easy voltage matching via the transformer turn ratio
- Fault current is limited with the auxiliary/leakage inductor [12].

The DAB DC-DC converters are widely used in solid state transformers [13], on-board battery chargers of EVs and PHEVs [14], grid-connected battery converters [15], railway traction systems [16], power conditioner circuits for fuel cells [17] and photovoltaic modules with a high voltage step-up ratio [18], and uninterruptable power supplies [19]. Research on the DAB DC-DC converter can be mainly classified into three directions. First, control and modulation strategies have been developed so as to increase the efficiency and power factor of the high-frequency transformer [20-27]. The second approach is the application of wide-band gap semiconductor devices, mainly SiC MOSFET [28-30], as the power switches operating at a higher frequency in order to enhance the efficiency and power density. The third approach direction is development of topology variants such as multi-input isolated DC-DC converter [30, 31], or three-phase DAB DC-DC converter [10, 16, 32] for high power applications with low ripple currents.

The high-frequency transformer and auxiliary inductor are the key components of the DAB DC-DC converter along with the two bridges. Ferrite materials are commonly used in such transformers and inductors [17, 18, 20, 21]. Iron-based nanocrystalline materials with a higher saturation induction and lower loss were also used as the transformer cores of the DAB converters [15, 30]. Air-core inductors are commonly used in high power DAB DC-DC converters [16, 32]. Iron powder materials with higher saturation induction and lower permeability than the ferrite cores are also another choice for high-frequency inductors in power switching converters [33, 34], which was found to be more compact than the ferrite cores [34].

However, No direct comparison of high-frequency magnetic materials for the DAB converters has been made.

Thus, this project is to explore the applications of high-frequency materials for transformers and auxiliary inductors of the DAB DC-DC converters. Commercial and custom-made iron powder cores will used to construct the auxiliary inductors. Commercial nanocrystalline materials will selected for the transformers. Comparisons with the commonly used ferrites materials will be made. Lower losses and less core volumes lead to a higher efficiency and power density. This project is beneficial for the electronic, renewable energy and power transformer industry of Thailand. Knowledge obtained from this research can be transferred to the industry so that our local-made power converters can compete with the imported products.

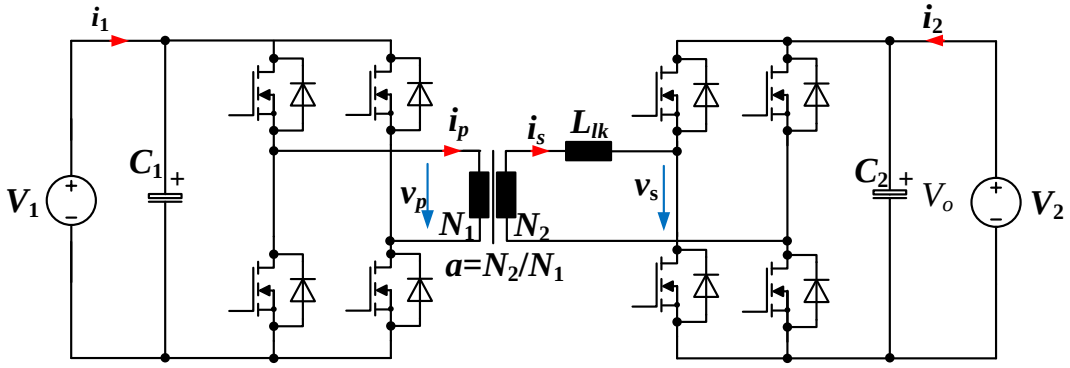

Figure 1-1 Dual active bridge DC-DC converter

1.2 Objective

This research is to investigate suitable high-frequency magnetic materials for inductors and transformers of a single-phase dual active bridge DC-DC converter in order to improve efficiency and power density.

1.3 Scope of Research

1) A single-phase DAB converter 1 kW with the voltage input of 42-52 V and output voltage of 360-400 V with the SPS and DPS modulations is used in this research.
2) The switching frequency of the DAB converter is 20 kHz.
3) High-frequency transformers will be constructed from commercial ferrite and nanocrystalline materials.
4) The auxiliary inductors will be built from commercial ferrite and iron powder materials.
5) Standard design methodologies based on product area (A_p) ad geometrical constant (K_g) will be used in designing the transformer and inductors.
6) Litz wires and interleaved windings will be used to minimize the skin effect and proximity effect.

Chapter 2

Basic Theory and Literature Review

2.1 Basic Operation of the Dual Active Bridge (DAB) DC-DC Converter

The DAB DC-DC converter was originally presented by De Doncker *et at* [11] as shown in Figure 2-1. For the most basic operation, so called the single phase shift (SPS) mode, each bridge generates a square wave voltage to the transformer windings. The circuit can be simplified by referring to the primary winding of the transformer as shown in Figure 2-2. So, the secondary side variables seen from the primary side can be written as follows

$$V_2' = \frac{V_2}{a} \tag{2-1}$$

$$v_s' = \frac{v_s}{a} \tag{2-2}$$

$$L_{lk2}' = L_{lk2}/a^2 \tag{2-3}$$

$$C_2' = a^2 C_2 \tag{2-4}$$

where $a = N_2/N_1$ is the transformer turn ratio. The inductance $L_{lkt} = L_{lk1} + L_{lk2}' + L_a$ is the total leakage inductance of the transformer with an auxiliary inductor L_a added to limit the maximum delivered power of the circuit. The voltage ratio between the two ports is defined by

$$d = \frac{V_2'}{V_1} = \frac{N_1}{N_2} \cdot \frac{V_2}{V_1}. \tag{2-5}$$

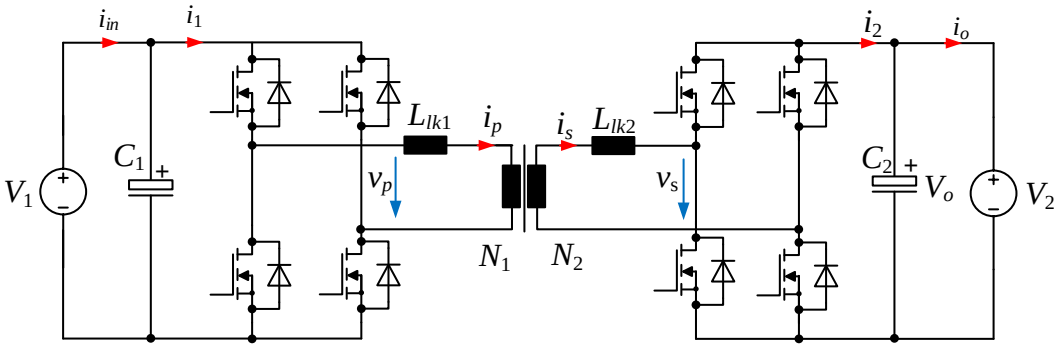

Figure 2-1 Dual active bridge DC-DC converter

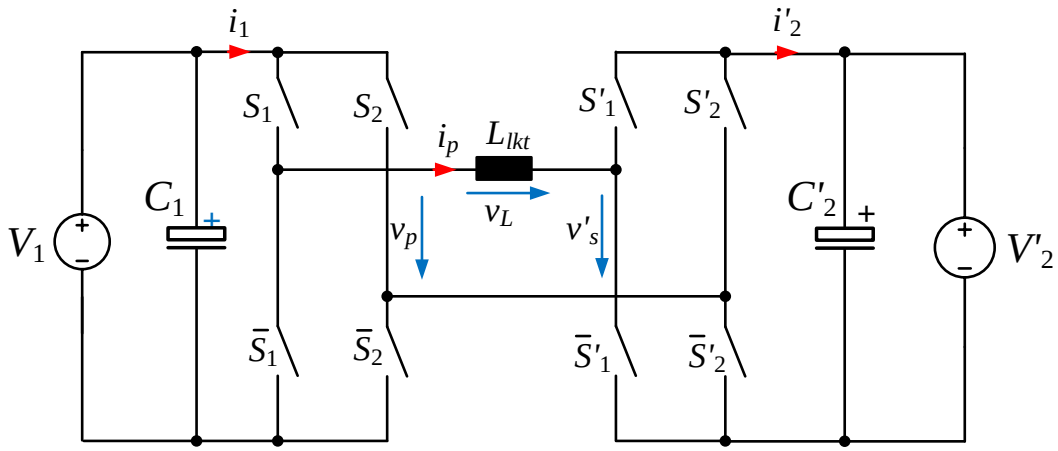

Figure 2-2 Simplified circuit diagram of the DAB DC-DC converter referred to the transformer primary winding

Figure 2-3 illustrates the primary voltage v_p, secondary voltage v_s', and the primary current i_p operating in the SPS modulation when $V_1 = V_2'$ $(d = 1)$. At $\theta = 2\pi f_s t = 0$, when the switches S_1 and $\bar{S}_2$ are turned on, the current $i_p(0) < 0$ does not flow through the MOSFETs of those two switches. However, the current i_p does flow through the anti-parallel diodes of the switches S_2 and $\bar{S}_1$. The current i_p starts to flow through the MOSFETs of S_1 and $\bar{S}_2$ when the current $i_p(0) > 0$. This operation is called the zero voltage switching (ZVS) techniques, which reduces loss in the MOSFET during the turn on transition. When $V_2' > V_1$ $(d > 1)$, $i_p(0)$ approaches zero as illustrated in Figure 2-4.

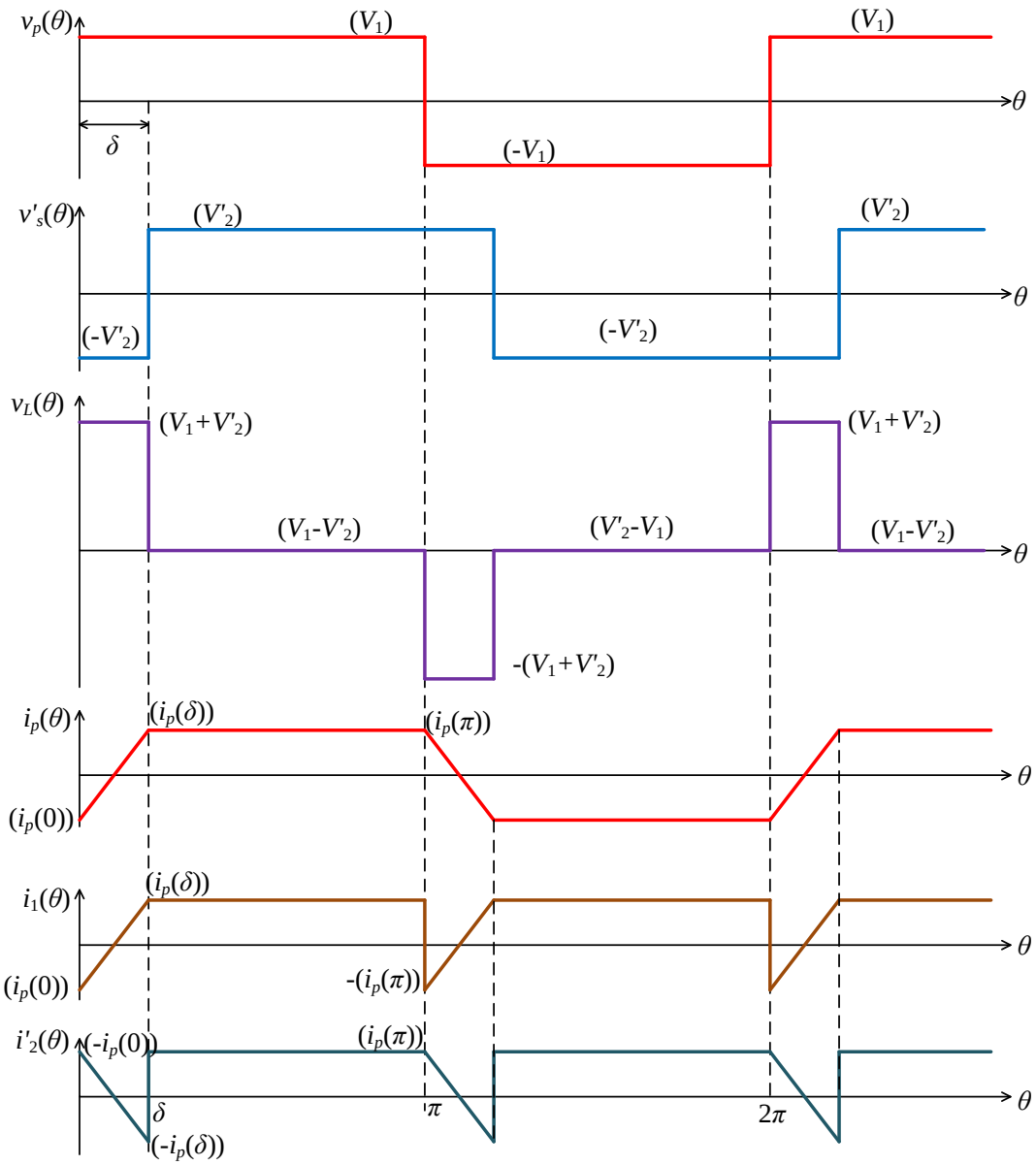

Figure 2-3 Key waveforms of the DAB DC-DC converter when $d = 1$.

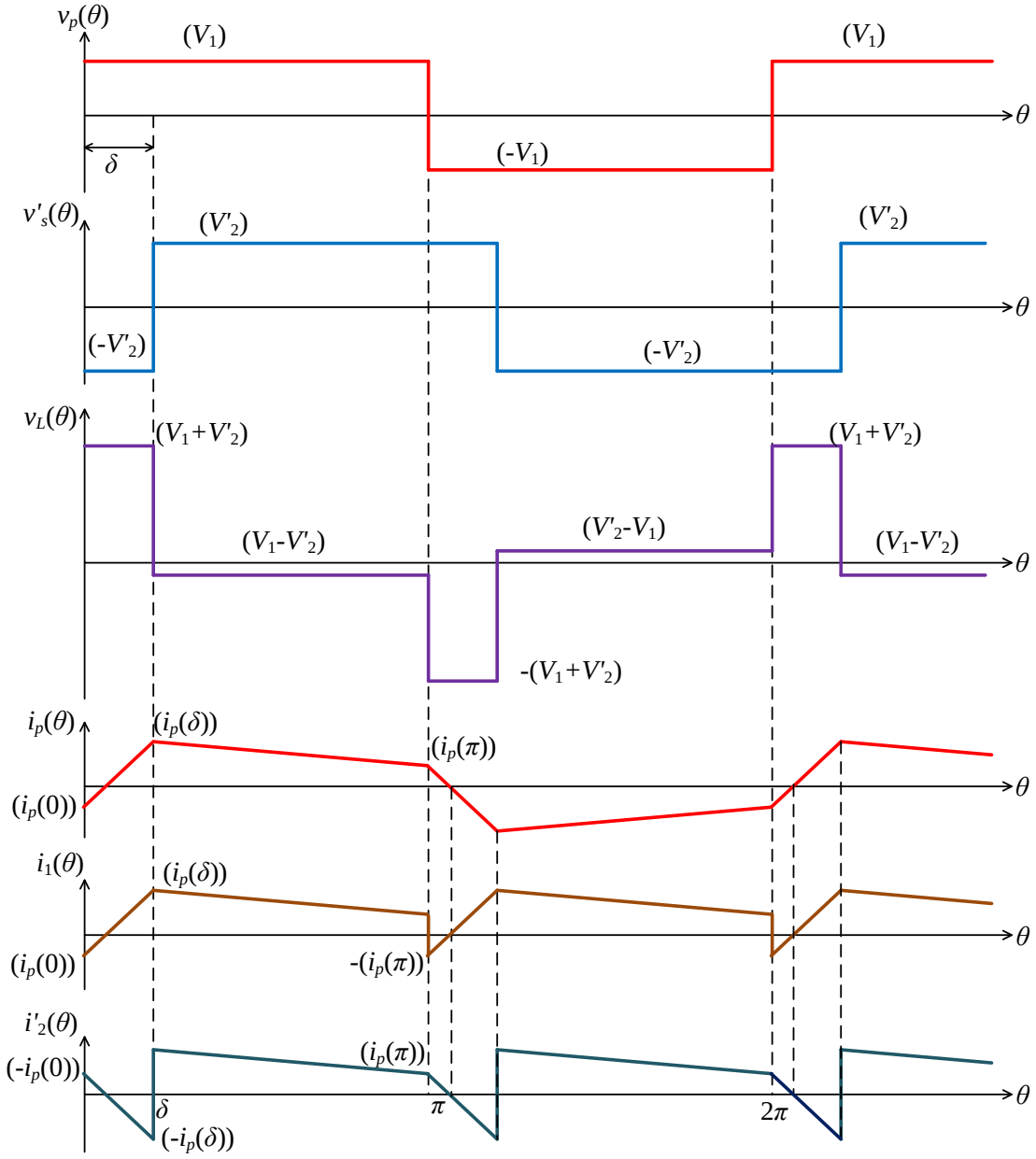

Figure 2-4 Key waveforms of the DAB DC-DC converter when $d > 1$.

In contrast, the current i_p at $\theta = \delta$ appraoches zero when $V_1 > V_2'$ $(d < 1)$. This results in the secondary bridge to operate as a diode bridge rectifier. Thus, it is important to keep $i_p(0) < 0$ and $i_p(\delta)>0$ so that the switching loss is minimized.

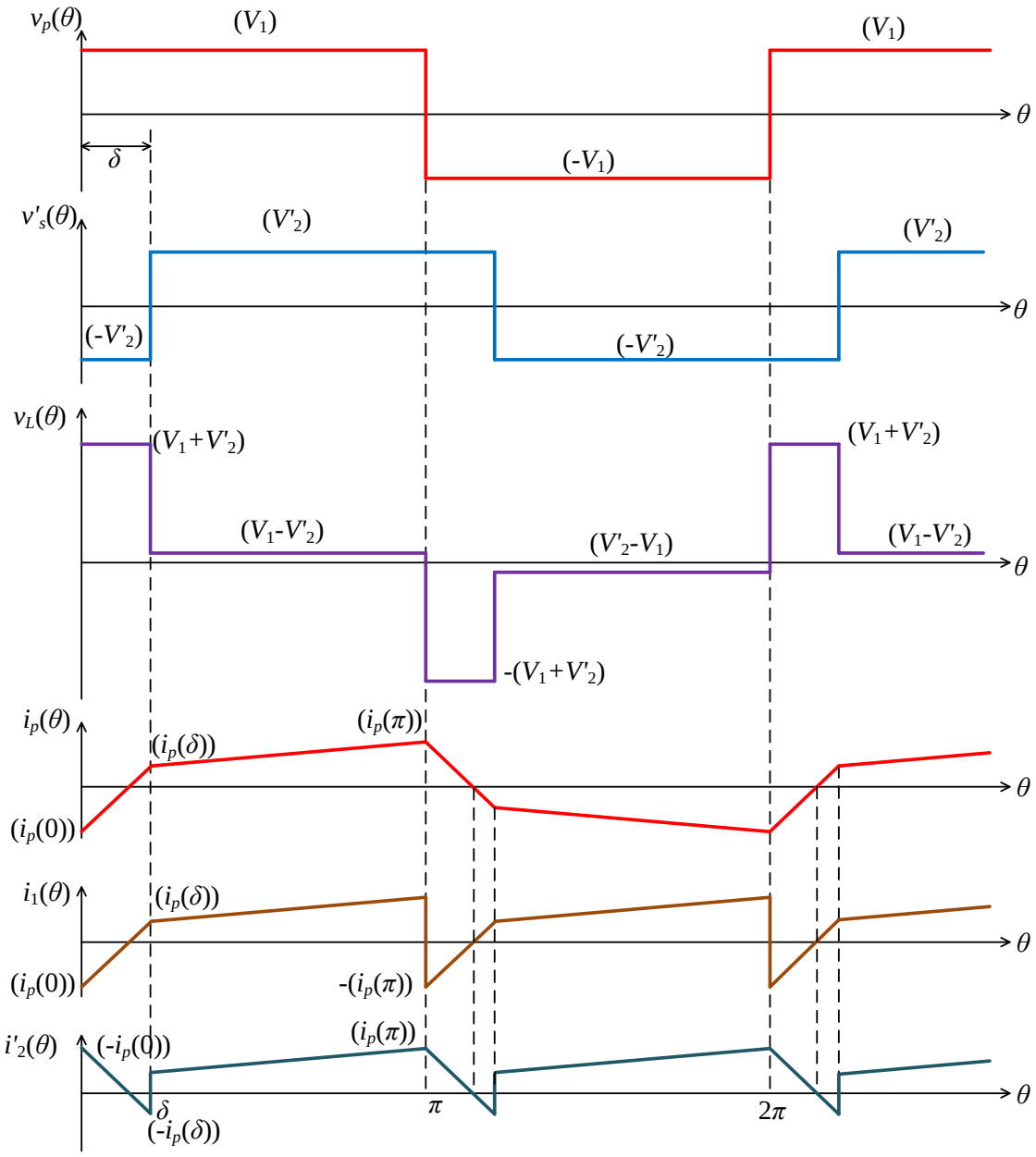

Figure 2-5 Key waveforms of the DAB DC-DC converter when $d < 1$.

The transferred power P_1 can be determined within a switching period as

$$P_1 = \frac{1}{2\pi}\int_0^{2\pi} v_p(\theta) i_p(\theta) d\theta. \qquad (2\text{-}6)$$

Assuming no loss occurs in the power switches, the transferred power P_1 can be written as

$$P_1 = \frac{V_1}{\pi}\int_0^{\pi} i_p(\theta) d\theta. \qquad (2\text{-}7)$$

The primary current $i_p(\theta)$ is defined as

$$i_p(\theta) = \begin{cases} \frac{(V_1+V_2')}{\omega_s L_{lkt}}\theta + i_p(0) & \text{for } 0 \le \theta < \delta \\ \frac{(V_1+V_2')}{\omega_s L_{lkt}}(\theta-\delta) + i_p(\delta) & \text{for } \delta \le \theta < \pi \end{cases}. \qquad (2\text{-}8)$$

Due to the symmetry in the current waveform, substituting $i_p(\theta) = -i_p(0)$ into (2-8) leads to

$$i_p(0) = -\frac{V_1}{\omega_s L_{lkt}}\left[d\delta + \frac{\pi(1-d)}{2}\right] \qquad (2\text{-}9)$$

$$i_p(\delta) = \frac{V_1}{\omega_s L_{lkt}}\left[\delta - \frac{\pi(1-d)}{2}\right] \quad . \qquad (2\text{-}10)$$

Using equations (2-8) to (2-10), the transferred power P_1 and the average input current of the DAB DC-DC converter are given as follows

$$P_1 = \frac{V_1 V_2'}{\omega_s L_{lkt}}\delta\left(1 - \frac{|\delta|}{\pi}\right) = \frac{dV_1^2}{\omega_s L_{lkt}}\delta\left(1 - \frac{|\delta|}{\pi}\right) \qquad (2\text{-}11)$$

$$I_1 = \frac{V_2'}{\omega_s L_{lkt}}\delta\left(1 - \frac{|\delta|}{\pi}\right) = \frac{dV_1}{\omega_s L_{lkt}}\delta\left(1 - \frac{|\delta|}{\pi}\right) \qquad (2\text{-}12)$$

Figure 2-6shows transferred power with the phase shift angle. This DAB DC-DC converter has a capability to transfer power in two directions. The ZVS boundaries

are plotted by solving $i_p(0) = 0$ in (2-9) and $i_p(\delta) = 0$ in (2-10). The voltage ratio between the two ports should be close to the transformer turn ratio ($d = 1$) to achieve to the ZVS operation especially at a light load.

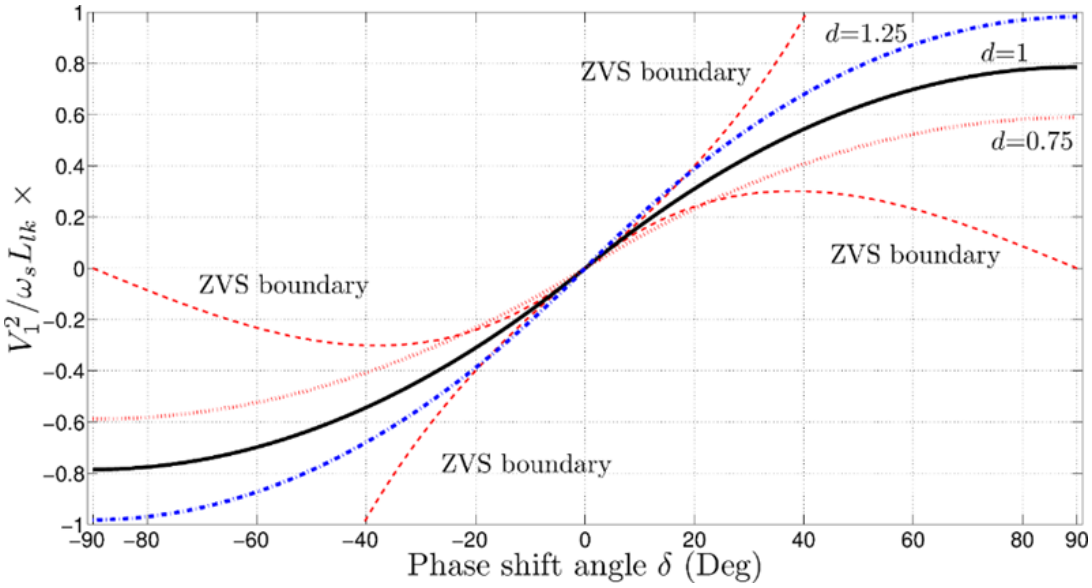

Figure 2-6 Transferred power with the phase shift angle

The RMS value of the current i_p is derived from

$$I_p = \sqrt{\frac{1}{\pi}\left(\int_0^{\delta} i_p^2(\theta)\, d\theta + \int_0^{(\pi-\delta)} i_p^2(\theta-\delta) d(\theta-\delta)\right)}. \qquad (2\text{-}13)$$

Substitute (2-9) and (2-10) in to (2-13) leads to

$$I_p = \sqrt{\frac{2}{3}\frac{\delta}{\pi} i_p(0) i_p(\delta) + \frac{1}{3}\left(i_p^2(0) - i_p(0) i_p(\delta) + i_p^2(\delta)\right)} \qquad (2\text{-}14)$$

The phase shift angle of $\delta = \pm\pi/2$ results in a full swing of the maximum power transfer. However, this will lead to a large RMS current in the transformer winding. Thus, the maximum phase shift is normally limited to be less than $\pm\pi/2$.

2.2 Topologies and Modulation Strategies of the DAB DC-DC Converter

Apart from the narrow ZVS operation range, the SPS modulation scheme also faces pure transformer utilization due to the circulating current in the auxiliary inductor [10, 11]. Thus, the pulse width of the primary and/or secondary voltages are adjusted to accommodate a wider voltage regime by adding a phase shift between two phase legs of each bridge in order to increase the ZVS range and reduce the circulating current. The pulse width modulation schemes of the single-phase DAB DC-DC converter can be summarized in Figure 2-7 and Figure 2-8. The extended phase shift (EPS) method varies the pulse width only in one side of the transformer [20-22], whereas the dual phase shift (DPS) [23, 24] and triple phase shift (TPS) schemes [25-27] adjust the pulse width of both primary and secondary voltages. The difference between the DPS and TPS methods is that the TPS method varies the pulse width of the two voltage sides independently, while the pulse width of the two sides are identical for the DPS scheme. It is noted the phase angle δ is also the main variable for the power transfer. In other words, the TPS is considered as the unified representation of the phase shift control for the single-phase DAB DC-DC converter. Although the TPS method gives the best performance among these modulation strategies, but it requires three control variables. Thus, the DPS scheme is considered to be optimal for a large scale implementation. The SPS method is simple and it is suitable for a narrow voltage range.

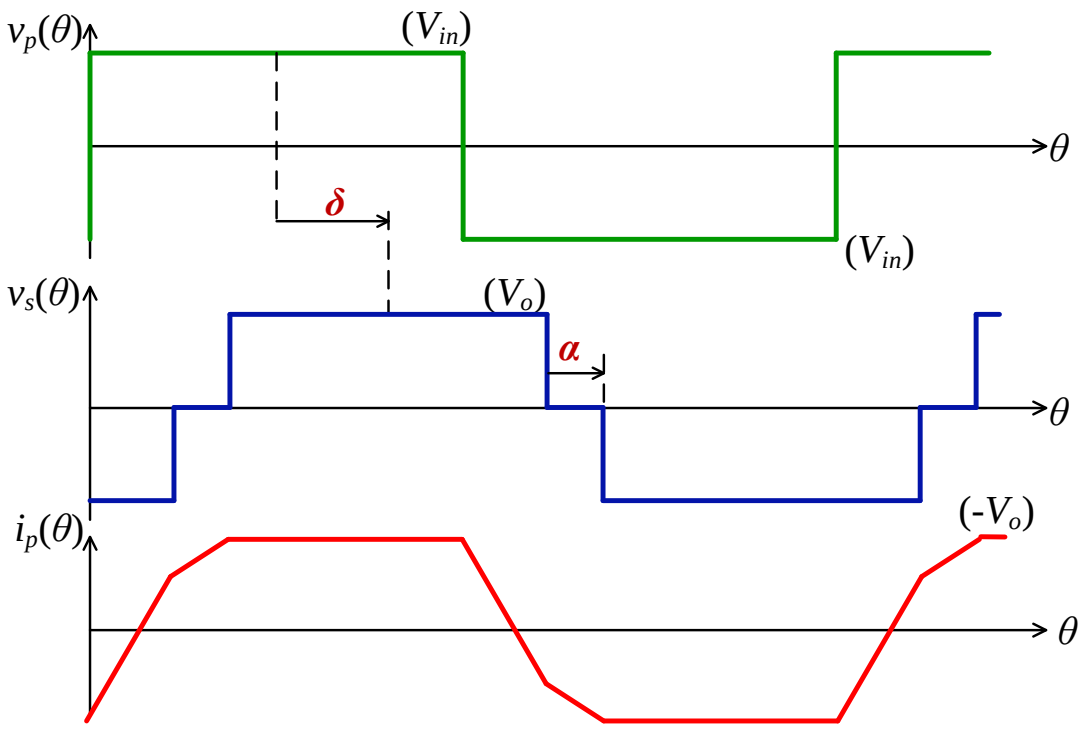

Figure 2-7 Extended phase shift modulation of the DAB DC-DC converter

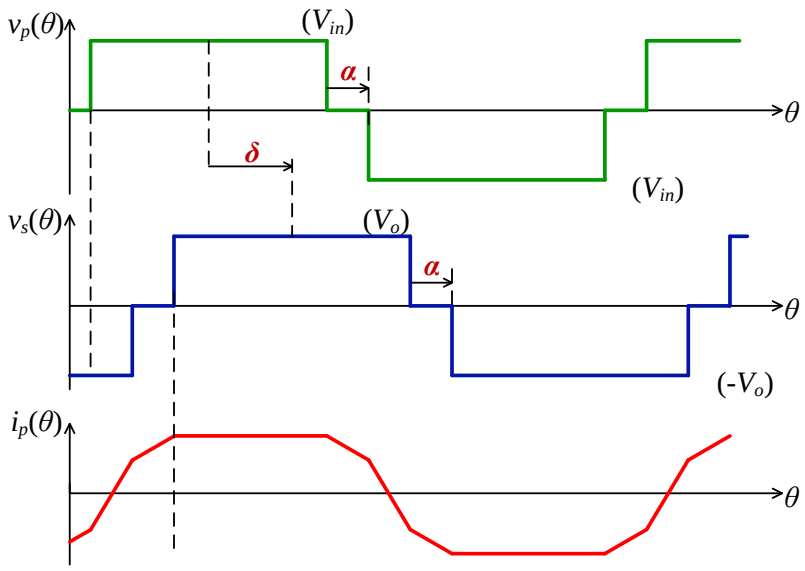

(a)

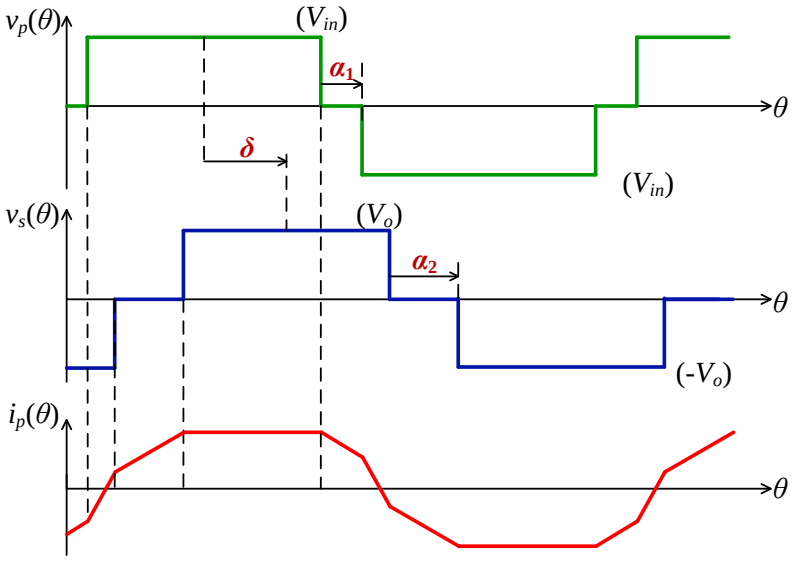

(b)

Figure 2-8 (a) Dual phase shift modulation, (b) Triple phase shift modulation of the DAB DC-DC converter

A third wining can be added to the transformer connected to another active bridge as shown in Figure 2-9 [31]. This topology is suitable for connecting a renewable energy source such as fuel cells or photovoltaic modules with the main DC bus and the third port is connected to an energy storage device such a battery. The advantages of this configuration are a compact structure due to the common use of a single transformer core, galvanic isolation, ease of voltage matching via the transformer turn ratios.

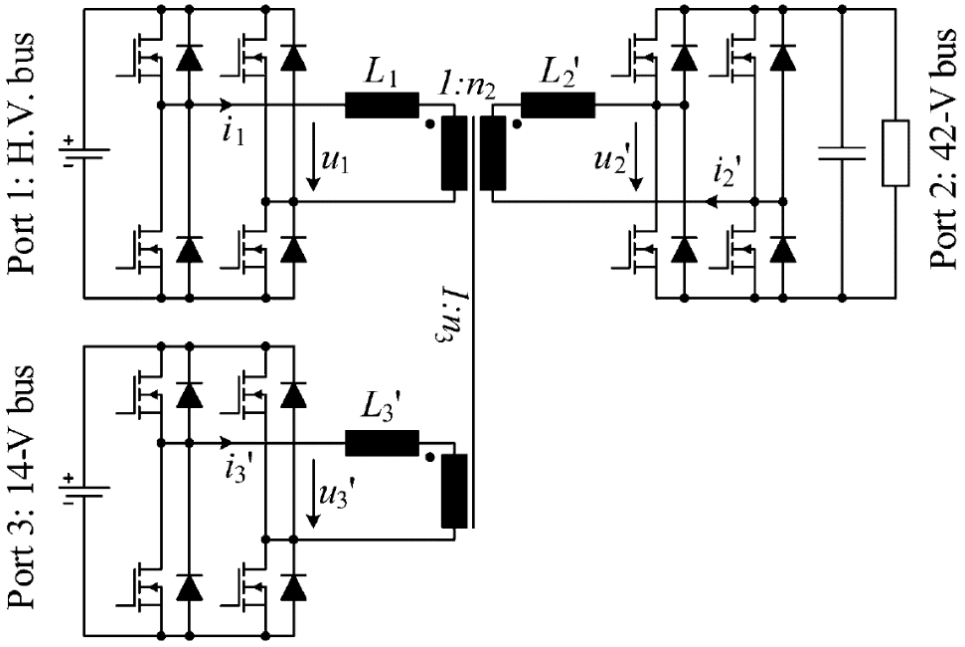

Figure 2-9 Triple active bridge DC-DC converter [18]

For high power applications, the DAB DC-DC converter can be implemented in the three-phase configuration as exhibited in Figure 2-10 [10, 16]. Each three-phase voltage source converter operates in the six-step mode and the power transferred is determined by the phase shift in each phase similar to the single-phase DAB converter. High power capability and lower component rating are the

advantages of this topology. Moreover, the ripple current in each bridge is lower resulting in smaller filter capacitors. A six-leg inverter can be used instead of the three-leg inverter as shown in Figure 2-11 which increases control degrees [32]. Moreover, the switches rating is reduced by half.

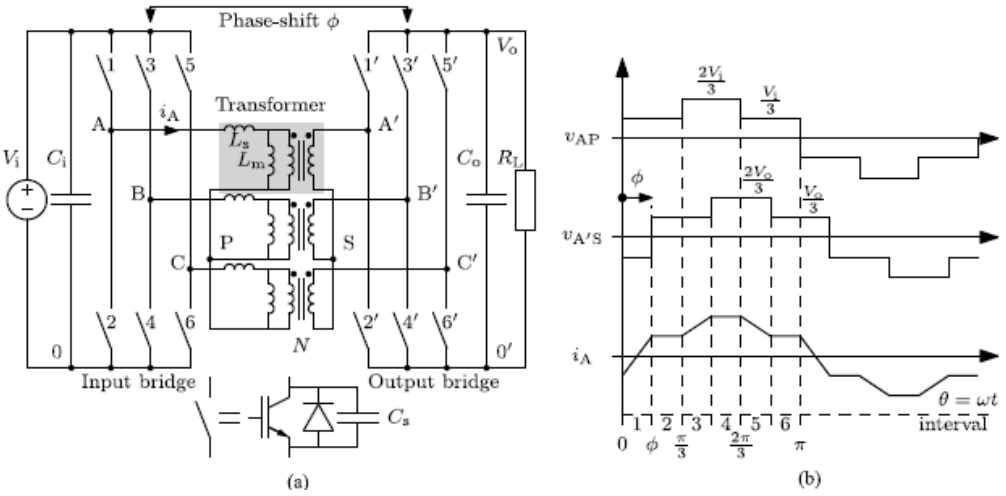

Figure 2-10 Three-phase DAB DC-DC converter and its ideal waveforms [16]

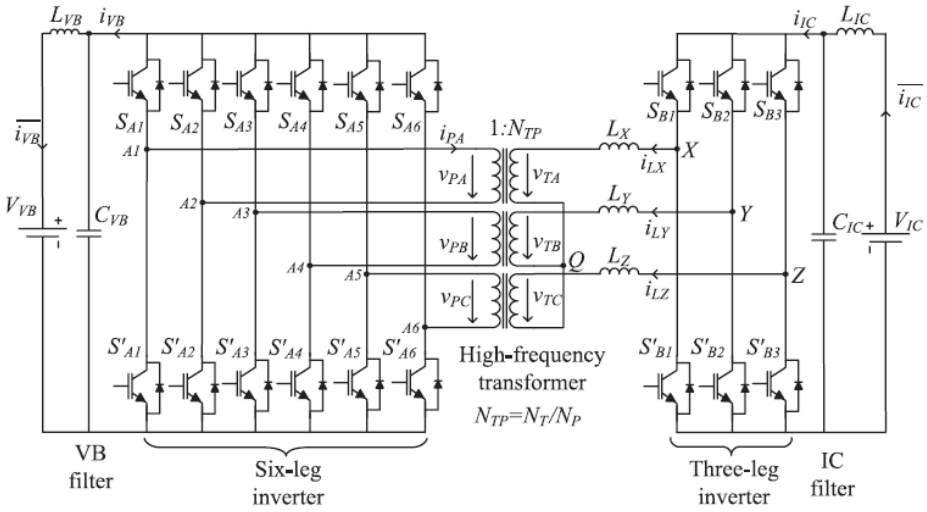

Figure 2-11 Six-leg three-phase DAB DC-DC converter [35]

2.3 High-frequency Magnetic Materials and Their Application in Power Electronic Converters

High-frequency magnetic materials used in the inductors of power electronic converters should exhibit low permeability so that a large amount of energy can be stored underneath the $B-H$ curve as illustrated in Figure 2-12 (green curve). Moreover, the width of the $B-H$ curve within a magnetizing period should be narrow to maintain low hysteresis loss. On the other hand, large permeability is desirable for the high-frequency transformers so that large energy will be transferred across via the induced magnetic flux in the core (blue curve). For the electrical engineering point of view, large permeability results in lower magnetizing current. Large saturation induction is preferred for higher power density.

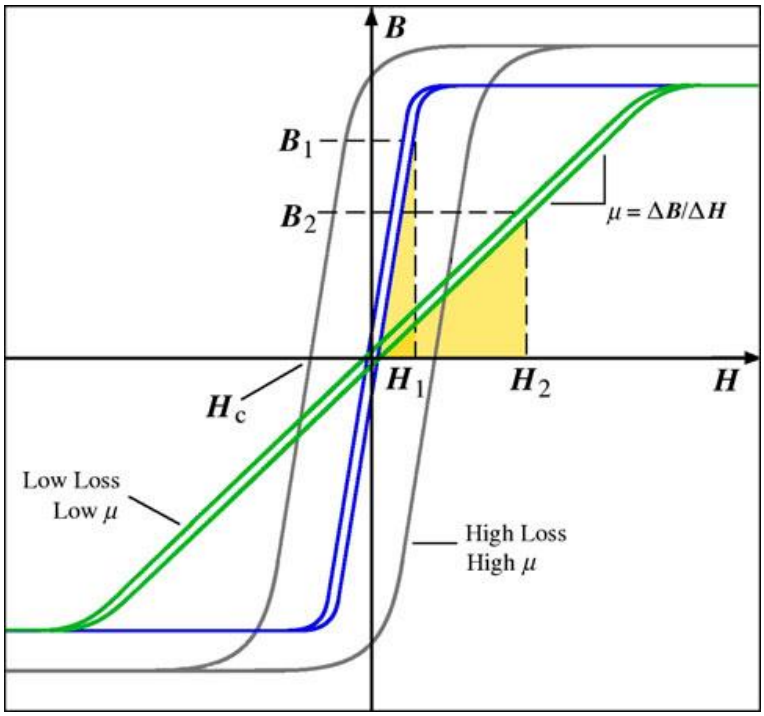

Figure 2-12 B-H characteristics of soft magnetic materials [36]

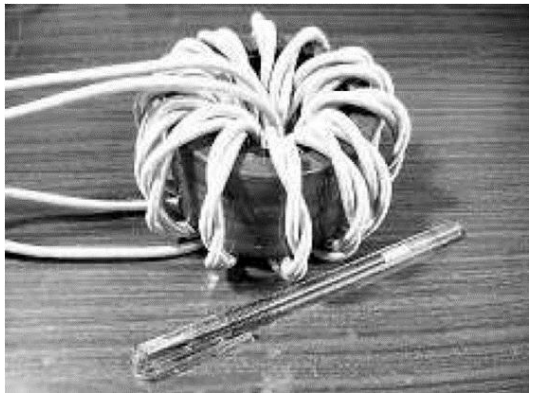

Figure 2-17 350-V 10-kVA and 20-kHz transformers for a DAB DC-Dc converter using FINEMET nanocrystalline toroid from Hitachi metal [39]

Table 2-1 compares the typical high-frequency materials used in power electronics converters. Ferrites are the most commonly used materials, which are made up of iron oxide (Fe_2O_3) mixed with other metals such as manganese (Mn), Zinc (Zn) etc. Ferrites in general have low Curie temperature. Thus, magnetic properties of ferrites vary with temperature significantly. For example, the saturation flux density of Epcos N87 MnZn material reduce from 0.49 T at 25°C to 0.39 T at 100°C. Core loss has a larger temperature dependent as depicted in Figure 2-13. Ferrites have relatively high permeability. Cut cores with air gap are normally used to construct a high-frequency inductor. However, poor manufacturing techniques greatly influence cut core properties and can lead to higher loss [36].

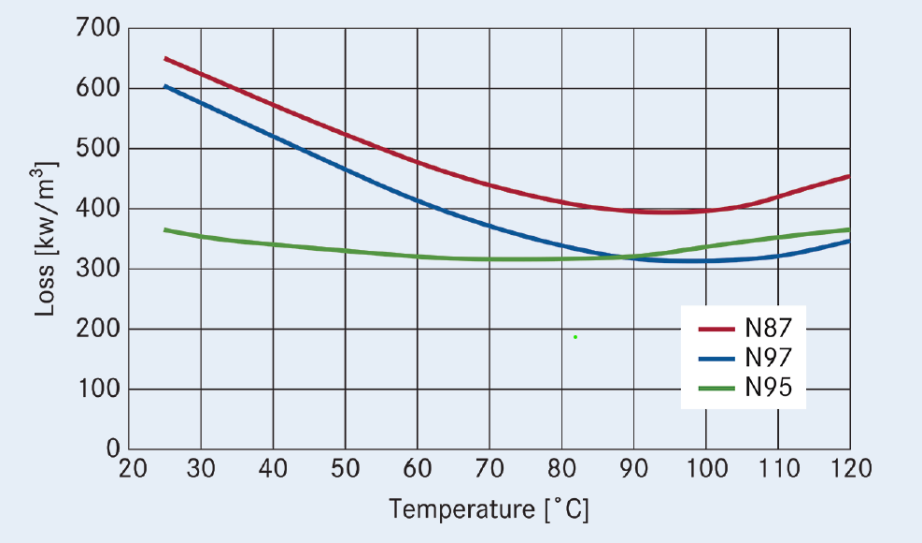

Figure 2-13 Loss variation with temperature of N87, N95 and N97 ferrites [37]

Iron powder materials are suitable alternatives for the high-frequency inductor cores [33]. They are manufactured from iron or iron alloy powder mixed or glued with an insulation material, then compressed into a ring or toroidal shape. The distributed gap causes low permeability, which is a function of powder size, spacing and chemical composition. Rafiq *et al* [34] compared inductors constructed from ferrite and iron powder cores of a 60-kW bidirectional DC-DC converter and found that the iron powder materials gave a lighter weight design than the ferrites with an insignificant difference in the converter efficiency.

Amorphous metal is produced by ultra-rapid quenching (about 1 million °C per second) of molten alloy which results in a non-crystalline structure as shown in Figure 2-14. This structure has no anisotropic properties due to a crystalline structure, and it has no crystalline grain boundaries to obstruct movements of magnetic domains. Thus, it exhibits high permeability and low loss with a high-saturation magnetic flux density. Iron-based amorphous metal materials are popular

power applications such as power transformers and filter inductors in power electronic converters [35].

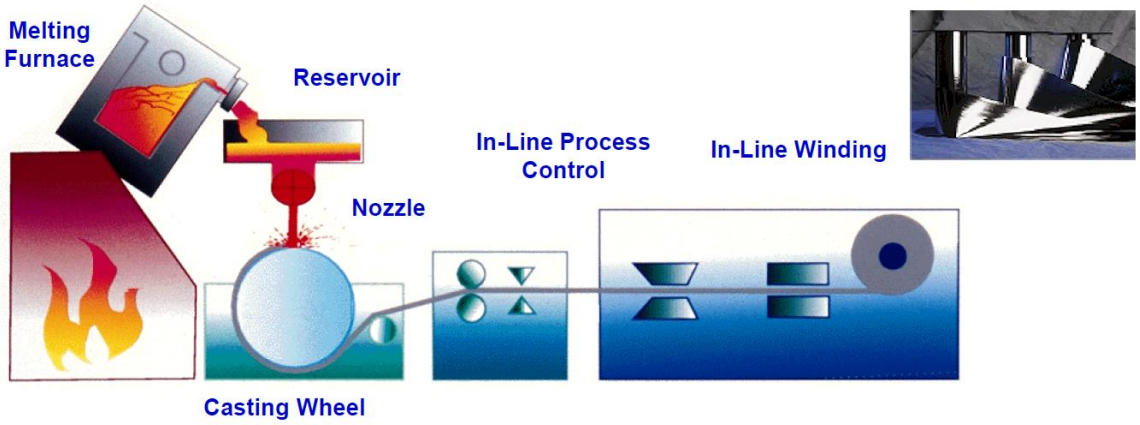

Figure 2-14 Schematic diagram of the production process of amorphous metal [38]

Nanocrystalline material is very close to amorphous metal. Amorphous ribbon of an FeSiB alloy, containing small additions of Nb and Cu, is casted by very rapid solidification with approximate 15-20μm thick as shown in Figure 2-15. After that, heat treatment is applied for crystallization with grain sizes of 10-20 μm. Their relative permeability is typically 20,000 and the saturation flux density is as high as 1.5 T. It exhibits a low eddy current. Their advantages over the ferrites are the saturation flux density up to 1.2 T and stable magnetic properties over a wide temperature range due to the Curie temperature up to 600°C. Nanocrystalline ribbon is wound into toroid and rectangular cores. Each layer is sandwiched by PET insulations as illustrated in Figure 2-16. They are suitable for high-frequency transformers up to 150 kHz. Example applications of nanocrystalline materials in the DAB DC-DC converters were illustrated in [15, 30, 39]. Figure 2-17 shows a 10-kVA 20-kHz transformer made from Hitachi FINEMET toroid [39].

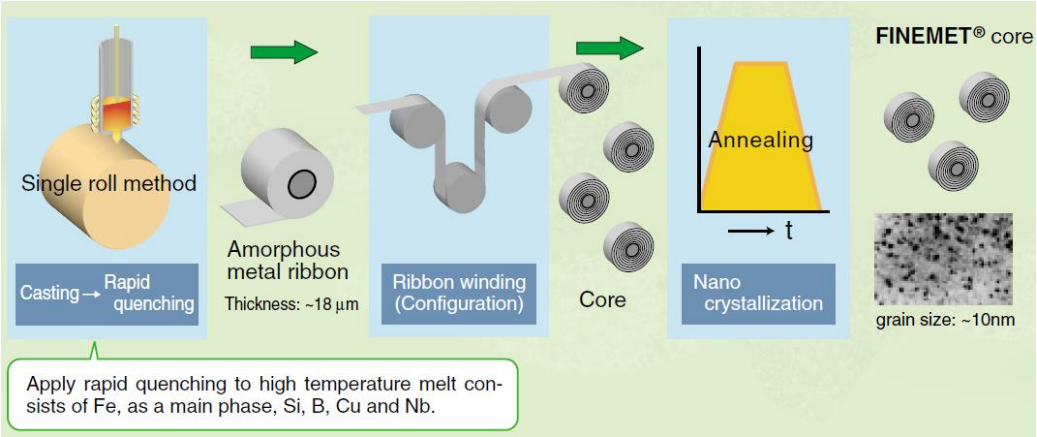

Figure 2-15 Production process of nanocrystalline materials [38]

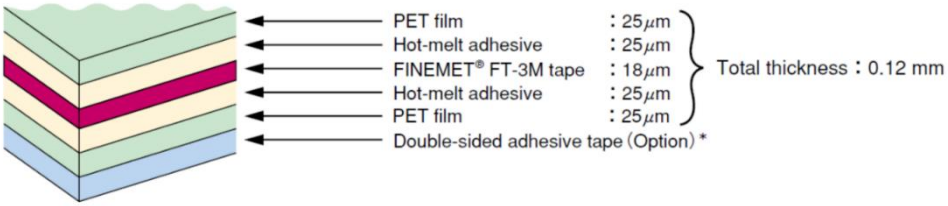

Figure 2-16 Structure of a nanocrystalline core [38]

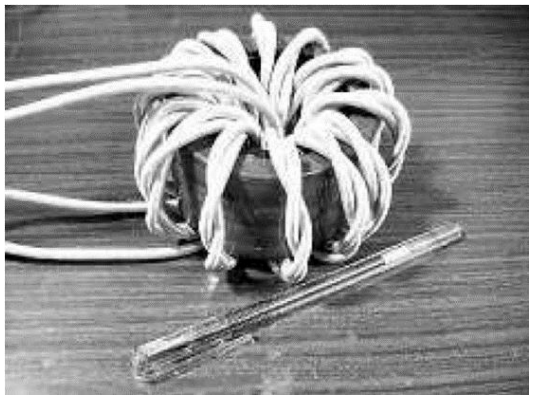

Figure 2-17 350-V 10-kVA and 20-kHz transformers for a DAB DC-Dc converter using FINEMET nanocrystalline toroid from Hitachi metal [39]

Table 2-1 Summary of high-frequency soft magnetic materials [40]

Materials	Ferrites	Nanocrystalline	Powdered iron	Amorphous metal
Model	Epcos N87	Vitroperm 500F	Micro-metals 75μ	Metglas 2605
Permeability, μ_i	2,200	15,000	75	5,000-10,000
$\hat{B}$ **, T**	0.49	1.2	0.6-1.3	1.56
P_{fe} **, W/cm³**	228 at 0.2T 50kHz	312 at 0.2 T 100 kHz	1032 at 0.2 T 10 kHz	294 at 0.2 T 25 kHz
Curie temp., °C	210	600	665	399

Chapter 3

Design of High Frequency Transformer and AC Inductor

3.1 High Frequency Transformer Design Methodology

In this research, the geometrical factor method K_g is selected for designing the transformer of the DAB DC-DC converter [41]. The transformer is considered to have k windings as shown in Figure 3-1. This K_g method is to determine the optimum peak magnetic flux density $\hat{B}_{opt}$ that minimizes the total loss in the transformer P_{tot}. The total loss is governed by the core loss P_{fe} and the copper loss P_{cu} as follow

$$P_{tot} = P_{fe} + P_{cu}. \tag{3-1}$$

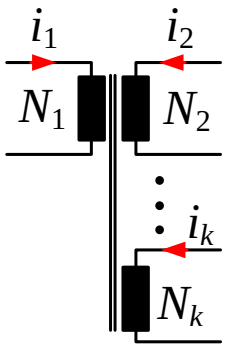

Figure 3-1 A transformer with k windings

Core loss P_{fe} is derived from the general Steinmetz equation given by

$$\frac{P_{fe}}{A_c l_m} = K_c f^{\alpha} \hat{B}^{\beta} \tag{3-2}$$

where K_c, α and β are the loss parameters of the core material, A_c is the core cross sectional area and l_m is the mean magnetic path length as illustrated in Fig. 8. At a given switching frequency of the DAB DC-Dc converter, the core loss P_{fe} is then simplified as

$$P_{fe} = K_{fe} \hat{B}^{\beta} A_c l_m \tag{3-3}$$

where $K_{fe} = K_c f_s^{\alpha}$.

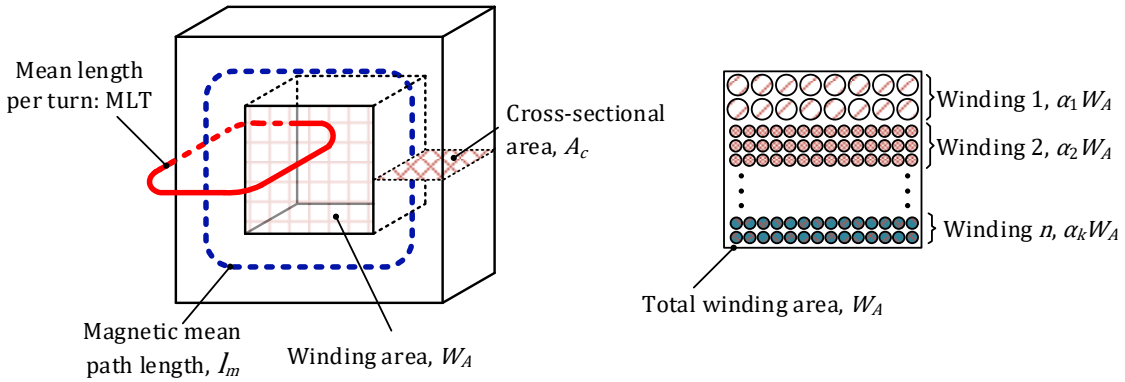

Figure 3-2 Transformer core geometry

Referring to the N_1 winding, the positive half of the voltage v_1 between t_1 to t_2 of an arbitrary waveform results in the flux density changing from $-\hat{B}$ to $\hat{B}$ as illustrated in Figure 3-3. Thus, the peak flux density can be obtained from

$$\hat{B} = \frac{\lambda_1}{2N_1 A_c} \tag{3-4}$$

where λ_1 is the flux linkage given by

$$\lambda_1 = \int_{t1}^{t2} v_1 dt. \tag{3-5}$$

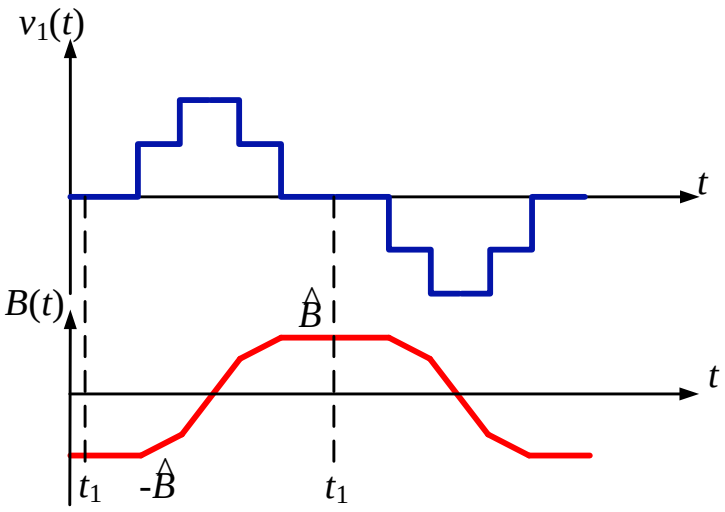

Figure 3-3 Induced voltage and flux density waveforms

The total copper loss in all the windings is given by

$$P_{cu} = \frac{\rho(MLT)N_1^2 I_{tot}^2}{W_A K_u} \tag{3-6}$$

where ρ is the resistivity of the copper wire, K_u is the fill factor and I_{tot} is the total RMS current referred to the N_1 winding given by

$$I_{tot} = \sum_{j=1}^{k} \frac{N_j}{N_1} I_1. \tag{3-7}$$

The primary turn number N_1 in (3-6) can be eliminated by substituting $N_1 = \frac{\lambda_1}{2\hat{B}A_c}$ from (3-4) into (3-6) so that the copper loss can be now expressed as

$$P_{cu} = \left(\frac{\rho\lambda_1^2 I_{tot}^2}{4K_u}\right)\left(\frac{MLT}{W_A A_c^2}\right)\left(\frac{1}{\hat{B}^2}\right) \tag{3-8}$$

Substitute (3-3) and (3-8) into (3-1) and set $dP_{tot}/d\hat{B} = 0$ to find the optimized value of $\hat{B}_{opt}$, which is given by

$$\hat{B}_{opt} = \left[\frac{\rho\lambda_1^2 I_{tot}^2}{2K_u}\frac{MLT}{W_A A_c^3 l_m}\frac{1}{\beta K_{fe}}\right]^{\left(\frac{1}{\beta+2}\right)}. \qquad (3\text{-}9)$$

Thus, the total power loss at the optimized flux density is given by

$$P_{tot} = (A_c l_m K_{fe})^{\left(\frac{2}{\beta+2}\right)}\left(\frac{\rho\lambda_1^2 I_{tot}^2}{4K_u}\frac{MLT}{W_A A_c^2}\right)^{\left(\frac{\beta}{\beta+2}\right)}\left(\left(\frac{\beta}{2}\right)^{-\left(\frac{\beta}{\beta+2}\right)} + \left(\frac{\beta}{2}\right)^{\left(\frac{\beta}{\beta+2}\right)}\right). \qquad (3\text{-}10)$$

Rearranging (3-10) yields

$$\frac{W_A(A_c)^{\frac{2(\beta-1)}{\beta}}}{(MLT)l_m^{2/\beta}}\left(\left(\frac{\beta}{2}\right)^{-\left(\frac{\beta}{\beta+2}\right)} + \left(\frac{\beta}{2}\right)^{\left(\frac{\beta}{\beta+2}\right)}\right)^{-\left(\frac{\beta}{\beta+2}\right)} = \left(\frac{\rho\lambda_1^2 I_{tot}^2 K_{fe}^{(2/\beta)}}{4K_u(P_{tot})^{\left(\frac{\beta}{\beta+2}\right)}}\right). \qquad (3\text{-}11)$$

The left-hand side term is composed of the core geometry, while the right hand side term depends on the electrical specification. Thus, the left term is defined as the geometry coefficient K_g given by

$$K_g = \frac{W_A(A_c)^{\frac{2(\beta-1)}{\beta}}}{(MLT)l_m^{2/\beta}}\left(\left(\frac{\beta}{2}\right)^{-\left(\frac{\beta}{\beta+2}\right)} + \left(\frac{\beta}{2}\right)^{\left(\frac{\beta}{\beta+2}\right)}\right)^{-\left(\frac{\beta}{\beta+2}\right)}. \qquad (3\text{-}12)$$

The selected core must have the geometry coefficient K_g larger than the electrical specification as below

$$K_g \geq \left(\frac{\rho\lambda_1^2 I_{tot}^2 K_{fe}^{(2/\beta)}}{4K_u(P_{tot})^{\left(\frac{\beta}{\beta+2}\right)}}\right). \qquad (3\text{-}13)$$

Equation (3-13) indicates that the core size is proportionally inverse with the power loss P_{tot} . In addition, the total RMS current I_{tot} has a great impact on the core size. After a core is selected, the parameters W_A, A_c, l_m and MLT are known. Then, the optimized $\hat{B}$ is evaluated using (3-9). The primary turn number N_1 is determined from

$$N_1 = \frac{\lambda_1}{2\hat{B}A_c}. \tag{3-14}$$

The turn numbers of the other windings are obtained from

$$\begin{aligned} N_2 &= N_1 \frac{V_2}{V_1} \\ N_3 &= N_1 \frac{V_3}{V_1} \\ &\vdots \end{aligned} \quad . \tag{3-15}$$

The winding area allocated to each winding is calculated from

$$\begin{aligned} W_{A1} &= \frac{N_1 I_1}{N_1 I_{tot}} W_A \\ W_{A2} &= \frac{N_2 I_2}{N_1 I_{tot}} W_A. \\ &\vdots \end{aligned} \tag{3-16}$$

Then, the cross-sectional areas of the copper wires are determined as follows

$$\begin{aligned} A_{w1} &= \frac{K_u W_{A1}}{N_1} \\ A_{w2} &= \frac{K_u W_{A1}}{N_2}. \\ &\vdots \end{aligned} \tag{3-17}$$

This core loss estimation used in the optimization is based on the general Steinmetz equation that is empirically obtained from sinusoidal excitations. The high frequency resistance due to the skin effect is also not considered. In practice, Litz wires are used for the transformer windings to minimize the skin effect and proximity

effect. Thus, the allowable power loss should have an additional margin to the losses caused by the non-sinusoidal flux density and the high frequency effects in the windings.

3.2 AC inductor Design Methodology

The design of the auxiliary inductor is adopted from the transformer design methodology. Only one winding is considered with an air gap in the core as shown in Fig. 10. The core size is determined from (3-13). The optimized flux density $\hat{B}$ and the turn number N are evaluated using (3-9) and (3-14) which is similar with the transformer design. The wire size is then calculated from

$$A_w = \frac{K_u W_A}{N}. \qquad (3\text{-}18)$$

The inductance is controlled by an air gap length which is then obtained from

$$l_g = \frac{\mu_0 A_c N^2}{L}. \qquad (3\text{-}19)$$

For a core with integrated air gap, the minimum A_L in [mH/1,000 turns] should be obtained as

$$A_L = \frac{L}{N^2} 10^9 \quad . \qquad (3\text{-}20)$$

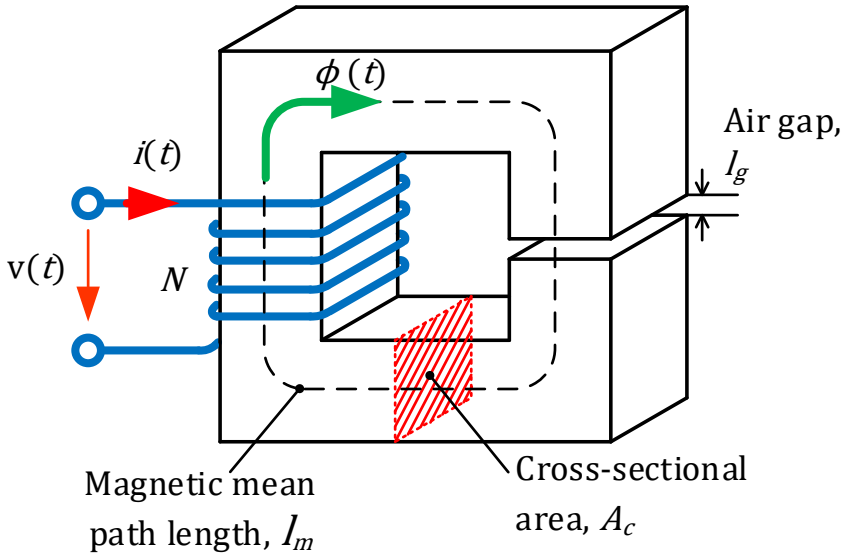

Figure 3-4 An inductor core geometry and construction.

3.3 Design of Transformer for the DAB DC-DC Converter

3.3.1 Electrical specifications

Figure 3-5 shows the DAB DC-DC converter under test. The input voltage ranges from 42V to 54V which is suitable for home battery storage. The maximum power is 1.1 kW at the nominal voltage with the nominal voltage of 48V. The maximum phase shift is limited at 60°. The secondary side feeds the 400-V DC bus voltage of the grid-connected inverter. This design considers the DAB DC-DC operates in the SPS modulation with the switching frequency of 20 kHz. Table 3-1 summarizes the electrical specifications for designing the transformer and the auxiliary inductor.

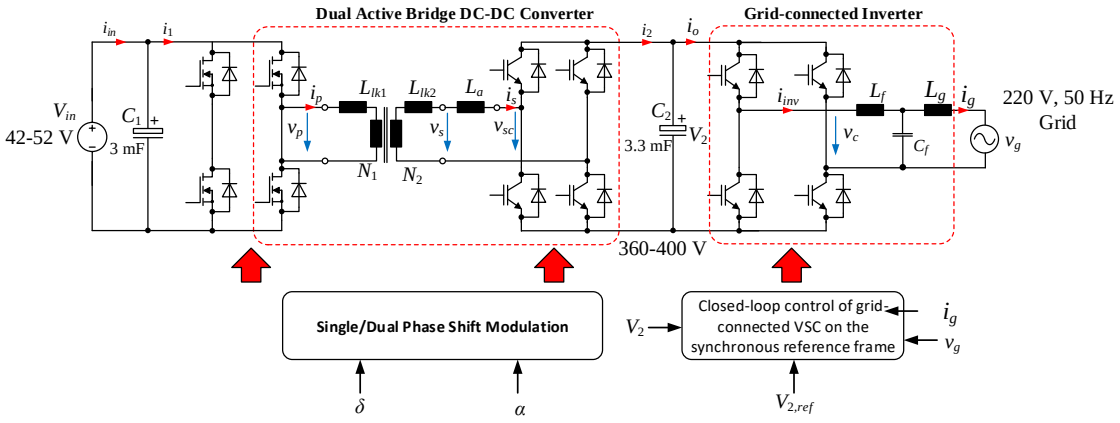

Figure 3-5 DAB DC-DC converter under test

Table 3-1 Electrical specifications of the DAB DC-DC converter

Parameters	**Formulas**	**Values**
Switching frequency, f_s	-	20 kHz
Nominal input voltage, $V_{in,norm}$	-	48 V
Maximum input voltage, $V_{in,max}$	-	54 V
Minimum input voltage, $V_{in,min}$	-	42V
Nominal output voltage, V_2	-	400V
Transformer turn rations	$V_2/V_{in,norm}$	400V/48V = 8.333
Maximum phase shift, δ_{max}	-	60º
Maximum power, $P_{1,max}$		1.1 kW at $V_{in,norm}$ and δ_{max}
Total leakage inductance L_{lkt} referred to the primary winding	$\frac{(nV_{in,norm})^2}{2\pi f_s P_{1,max}}\delta_{max}\left(1-\frac{\lvert\delta_{max}\rvert}{\pi}\right)$	808 µH
Maximum primary winding volt-second, $\lambda_{1,max}$	$\frac{V_{in,max}}{2\times f_s}$	0.0014 V·s
Nominal primary RMS current	Eq. (2-14) $V_1 = V_{in}, norm$ and $\delta = \delta_{max}$	30.32 A
Nominal secondary RMS current	$I_2 = (N_1/N_2)I_1$	3.64 A
Nominal total RMS current (referred to the primary side)	$I_{total} = I_1 + (N_2/N_1)I_2 = 2I_1$	60.64 A

3.3.2 Selected core materials

Amorphous, ferrite and nanocrystalline materials are considered in this study. Table 3-2 summarizes key properties of the selected materials. Figure 3-6 and Figure 3-7 compare the loss density and specific power loss the core materials with peak flux density $\hat{B}$ at 20 kHz using the general Steinmetz equation in (3-3). It can be observed that the nanocrystalline materials Hitachi Finemet and Vitroperm500F from VACUUMSCHMELZE GmbH are the best materials for frequency range below 100 kHz. However, the two materials are not widely available for a small order and difficult to find in the retails. The Amorphous Metglass from Hitachi metal is not selected in this study as it has the highest core loss due to its largest parameter α among the considered materials. The amorphous metal is more suitable for inductor applications with majority flux density is DC or line frequency AC waveforms, where the core loss is neglected compared with the copper loss. The nanocrystalline materials from the china-based manufacturer King Magnetics and from the US-based company MK magnetics are then used as alternative options for this study as its loss density and specific power loss under 100 kHz is still lower than the TDK N87 ferrite as shown in Figure 3-8 and Figure 3-9.

Table 3-2 Parameters of potential magnetic materials

Properties	**Amorphous Metglass AMCC series [38]**	**Ferrite TDK N87 [42]**	**Nanocrystalline King Magnetics [43]**	**Nanocrystalline Vitroperm500F [44]**	**Nanocrystalline Finemet [45]**	**Nanocrystalline MK magnetics [46]**
Peak flux density	1.56 T	0.39 T	1.25 T	1.2 T	1.23 T	1.2 T
Coercivity	2.0 A/m	21 A/m	1.2 A/m	Not given	Not given	Not given
Initial permeability	5,000	2,200	80,000	10,000	10,000	Not given
Power loss	2.2 W/cm^3 at 100 kHz 0.2 T	- 0.057 W/cm^3 at 25 kHz 0.2 T 100ºC - 0.375 W/cm^3 at 100 kHz 0.2 T 100ºC	- 0.0247 W/cm^3 at 20 kHz 0.2 T - 0.2175 W/cm^3 at 20 kHz 0.5 T - 0.29 W/cm^3 at 50 kHz 0.3 T	- 0.809 W/cm^3 at 100 kHz 0.3 T	- 0.0044 W/cm^3 at 10 kHz 0.1 T	- 0.0885 W/cm^3 at 20 kHz 0.2 T
Physical density	7,590 kg/m^3	4,850 kg/m^3	7,250 kg/m^3	7,350 kg/m^3	7,300 kg/m^3	7,300 kg/m^3
Steinmetz parameter, β	1.74	2.1	2.38	2.08	2.14	2.10
Steinmetz parameter, α	1.81	1.36	1.64	1.8	1.70	1.44
Steinmetz parameter, K_c [W/(m^{3}Hz$^\alpha$T$^\beta$)]	0.053	1.766	0.101	0.091	0.003	0.6472

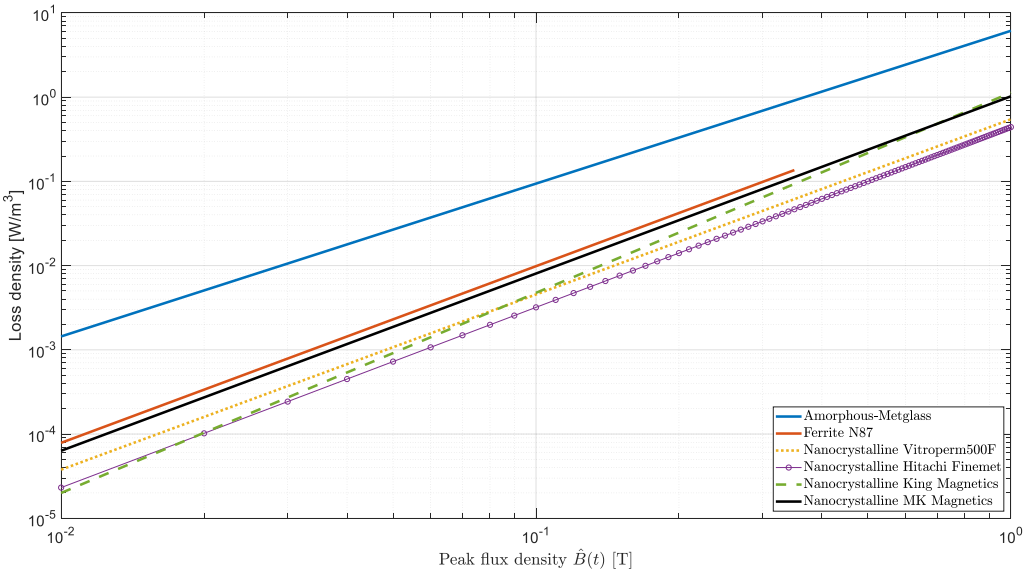

Figure 3-6 Loss density of different magnetic materials with the peak flux density at 20 kHz

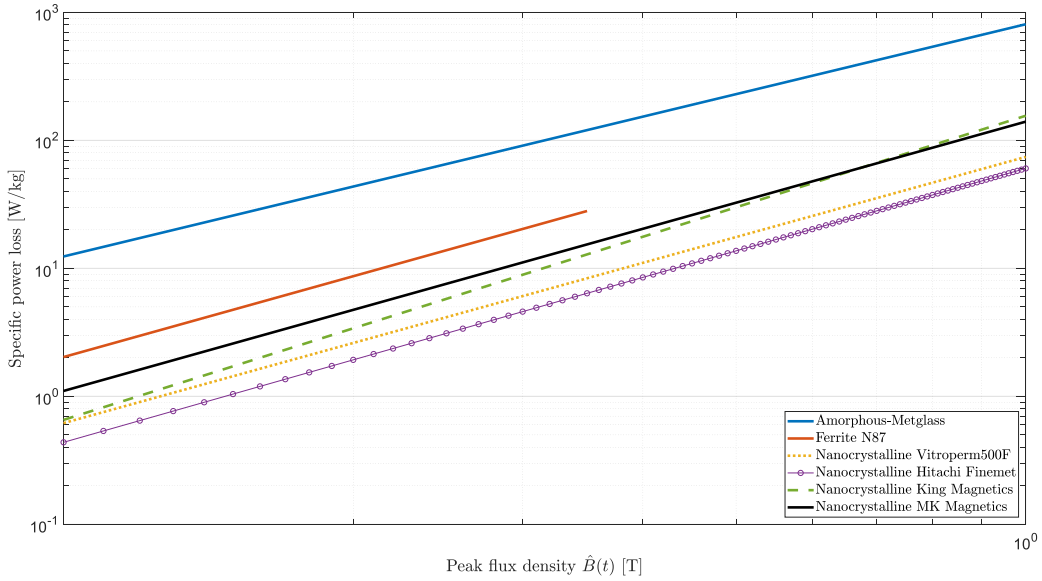

Figure 3-7 Specific power loss of different magnetic materials with the peak flux density at 20 kHz

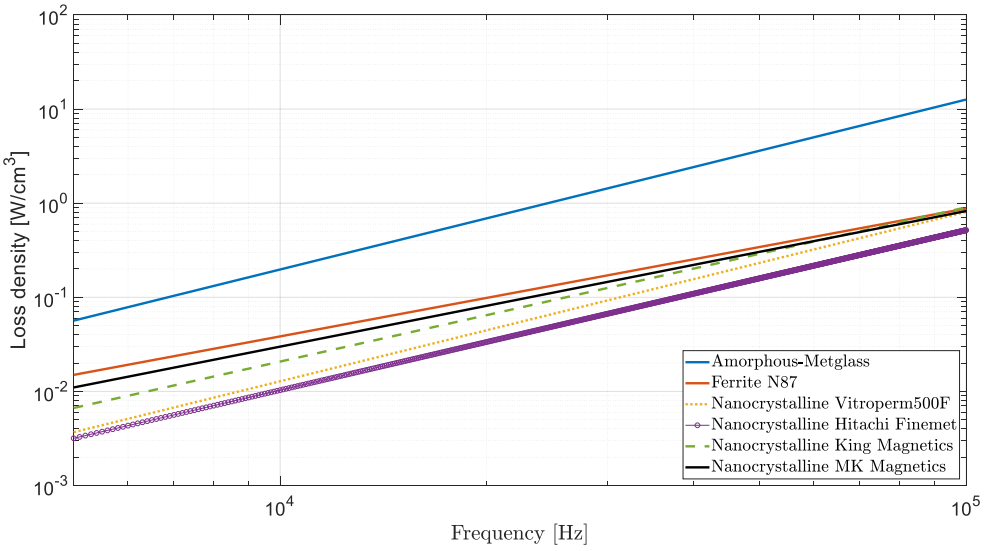

Figure 3-8 Loss density of different magnetic materials with the magnetizing frequency at 0.3 T

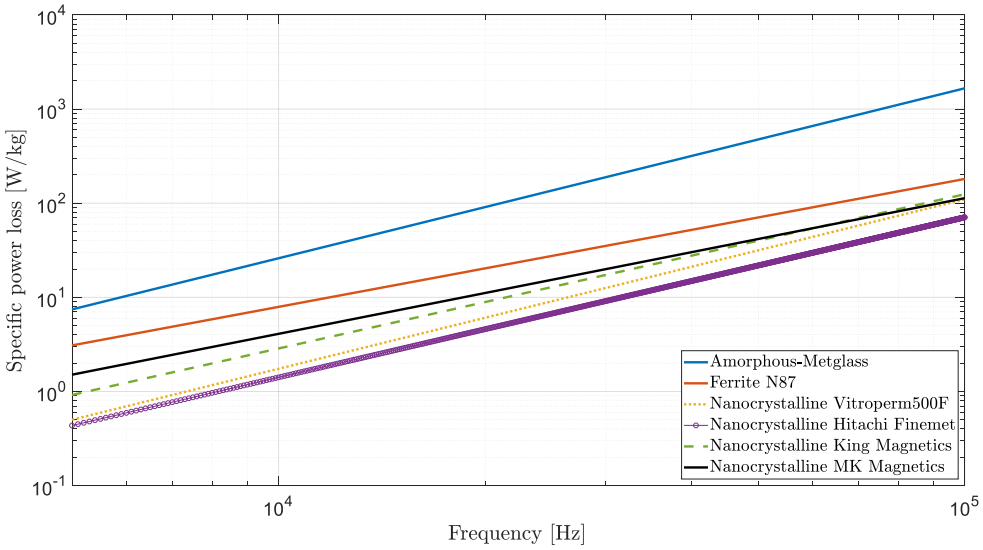

Figure 3-9 Specific power loss of different magnetic materials with the magnetizing frequency at 0.3 T

3.3.3 Prototype transformers

Three prototype transformers were designed and constructed. The core materials are the TDK N87 ferrite, King Magnetics nanocrystalline and MK magnetics, which were selected due to availability. Served Litz wires assembles from AWG36 and AWG40 conductors were used in the windings with the fill factor $K_u = 0.35$. The maximum peak flux density at $V_{in,max} = 54$ V was limited to 50% of the saturation flux density as given in Table 3-2. The maximum allowable power loss at the nominal input voltage of 48 V was 10 W, which is 0.91% of the rated power. Table 3-3 summarizes the parameters of the three prototype transformers, denoted as Transformer A to Transformer C. The ferrite transformer A has the largest core volume $A_c l_m = 77.8$ cm^3, while the toroidal nanocrystalline transformers B has the smallest core volume. Core loss, copper loss and total loss of each transformer was estimated using during the design stage. The ferrite transformer A is expected to have the poorest efficiency and power density.

Figure 3-10 illustrates winding configurations of the prototype transformers. The ferrite transformer A has the largest winding are W_A so that the interleaved winding configuration can be applied. This results in lower magnetomotive force (MMF) which is a cause of the proximity effect loss.

Figure 3-11 shows the photograph of the prototype transformer. The physical sizes of transformers B and C including the windings are not significantly smaller than transformer A. In fact, the shell type structure of transformers A and C are more compact because the windings are partially enclosed by the core. The estimated copper losses of the nanocrystalline transformers B and C are higher than the ferrite transformer A due to the available wire sizes are smaller than the optimum sizes.

The leakage inductance referred to the secondary winding of each transformer must know accurately identified which will be used to design the auxiliary inductance. The primary magnetizing inductance and the total leakage inductance referred to the secondary winding is determined by using an electrochemical impedance spectroscopy (EIS) machine Metrohm Autolab as shown in Figure 3-12 to generate a constant Ac current of 700 μA with the frequency range of 0.1 Hz to 100 Hz feed to the winding to be tested. After that an RL circuit was used to find the best fit with the measured impedance.

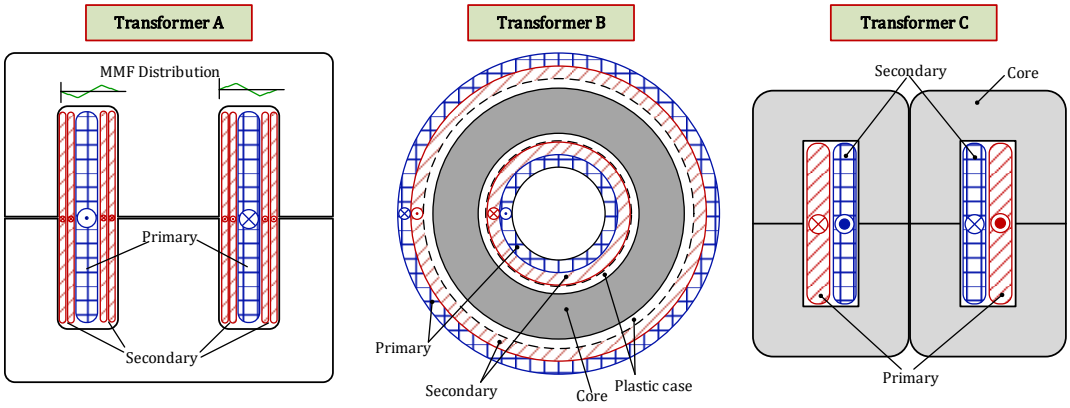

Figure 3-10 Winding configuration of the prototype transformers

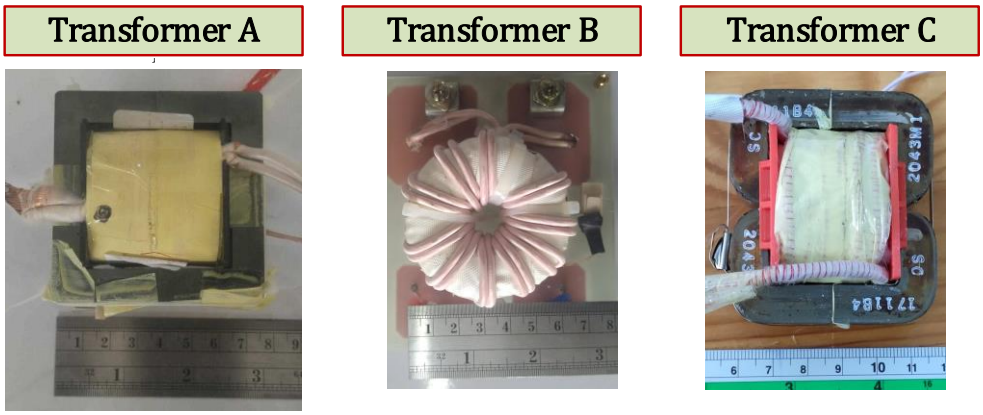

Figure 3-11 Photograph of the prototype transformers

Table 3-3 Parameters of the prototype transformers

Parameters	Transformer A	Transformer B	Transformer C
Material	Ferrite N87	Nanocrystalline King Magnetics	Nanocrystalline MK Magnetics
Core structure	EE65	Toroid KMN503220T	2 sets of SC2043M1
Total core area, A_c	5.29 cm^2	1.4 cm^2	3.12 cm^2
Magnetic length, l_m	14.7 cm	12.9 cm	12.8 cm
Primary winding	6 turns 2 in parallel of (500xAWG40)	10 turns 2 in parallel of (265xAWG36)	7 turns (800xAWG40)
Secondary winding	50 turns 2 in parallel of (40xAWG36)	83 turns (128xAWG40)	59 turns (128xAWG40)
$\hat{B}$ at 48V/54 V	0.19 T / 0.21 T	0.43 T / 0.48 T	0.27 T / 0.31 T
Est. P_{cu} at 48V/54 V	3.3 W / 4.8 W	4.0 W / 5.8 W	3.8 W / 5.5 W
Est. P_{fe} at 48V/54 V	6.7 W / 9.2 W	2.7 W / 3.6 W	2.7 W / 3.5 W
Est. P_{tot} at 48V/54 V	10.0 W / 15.0 W	6.7 W / 9.4 W	6.5 W / 9.0 W
Primary magnetizing inductance	0.26 mH	5.46 mH	0.16 mH
Total leakage inductance referred to the secondary winding	22 µH	43 µH	9 µH

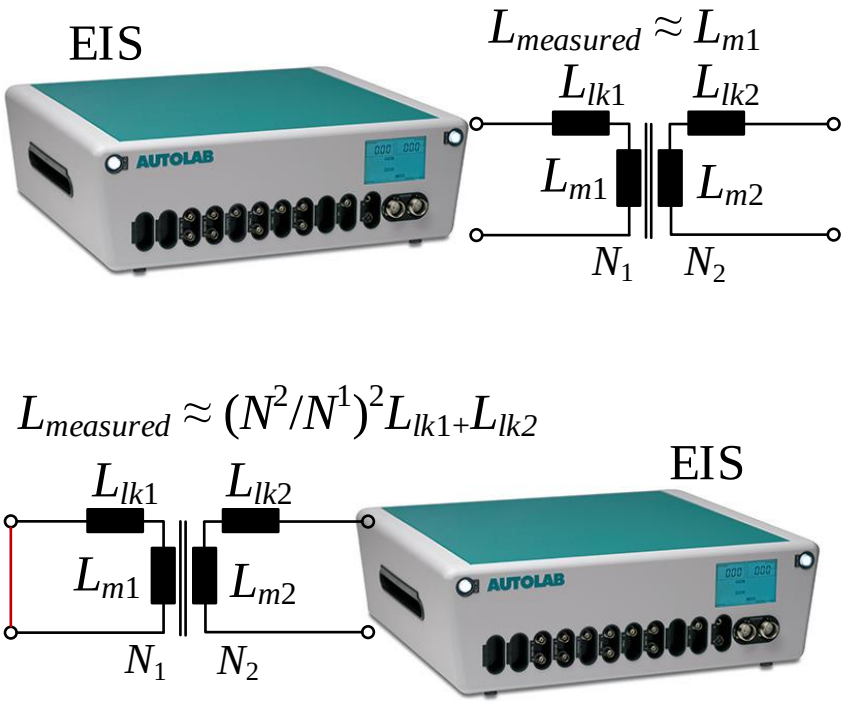

Figure 3-12 Determination of magnetizing inductance and leakage inductance

3.4 Design of Auxiliary Inductor for the DAB DC-DC Converter

According to Table 3-1 Electrical specifications of the DAB DC-DC converter, the total inductance $L_{lkt} = 808$ μH referred to the secondary winding is required to satisfy the power transfer of 1.1 kW at δ_{max}. In this experimental setup, the voltage of the secondary bridge is regulated at $V_2 = 400$ V, while that of the primary bridge varies from $V_{in,min} = 42$ V to $V_{in,max} = 54$ V. Observing from Figure 2-3 to Figure 2-5, the maximum volt-second across the total inductance L_{lkt} occurs when $d < 1$ as illustrated in Figure 3-13. Thus, the volt-second λ_1 across the auxiliary inductor L_a required in (3-13) is determined at $V_{in,max}$ as follows

$$L_a = L_{lkt} - L_{lk1} - L_{lk2} \tag{3-22}$$

$$v_{La}(t) = \frac{L_a}{L_{lkt}} v_L(t) \tag{3-23}$$

$$\lambda_1 = \left[\left(nV_{in,max} \right) \frac{\delta_{max}}{2\pi} T_s + \left(nV_{in,max} - V_2 \right) \frac{\left(\frac{\pi}{2} - \delta_{max} \right)}{2\pi} T_s \right] \cdot \frac{L_a}{L_{lkt}}. \tag{3-24}$$

The RMS current of the inductor is the same current of the secondary current of the transformer given in Table 3-1. Transformer A requires auxiliary inductance of 786 uH to ensure the transferred power of 1.1 kW at 48V. Transformer B has a larger leakage inductance which requires an extra auxiliary inductance of 765 μH. Transformer C has the smallest leakage inductance, which can be connected with both auxiliary inductors. The N87 ferrite and the nanocrystalline material from MK magnetics were selected for construction of the auxiliary inductors due to core availability. Table 3-4 lists the key parameters for the auxiliary inductors and Fig. 24 shows the photograph of the auxiliary inductors.

The inductance values were determined by using the EIS machine with the same method as that of the transformers. The air gap of each inductor was slightly

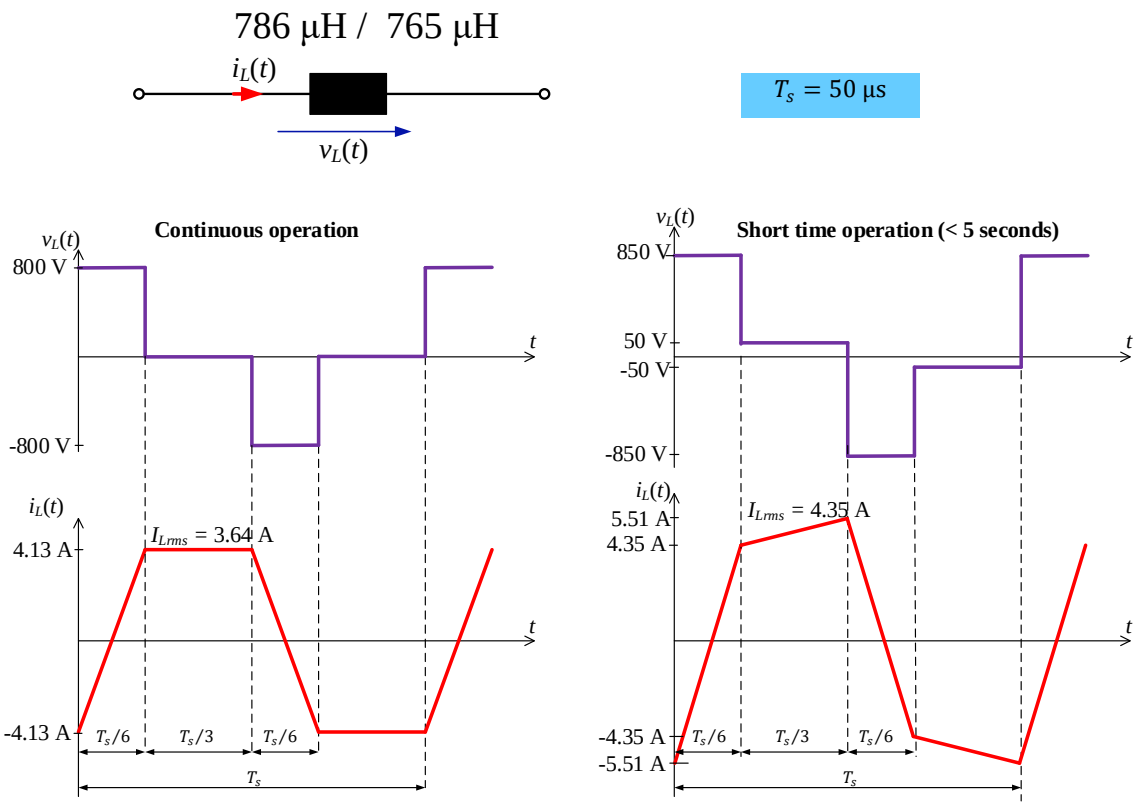

Figure 3-13 Voltage and current waveforms across the inductor

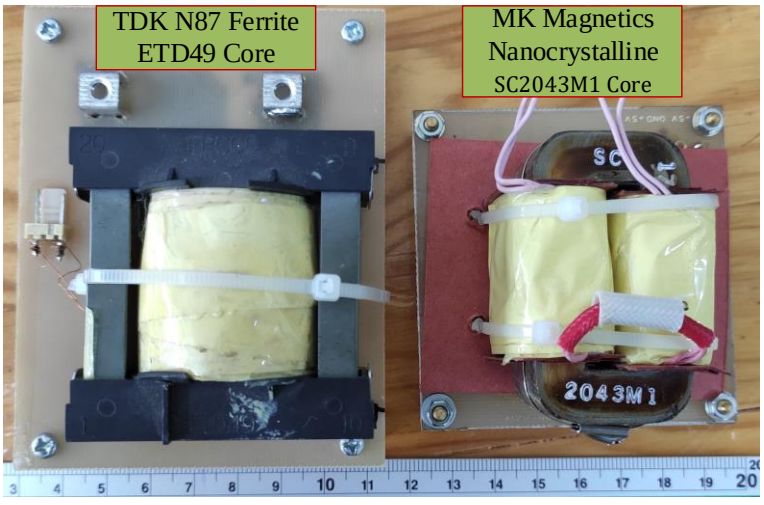

Figure 3-14 Auxiliary inductors

Table 3-4 Parameters of the auxiliary inductors

Inductor	A	B
Inductance	786 µH	765 µH
RMS current	3.6 A	3.6 A
Material	Ferrite N87	Nanocrystalline MK magnetics
Core structure	ETD49	SC2043M1
Total core area, A_c	2.11 cm^2	1.56 cm^2
Magnetic length, l_m	11.4 cm	12.8 cm
Winding	80 turns 2 in parallel of (40xAWG36)	85 turns 2 in parallel of (40xAWG36)
Air gap	2.2 mm	2.0 mm
Max. $\hat{B}$	0.24 T	0.30 T
Est. P_{cu}	1.6 W	1.6 W
Est. P_{fe}	1.4 W	1.6 W
Est. P_{tot}	3.0 W	3.2 W

Chapter 4

Experimental Results

4.1 No-load Tests of the Prototype Transformers

The prototype transformers described in chapter 3 were tested under no-load conditions to determine core losses P_{fe} under different magnetization waveforms. The primary winding of each transformer was excited by the low-voltage (LV) bridge as shown in Figure 4-1. The core loss was measured by using a 1-MHz Yokogawa WT3000E power meter, where the primary current is fed to an internal shunt resistor of the power meter and the secondary voltage is used as the measured voltage. The measured power is equal to

$$P_{meas} = \frac{1}{T_s}\int_0^{T_s} v_s(t) \cdot i_p(t)dt = \frac{1}{T_s}\int_0^{T_s} i_p(t) \cdot (N_2 \frac{dB(t)}{dt})dt. \qquad (4\text{-}1)$$

The core loss is then determined from

$$P_{fe} = \frac{N_1}{N_2} P_{meas} = \frac{1}{T_s}\int_0^{T_s} i_p(t) \cdot (N_1 \frac{dB(t)}{dt})dt. \qquad (4\text{-}2)$$

Moreover, the induced voltage $v_s(t)$ in the secondary winding was measured by a 20-MHz differential probe and the magnetizing current $i_{m1}(t)$ was measured by a 50-MHz HIOKI 3273-50 current probe. The experimental signals were recorded in a 70 MHz oscilloscope (ISO-TECH IDS1074B) with 1,000 data points per cycle. So, the instantaneous flux density $B(t)$ and magnetic field $H(t)$ can be calculated as follows.

$$B(t) = \frac{1}{N_2 A_c} \int v_s(t) dt \qquad (4\text{-}3)$$

$$H(t) = \frac{N_1 i_p(t)}{l_m} \qquad (4\text{-}4)$$

The extended phase shift modulation is used in this research where the duty ratio D of the low voltage primary winding is adjusted together with the phase shift δ between the primary and secondary voltage. According to Figure 2-7, the duty ratio of the primary winding voltage can be defined as

$$D = 1 - \frac{2\alpha}{\pi}. \qquad (4\text{-}4)$$

For this no-load test, the duty ratio was adjusted from 0.7 to 1.0 and the DC input voltage ranged from 42 to 54 V at the switching frequency of 20 kHz

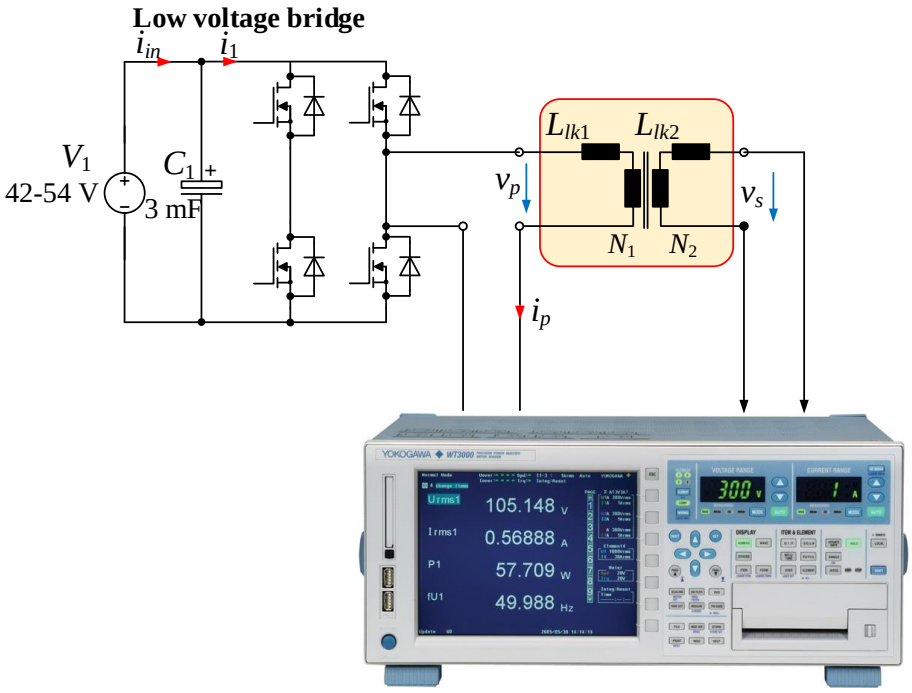

Figure 4-1 Experimental set up for no-load test

Figure 4-2 and Figure 4-3 show the induced voltage $v_s(t)$, flux density $B(t)$, magnetic field $H(t)$ and the B-H curve of the ferrite transformer A with the input voltage of 54 V at the duty ratios of $D = 1.0$ and $D = 0.8$ respectively. There are oscillations in the $v_s(t)$ and $H(t)$ due to the parasitic capacitance of the transformer and the parasitic inductance of the converter. It can be observed that there is an area inside the B-H curve. This area exhibits the core loss. Figure 4-4 to Figure 4-7 display the induced voltage $v_s(t)$, flux density $B(t)$, magnetic field $H(t)$ and the $B - H$ curve of the nanocrystalline transformers B and C under the same magnetizing conditions as the ferrite transformer A. Transformer B has a small magnetizing current due to it high permeability. However, there is a very large oscillation in $v_s(t)$ and $H(t)$ and this oscillation is asymmetry. The $B - H$ curve of transformer B is very narrow, so a low core loss is expected. The $B - H$ curve of transformer C is also very narrow, but it exhibits a very large magnetizing field. In fact, it is even larger than the ferrite transformer A. This effect was reported to be due to the impregnation and cutting process of the core [47].

Figure 4-8 compares $B - H$ curves of the ferrite transformer A and nanocrystalline transformers B and C. It clearly shows that the hysteresis loop of the ferrite material is significantly larger than the other two nanocrystalline materials, whereas the working flux density is the lowest. This is confirmed by the core loss measurement results with the input voltage at the duty ratio $D = 0.7, D = 0.8, D = 0.9$ and $D = 1.0$ in Figure 4-9. The toroidal nanocrystalline core from King magnetics exhibits the lowest loss because it passed through only the impregnation process without cutting, while the cut C-cores from the MK magnetics is expected to be deteriorated during the cutting process. Moreover, the nanocrystalline material from MK magnetics itself exhibits a higher loss than that from the King magnetics as illustrated in Figure 3-6 and Figure 3-7.

The core losses with the input voltage in Figure 4-9 correspond to the core losses with the peak flux density shown in Figure 4-10. Predicted core loss estimated from the Steinmetz equation in (3-3) are plotted along the measurements. The Steinmetz equation is basically an empirical model which is best fit for sinusoidal excitation. However, the flux density waveforms of this experiment are triangular for $D = 1.0$ and chopped triangular for $D < 1.0$. Thus, there are periodic components with frequency multiple number of 20 kHz, which contribute to the additional losses.

The difference between the experiment results and the predicted loss for the ferrite transformer A is believed to be due to 2 reasons. One is due to the non-sinusoidal flux density waveforms, and the other is due to the core temperature. Core loss of the MnZn N87 ferrite has a strong temperature dependence. Loss at 100°C is approximately 60% of that at 25°C. Parameters of the Steinmetz equation were extracted from the loss data at 100°C. However, the measured core loss was conducted at room temperature and the core temperature increased slightly.

The measured core loss of the transformer B is lower than the predicted values. This could be due to the core under test is an uncut core which was not significantly deteriorated during the manufacturing process. Another reason is the loss values are too low and may be affected by the accuracy of the power meter since the magnetizing current is approximately about 1 A.

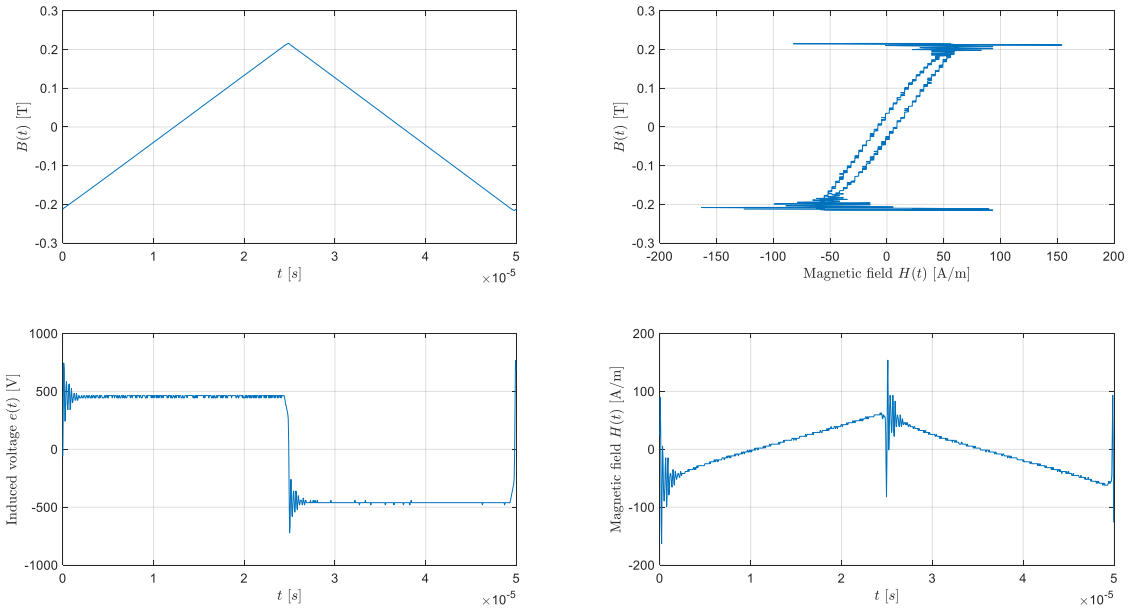

Figure 4-2 Induced voltage, flux density, magnetic field and the $B-H$ curve of the ferrite transformer A at 54 V, $D = 1.0$.

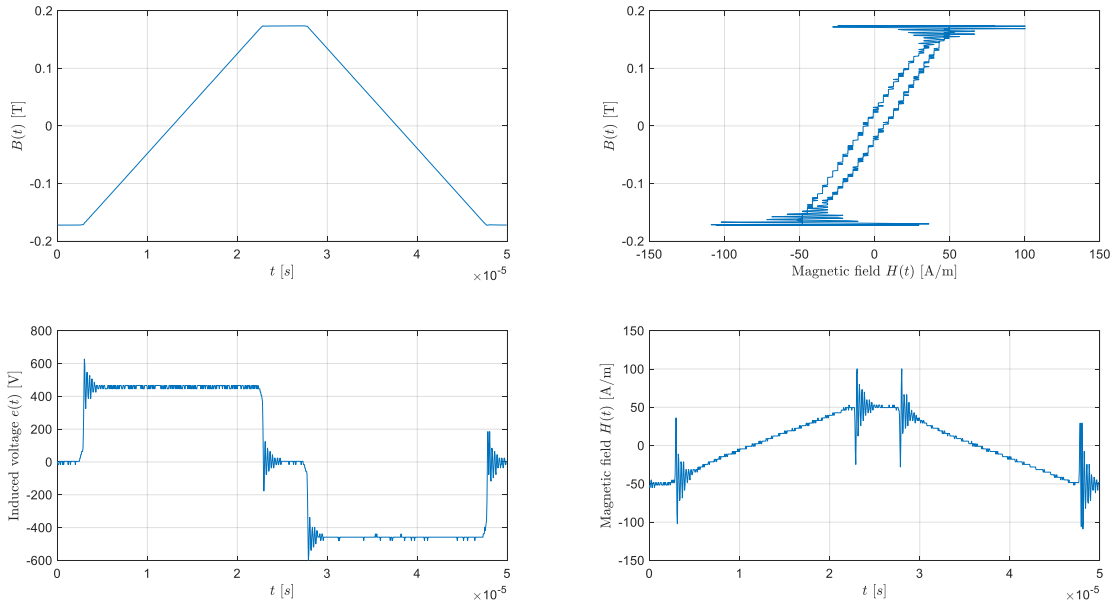

Figure 4-3 Induced voltage, flux density, magnetic field and the $B-H$ curve of the ferrite transformer A at 54 V, $D = 0.8$.

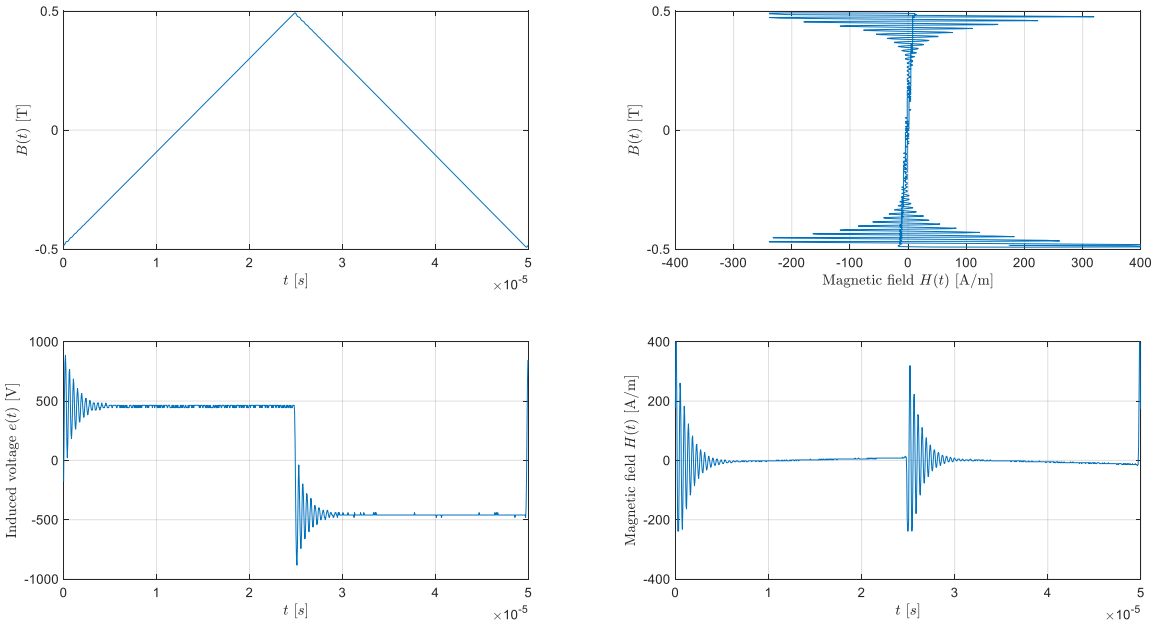

Figure 4-4 Induced voltage, flux density, magnetic field and the $B-H$ curve of the nanocrystalline transformer B at 54 V, $D = 1.0$.

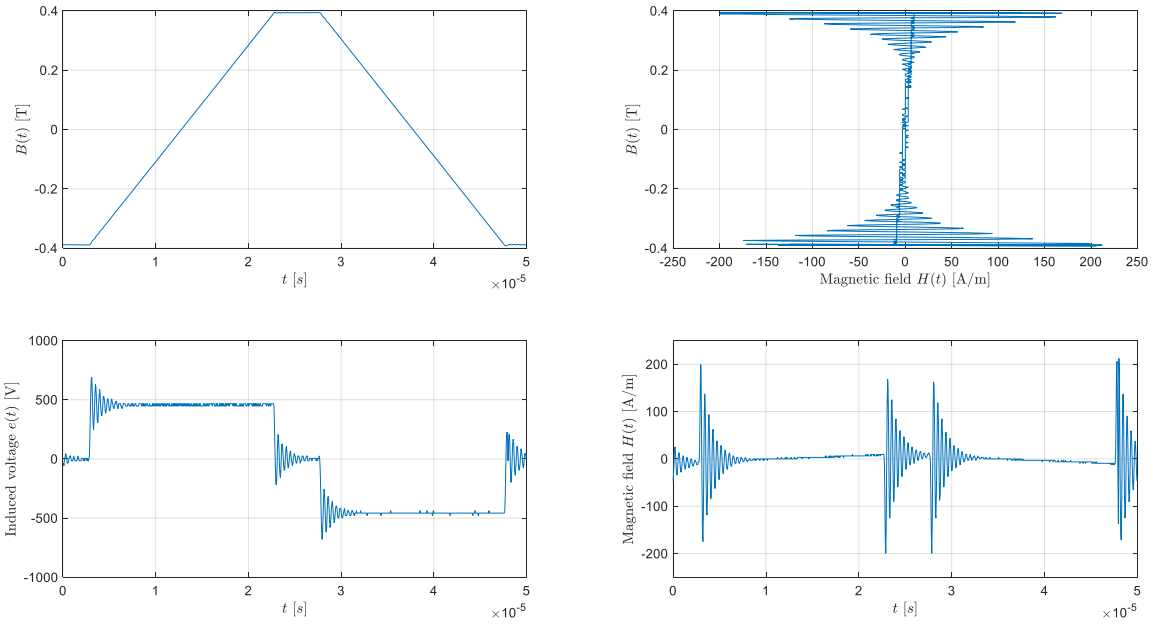

Figure 4-5 Induced voltage, flux density, magnetic field and the $B-H$ curve of the nanocrystalline transformer B at 54 V, $D = 0.8$.

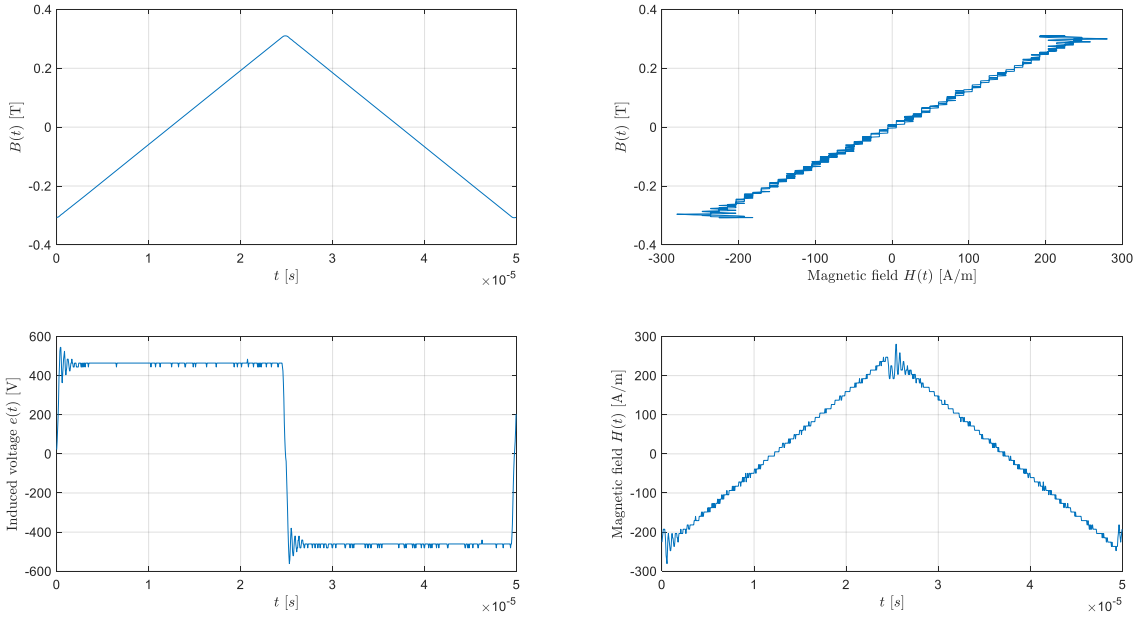

Figure 4-6 Induced voltage, flux density, magnetic field and the $B-H$ curve of the nanocrystalline transformer C at 54 V, $D=1.0$.

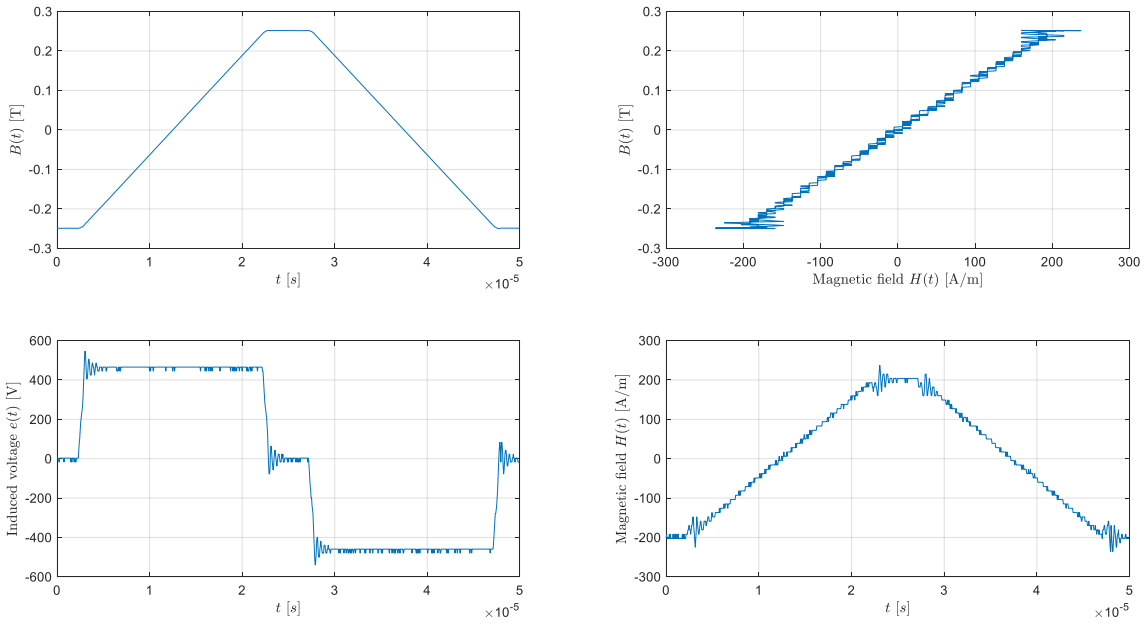

Figure 4-7 Induced voltage, flux density, magnetic field and the $B-H$ curve of the nanocrystalline transformer C at 54 V, $D=0.8$.

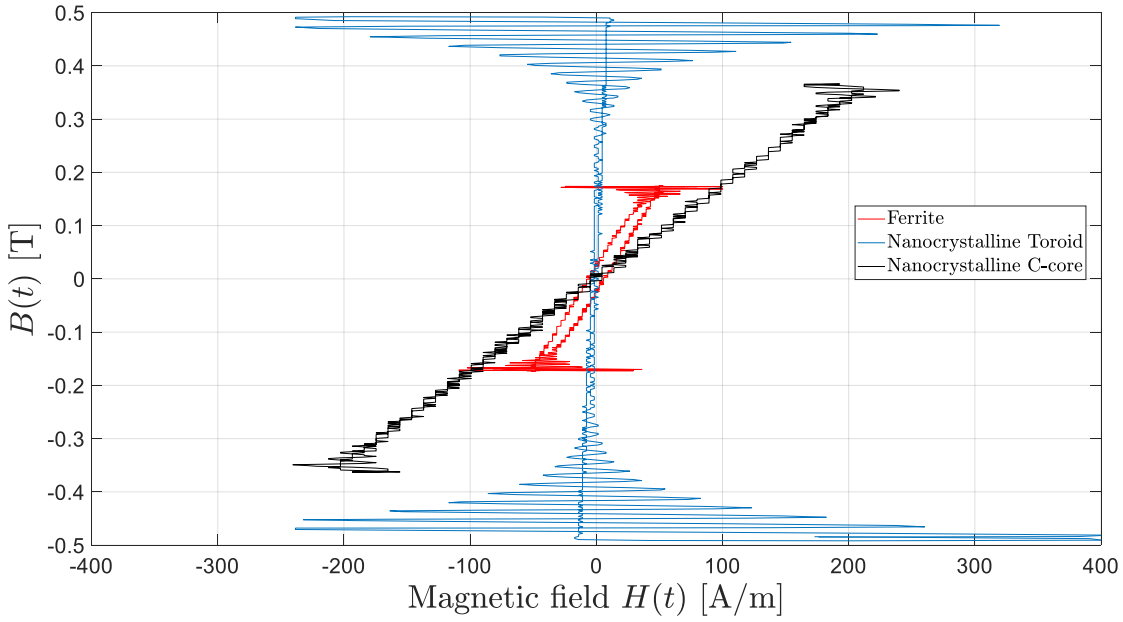

Figure 4-8 $B-H$ curves of the ferrite transformer A, and the nanocrystalline transformers B and C at 54 V, $D = 1.0$

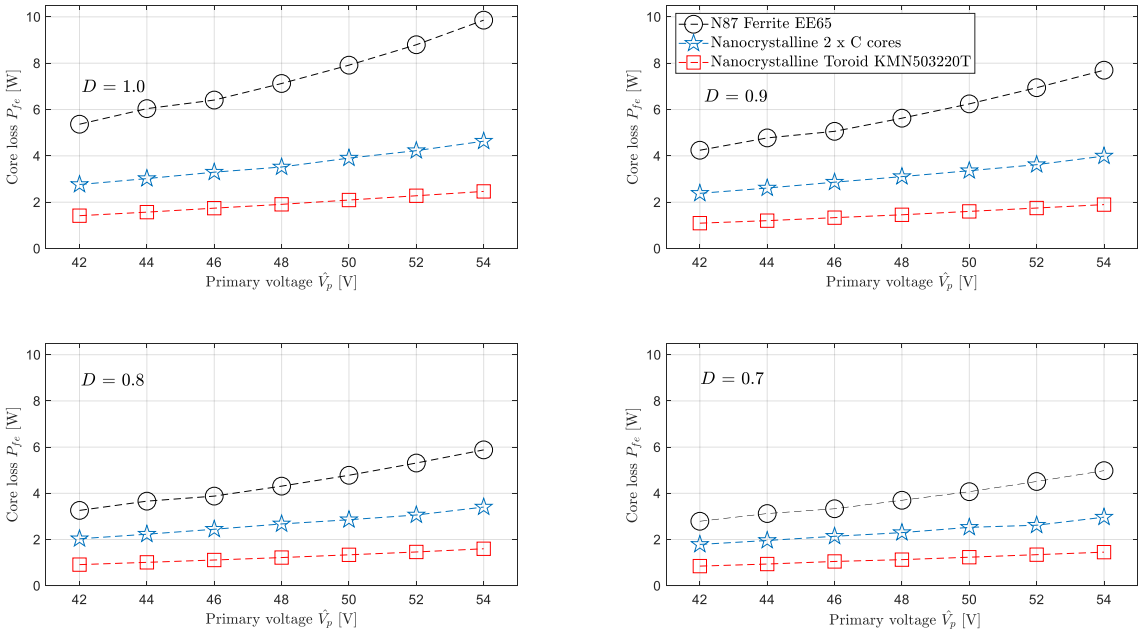

Figure 4-9 Core losses of transformers A,B and C with 42-54V and $0.7 \leq D \leq 1.0$.

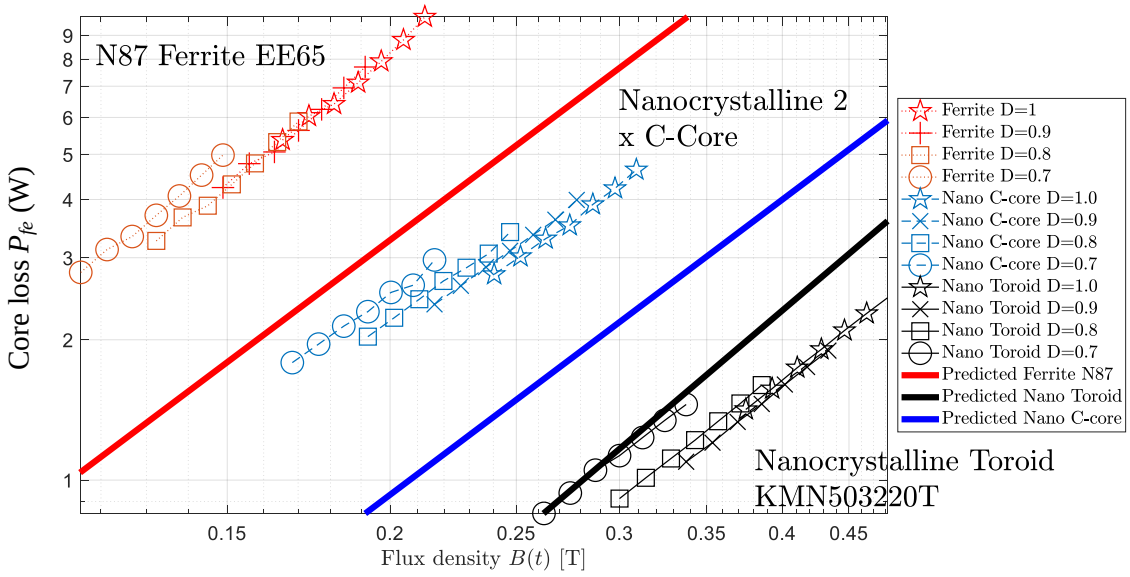

Figure 4-10 Core losses of transformers A,B and C with peak flux density and $0.7 \leq D \leq 1.0$.

4.2 On-load Tests of the Prototype Transformers

4.2.1 Experimental setup

The three prototype transformers and the auxiliary inductors were tested with the DAB DC-DC converter shown in Figure 4-11. The primary current is connected to the channel 1 internal shunt resistor of the power meter, and the secondary current is connected to the internal shunt resistors of channel 2 and channel 3. The primary voltage is connected to the voltage input of channel 1, where the associated quantities of the primary side are measured. The channel 3 is used for measurement of the secondary side of the transformer and the channel 3 measures the quantities across the auxiliary inductor.

During the experiments, the ferrite transformer A was used together with the ferrite inductor A listed in Table 2-1, whereas the nanocrystalline transformers B

and C were connected with the nanocrystalline inductor B. A 150-A 10-MHz Hioki 3274 was used to measure the primary current and the secondary current was measured by a 30-A 50-MHz Hioki 3273-50. The primary voltage, secondary voltage and inductor voltage were measured by 20-MHz differential probes. The experimental waveforms were recorded in a 70-MHz ISO-TECH IDS1074B oscilloscope.

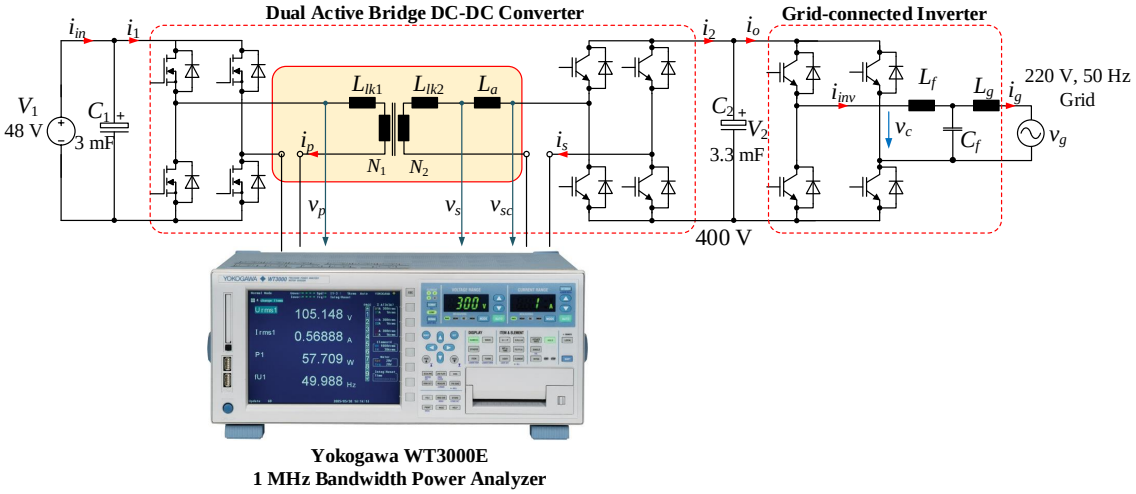

Figure 4-11 Experimental set up for on-load test

4.2.2 Operating waveforms

Figure 4-12 show the primary voltage $v_p(t)$, the primary current $i_P(t)$, the secondary voltage $v_s(t)$ and the inductor voltage $v_{La}(t)$ of the ferrite transformer A and the ferrite inductor A at the nominal voltage $V_1 = 48$ V, $\delta = 60°$, the duty ratio $D = 1.0$. The output power of the transformer is 1,054 W which is slightly less than the design. This is due to the presence of the leakage inductance of the transformer. The operating waveforms are close to the analytical waveforms in Figure 2-3. The duty ratio is applied on the primary voltage depicted in Figure 4-13 which are very close to the analytical waveforms in Figure 2-7. The inductor voltage and the primary

current change when the voltage ratio d increases as shown in Figure 4-14 with the output power of 1,200 W. In fact, the duty ratio is normally applied at a high input voltage in order to decrease the RMS current and power factor of the transformer as shown in Figure 4-14. Figure 4-16 shows the operating waveforms at the lowest input voltage which is similar to the analytical waveforms in Figure 2-5.

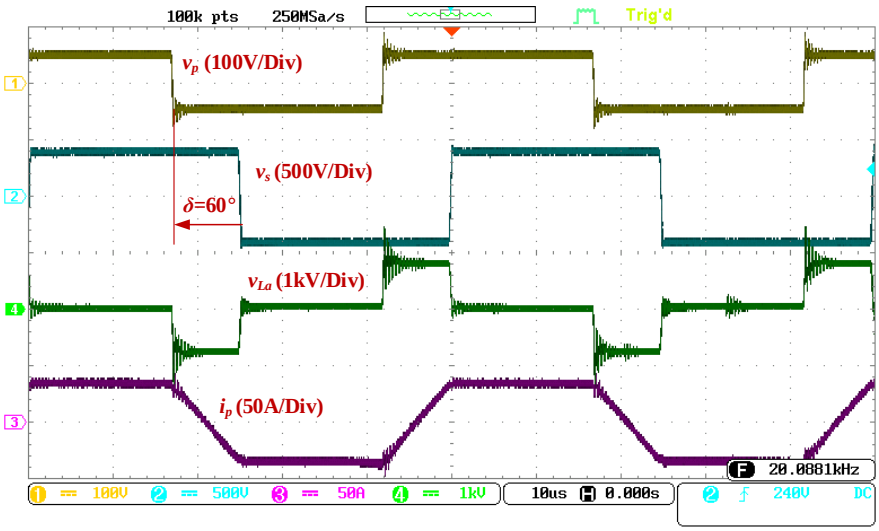

Figure 4-12 Operating waveforms of the DAB DC-DC converter with the ferrite transformer A and the ferrite inductor A at $V_1 = 48$ V, $\delta = 60$°C and $D = 1.0$.

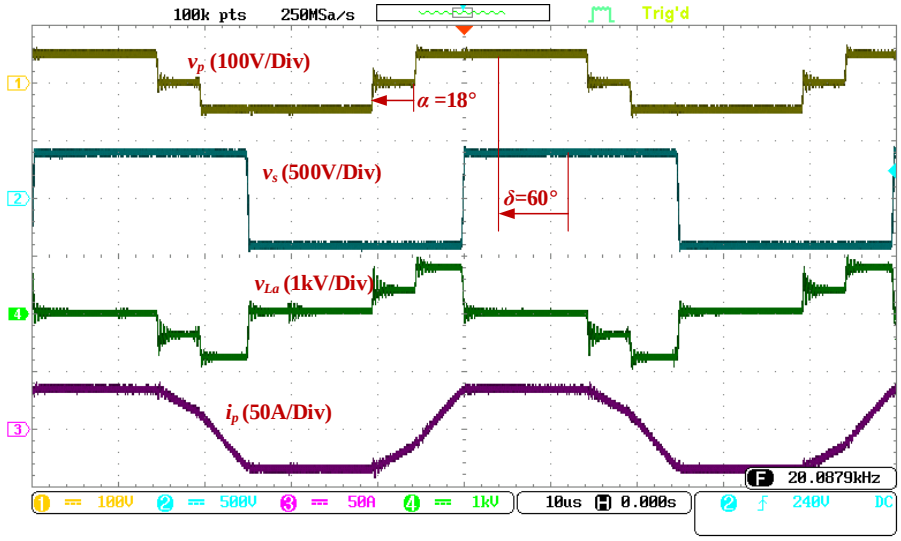

Figure 4-13 Operating waveforms of the DAB DC-DC converter with the ferrite transformer A and the ferrite inductor A at $V_1 = 48$ V, $\delta = 60°$C and $D = 0.8$.

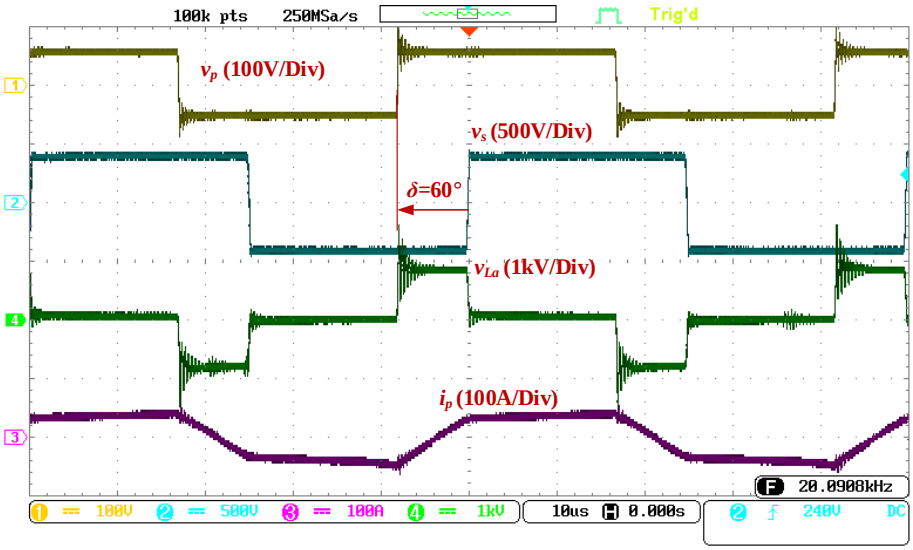

Figure 4-14 Operating waveforms of the DAB DC-DC converter with the ferrite transformer A and the ferrite inductor A at $V_1 = 54$ V, $\delta = 60°$C and $D = 1.0$.

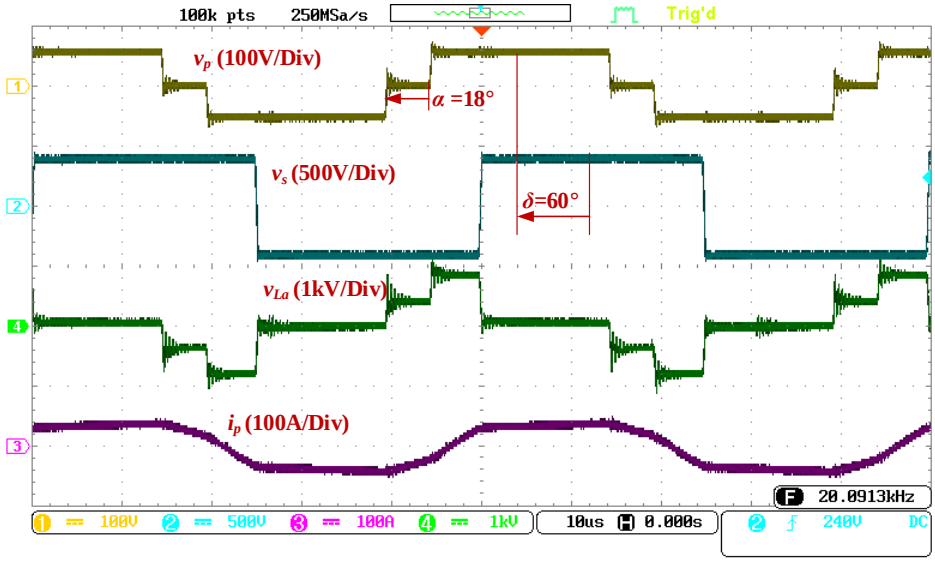

Figure 4-15 Operating waveforms of the DAB DC-DC converter with the ferrite transformer A and the ferrite inductor A at $V_1 = 54$ V, $\delta = 60°$C and $D = 0.8$.

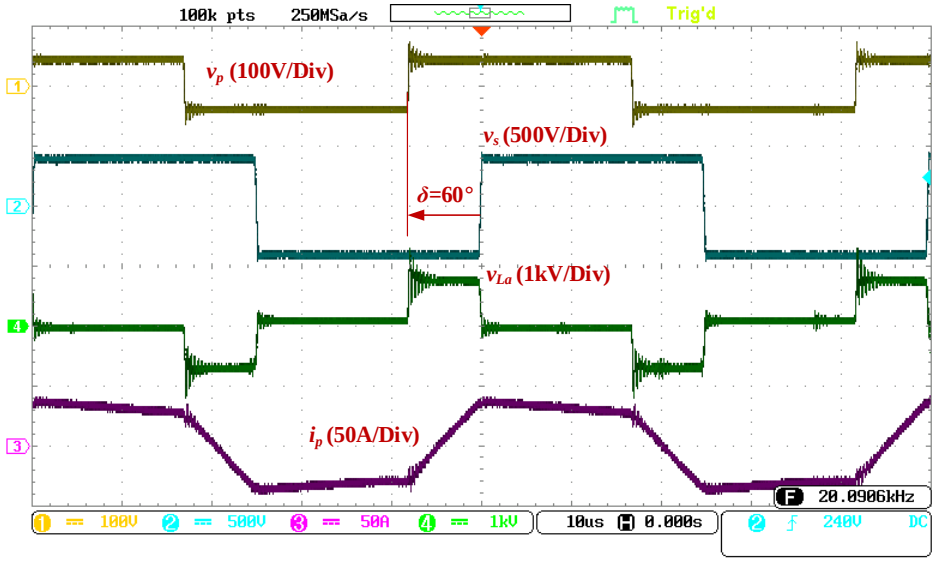

Figure 4-16 Operating waveforms of the DAB DC-DC converter with the ferrite transformer A and the ferrite inductor A at $V_1 = 42$ V, $\delta = 60°$C and $D = 1.0$.

Figure 4-17 to Figure 4-21 shows the operating waveforms of the nanocrystalline transformer B with the nanocrystalline inductor B under the same operating conditions as the ferrite transformer A. In general, the operating waveforms of the transformer B are close to those of the ferrite transformer B. However, there is an asymmetry in the inductor voltage which causes a spike in the primary current as encircled in Figure 4-21. This is believed to be due to the asymmetry in the magnetizing current shown in Figure 4-4. The cause and mitigation of this effect are outside the scope of this project and it will be investigated in the future.

Figure 4-22 to Figure 4-26 are the operating waveforms of the nanocrystalline transformer C with the nanocrystalline inductor B under the same operating conditions as the ferrite transformer A and the nanocrystalline transformer B. The operating waveforms of transformer C are very close to those of the ferrite transformer A and there is no spike in the primary current as those of the nanocrystalline transformer B.

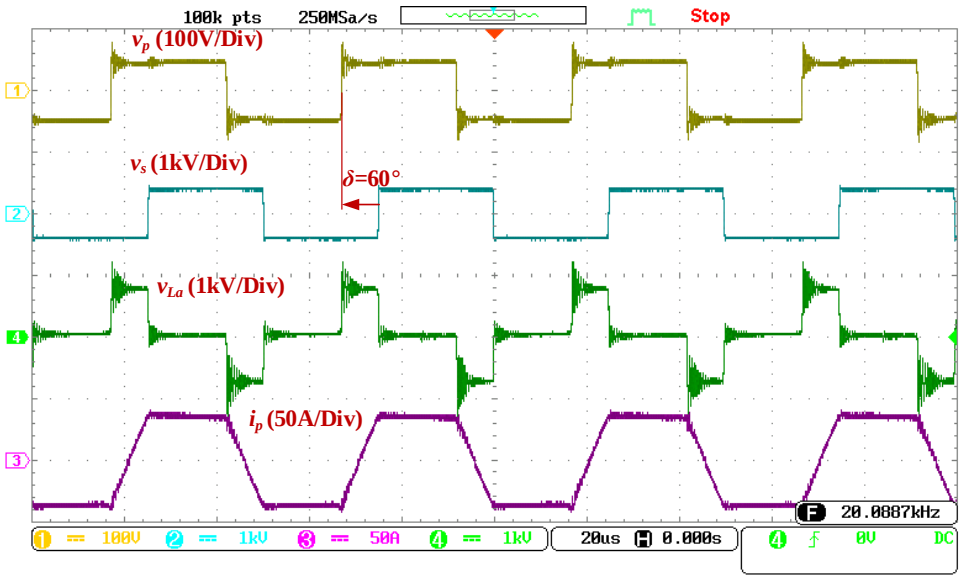

Figure 4-17 Operating waveforms of the DAB DC-DC converter with the nanocrystalline transformer B and the nanocrystalline inductor B at $V_1 = 48$ V, $\delta = 60$°C and $D = 1.0$.

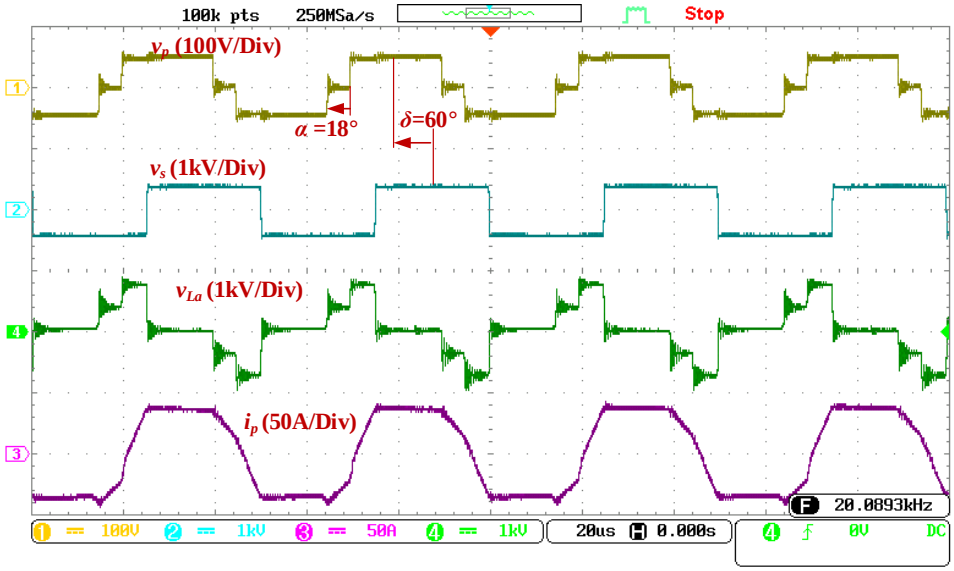

Figure 4-18 Operating waveforms of the DAB DC-DC converter with the nanocrystalline transformer B and the nanocrystalline inductor B at $V_1 = 48$ V, $\delta = 60$°C and $D = 0.8$.

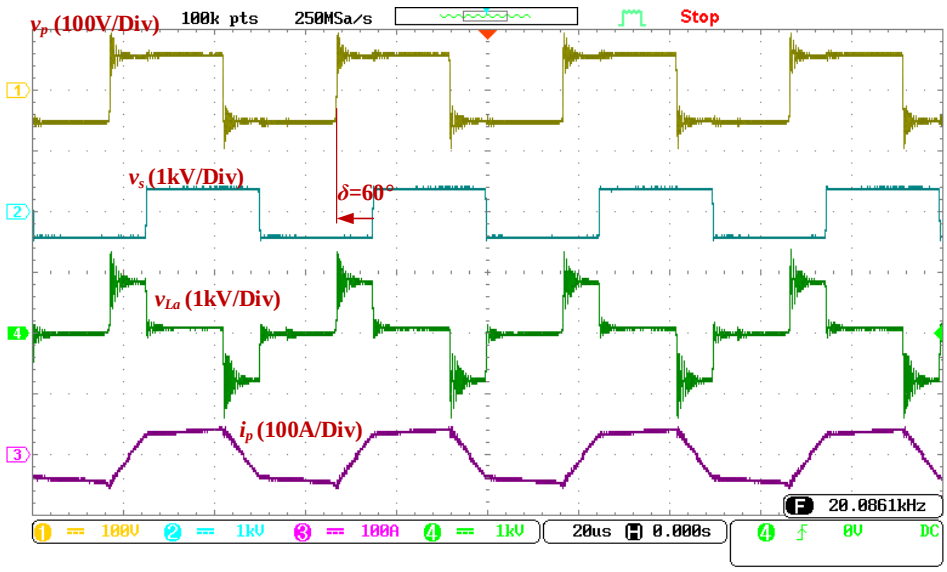

Figure 4-19 Operating waveforms of the DAB DC-DC converter with the nanocrystalline transformer B and the nanocrystalline inductor B at $V_1 = 54$ V, $\delta = 60°$C and $D = 1.0$.

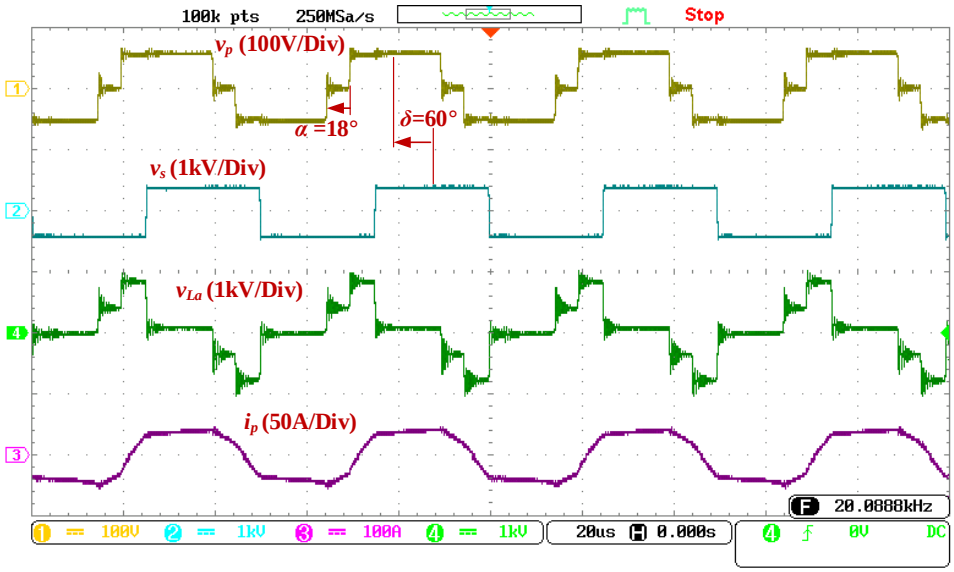

Figure 4-20 Operating waveforms of the DAB DC-DC converter with the nanocrystalline transformer B and the nanocrystalline inductor B at $V_1 = 54$ V, $\delta = 60°$C and $D = 0.8$.

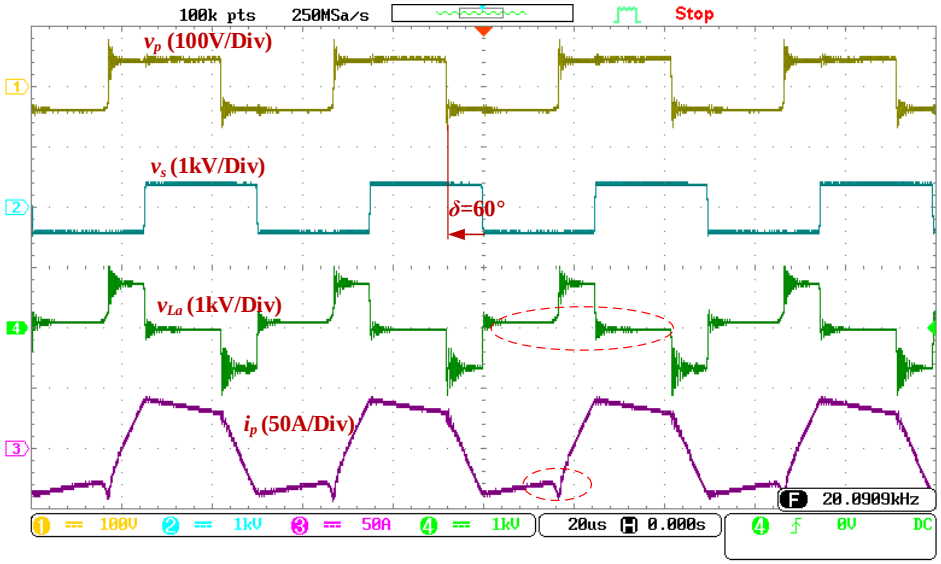

Figure 4-21 Operating waveforms of the DAB DC-DC converter with the nanocrystalline transformer B and the nanocrystalline inductor B at $V_1 = 42$ V, $\delta = 60°$C and $D = 1.0$.

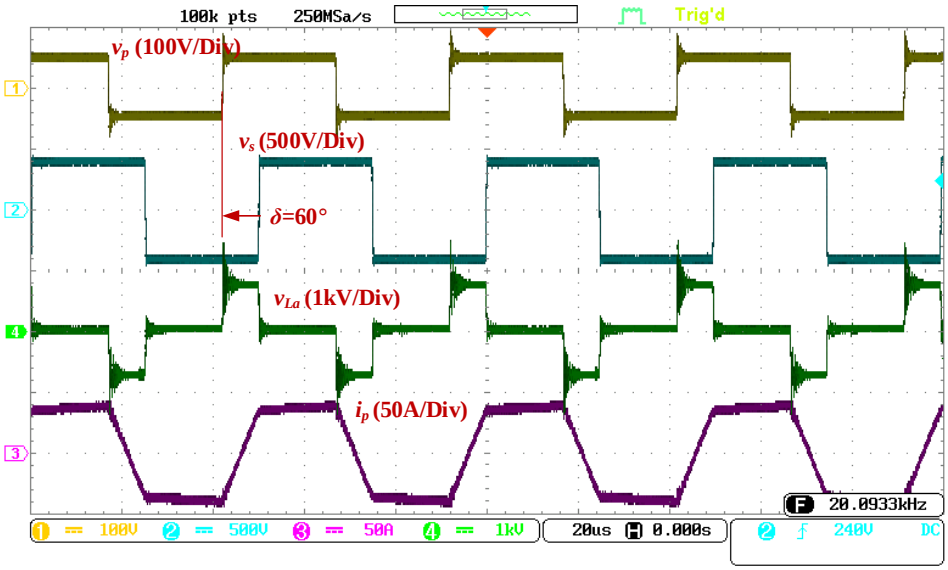

Figure 4-22 Operating waveforms of the DAB DC-DC converter with the nanocrystalline transformer C and the nanocrystalline inductor B at $V_1 = 48$ V, $\delta = 60°$C and $D = 1.0$.

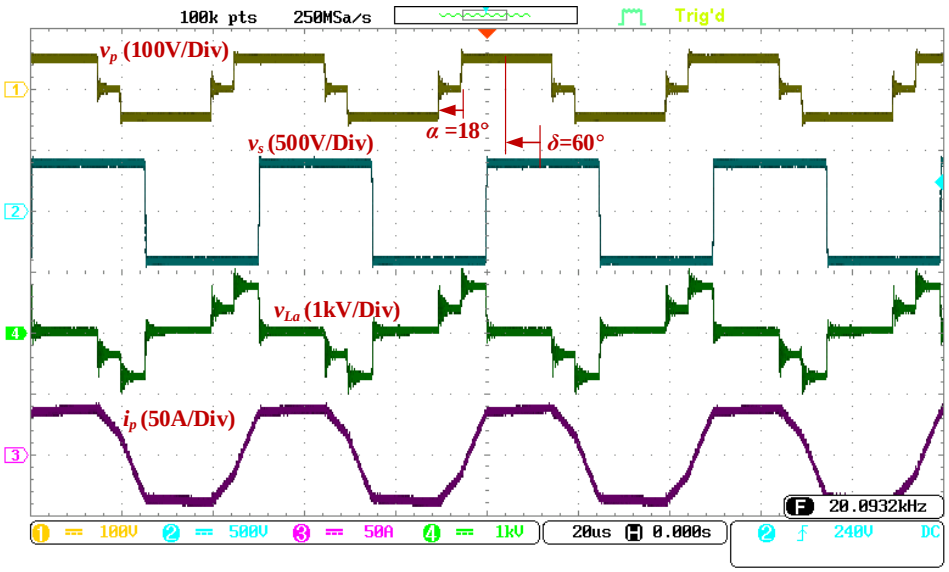

Figure 4-23 Operating waveforms of the DAB DC-DC converter with the nanocrystalline transformer C and the nanocrystalline inductor B at $V_1 = 48$ V, $\delta = 60$°C and $D = 0.8$.

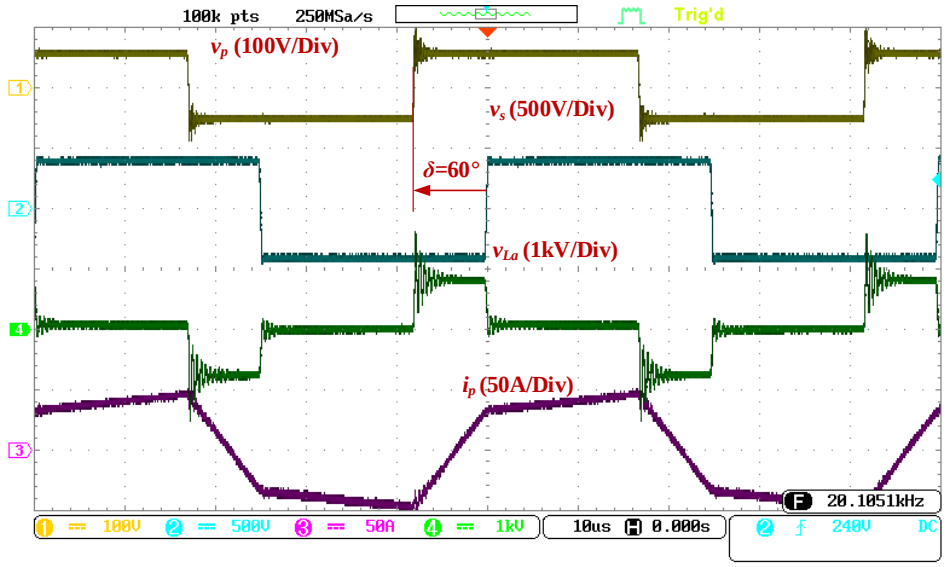

Figure 4-24 Operating waveforms of the DAB DC-DC converter with the nanocrystalline transformer C and the nanocrystalline inductor B at $V_1 = 54$ V, $\delta = 60$°C and $D = 1.0$.

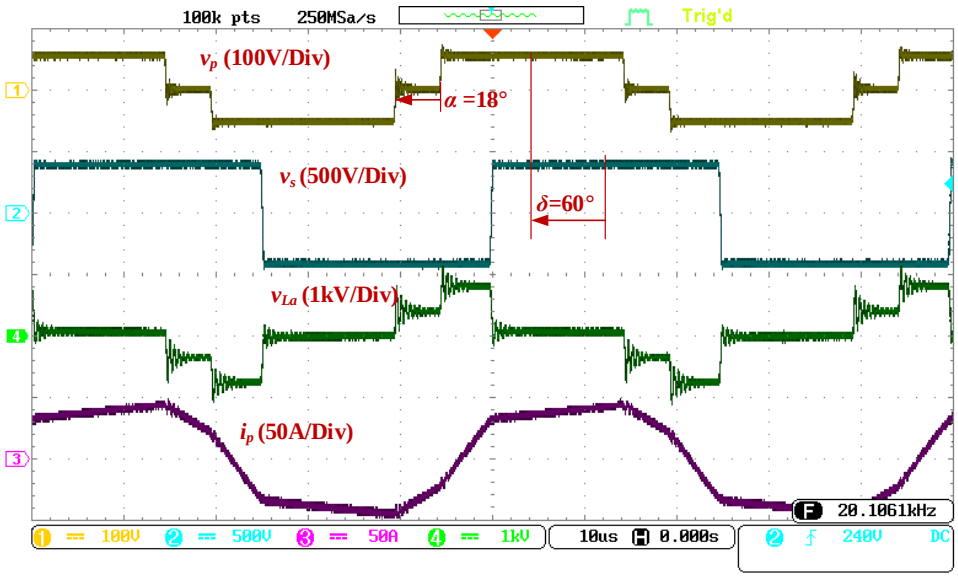

Figure 4-25 Operating waveforms of the DAB DC-DC converter with the nanocrystalline transformer C and the nanocrystalline inductor B at $V_1 = 54$ V, $\delta = 60°$C and $D = 0.8$.

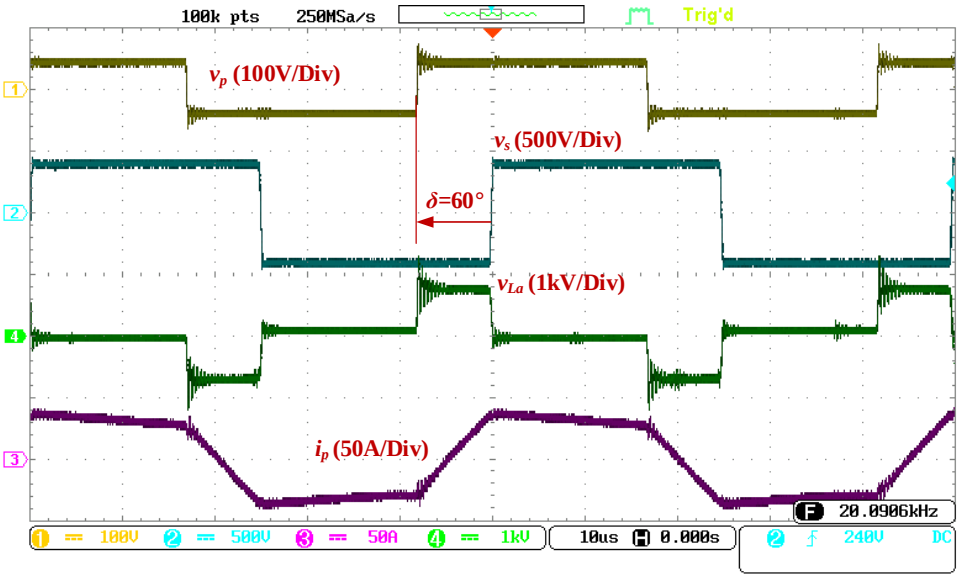

Figure 4-26 Operating waveforms of the DAB DC-DC converter with the nanocrystalline transformer C and the nanocrystalline inductor B at $V_1 = 42$ V, $\delta = 60°$C and $D = 1.0$.

4.2.3 Operating performance of the prototype transformers

This section describes the performance of the prototype transformers obtained from the power meter. Although the inductor loss was also measured, there was discrepancy in the measurements. This is due to the fact the inductor voltage has a narrow pulse shape and the loss is too low for the power meter to indicate reliable measurement results. Thus, the inductor measurement results are excluded in this chapter.

Figure 4-27 depicts the transferred power at the secondary winding P_s, the RMS primary current I_s, the total loss in the transformer P_{loss} and the ratio of the core loss to the total loss P_{fe}/P_{loss} of the ferrite transformer A with the phase shift angle δ at the input voltage of 42 V, 48 V and 54 V. Figure 4-28 compares the efficiency of the ferrite transformer A under the same conditions. It is noted that the core loss of the ferrite transformer A during the on-load operation is assumed to be 70% of the measured core loss given in the previous section. This is derived from the temperature dependent core loss curve of the N87 material [37]. The on-load working temperature is shown in the next section. The measured power loss at 48 V and $\delta = 60°$ is found to be 24.2 W where the estimated total loss during the design stage in Table 2-1 is only 10.0 W. Copper loss contributes approximately 75-80% at the maximum phase shift. The difference mainly comes from the non-sinusoidal flux density. Moreover, the main contribution of the copper loss is due to eddy current loss due to the skin effect and the proximity effect which is neglected during the design stage. At δ=60°, the even distribution between the core and the copper losses results in the maximum efficiency which found to be about 98.4%. The efficiency at the maximum power is found to be 97.6%.

Adoption of the extended phase shift modulation improves the flux density waveform and current waveforms closer to be sinusoidal. This reduces the RMS current and increases the efficiency as shown in Figure 4-27 to Figure 4-30. The maximum efficiency is found to be 98.8% at 48 V, $\delta = 30°$ and $D = 0.7$. The efficiency increases about 1% when reducing the duty ratio to $D = 0.7$.

The nanocrystalline transformers B and C with the nanocrystalline inductor B has a similar trend with the ferrite transformer as depicted in Figure 4-33 to Figure 4-44. The nanocrystalline transformer B has the maximum efficiency of 99.2% at 48 V, $\delta = 30°$ and $D = 0.7$. However, the efficiency drops significantly to 97.6% at 54 V, $\delta = 60°$ and $D = 1.0$. Moreover, the P_{fe}/P_{loss} ratio is smaller than the ferrite transformer A. This is because of the primary winding covers around the core as shown in Figure 3-11 making the winding length longer than the windings of transformers A and C.

The nanocrystalline transformer C has relatively flat efficiency curves. Th e maximum efficiency is 99.1% at 48 V, $\delta = 30°$ and $D = 0.7$ and the lowest efficiency is found to be 98.4% 99.2% at 54 V, $\delta = 30°$ and $D = 1.0$. It can be observed that the nanocrystalline transformer C has the highest RMS current among the three transformers especially at 54 V, $\delta = 60°$ and $D = 1.0$. This is because of a high magnetizing current shown in Figure 4-8 which partly contributes to the copper loss in the primary winding.

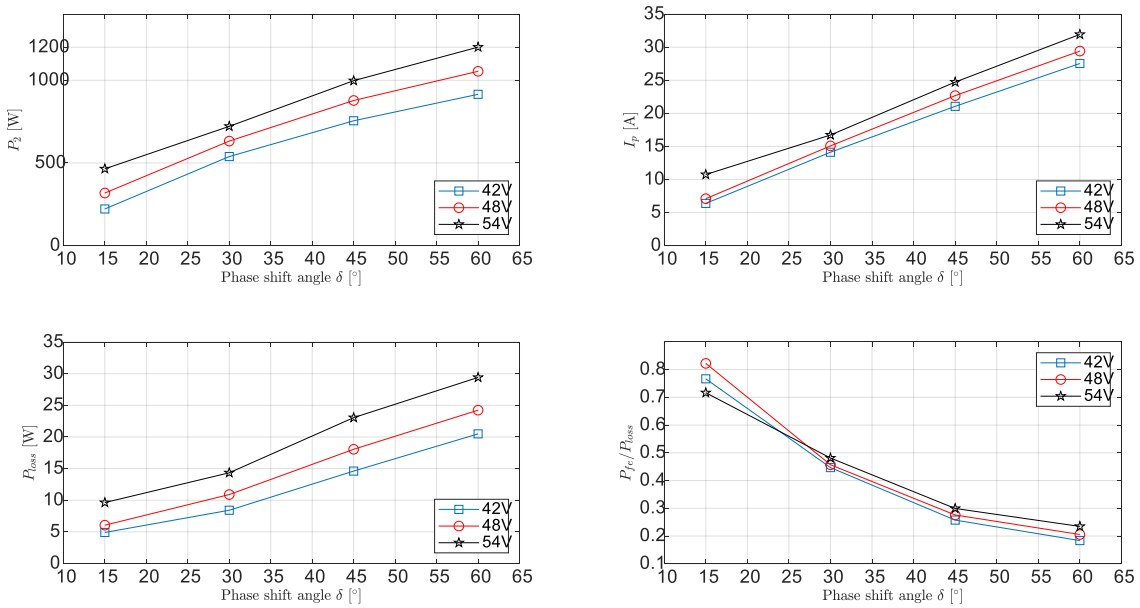

Figure 4-27 Output power, primary current, power loss and core loss to power loss ratio of the ferrite transformer A at 42 V, 48 V and 54 V with $D = 1.0$.

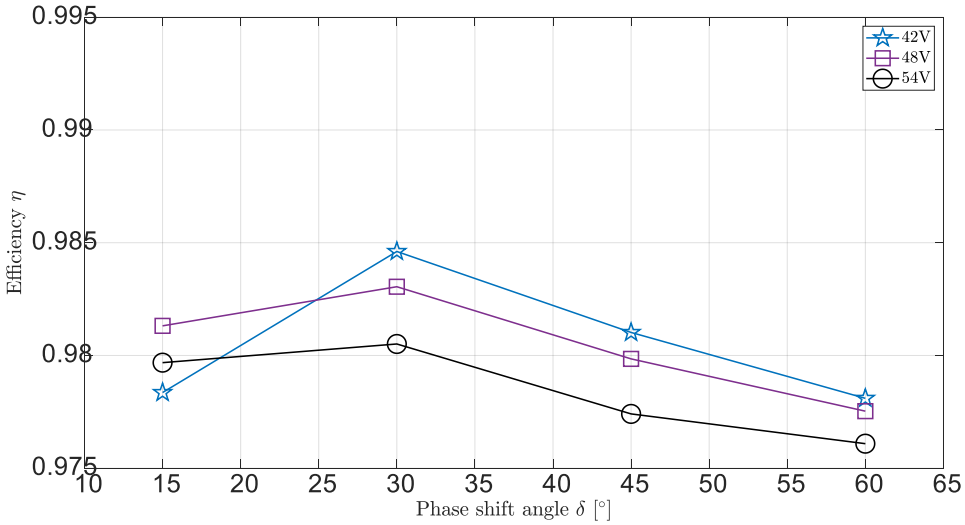

Figure 4-28 Efficiency of the ferrite transformer A at 42 V, 48 V and 54 V with $D = 1.0$.

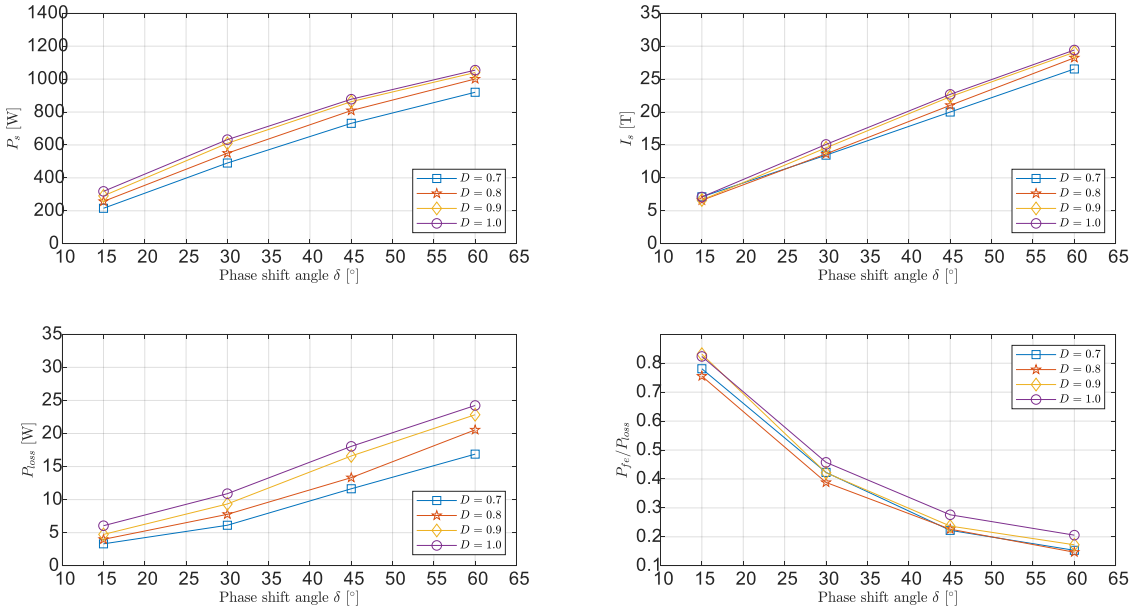

Figure 4-29 Output power, primary current, power loss and core loss to power loss ratio of the ferrite transformer A at 48 V with $0.7 \leq D \leq 1.0$.

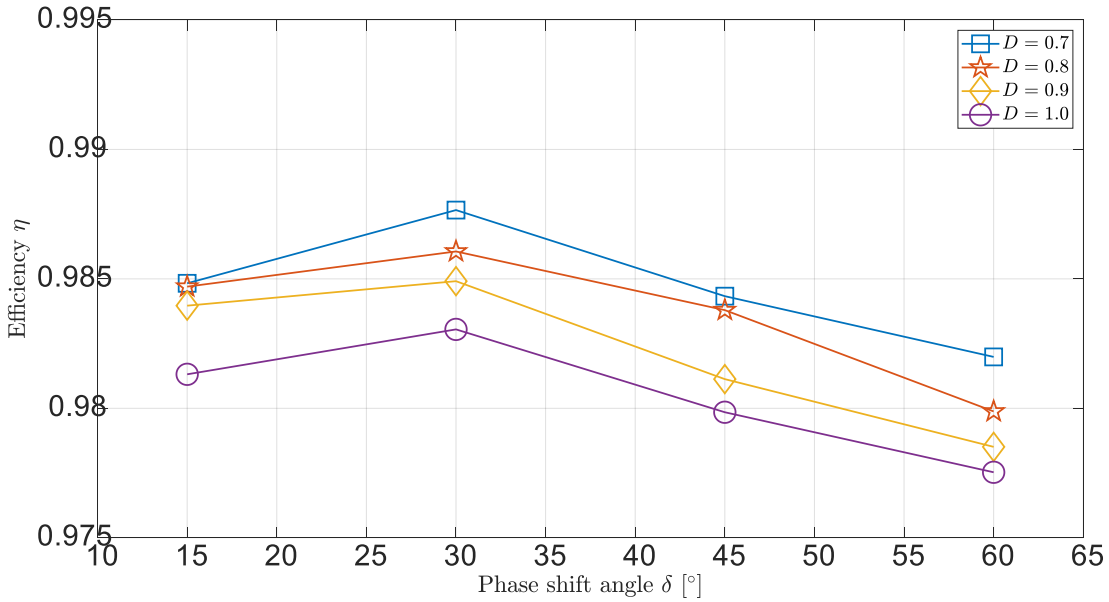

Figure 4-30 Efficiency of the ferrite transformer A at 48 V with $0.7 \leq D \leq 1.0$

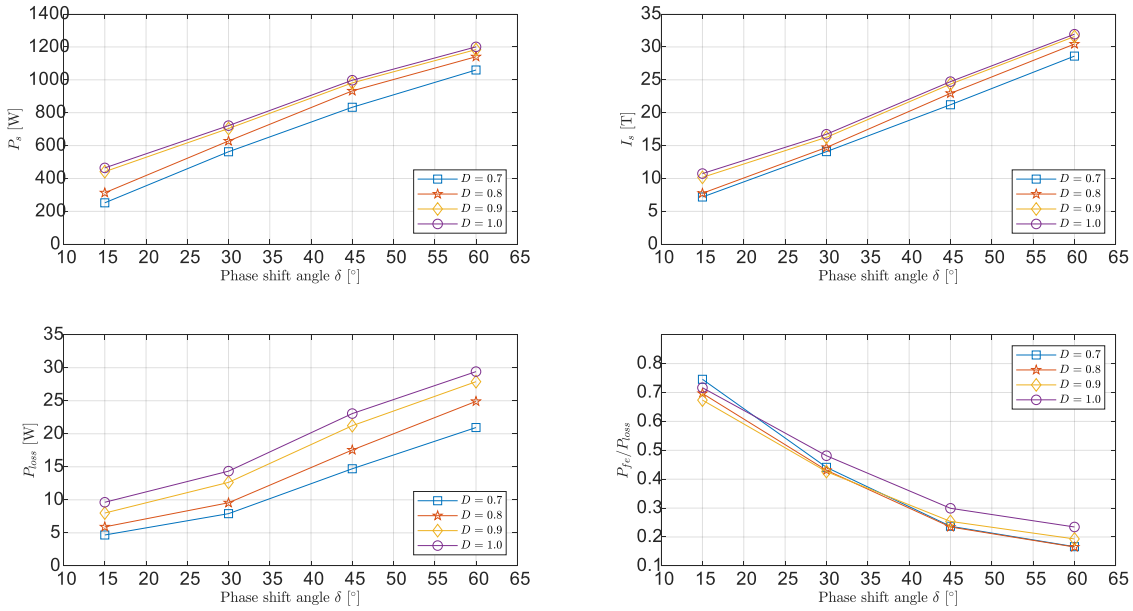

Figure 4-31 Output power, primary current, power loss and core loss to power loss ratio of the ferrite transformer A at 54 V with $0.7 \leq D \leq 1.0$.

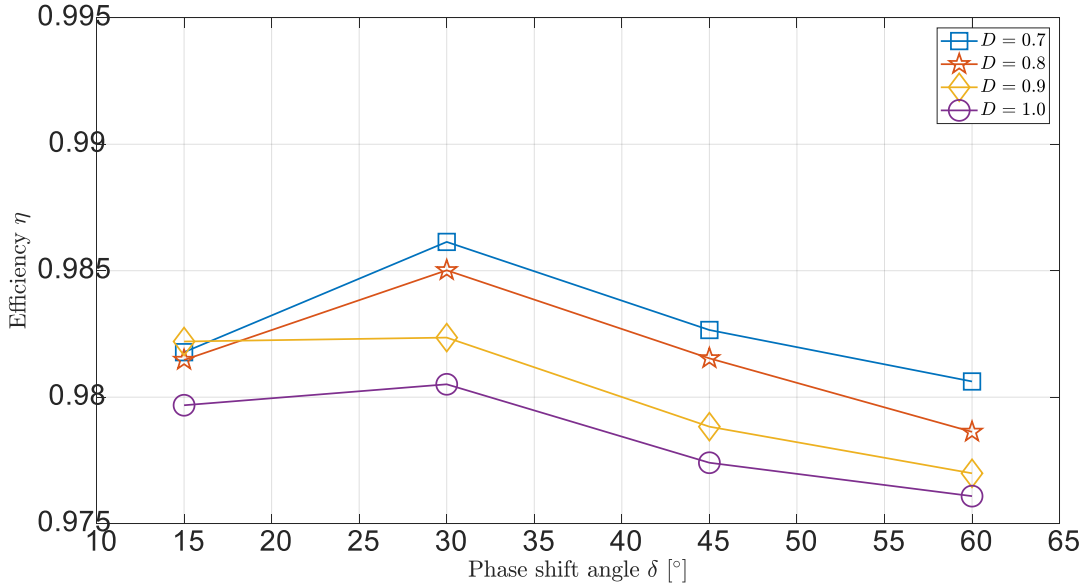

Figure 4-32 Efficiency of the ferrite transformer A at 54 V with $0.7 \leq D \leq 1.0$

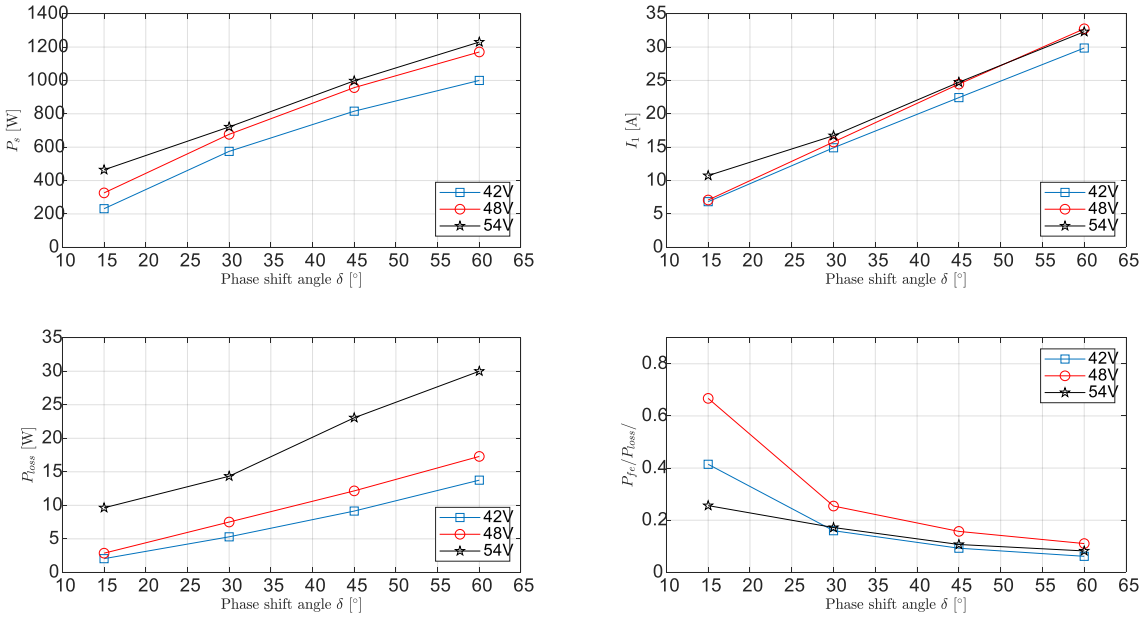

Figure 4-33 Output power, primary current, power loss and core loss to power loss ratio of the nanocrystalline transformer B at 42 V, 48 V and 54 V with $D = 1.0$.

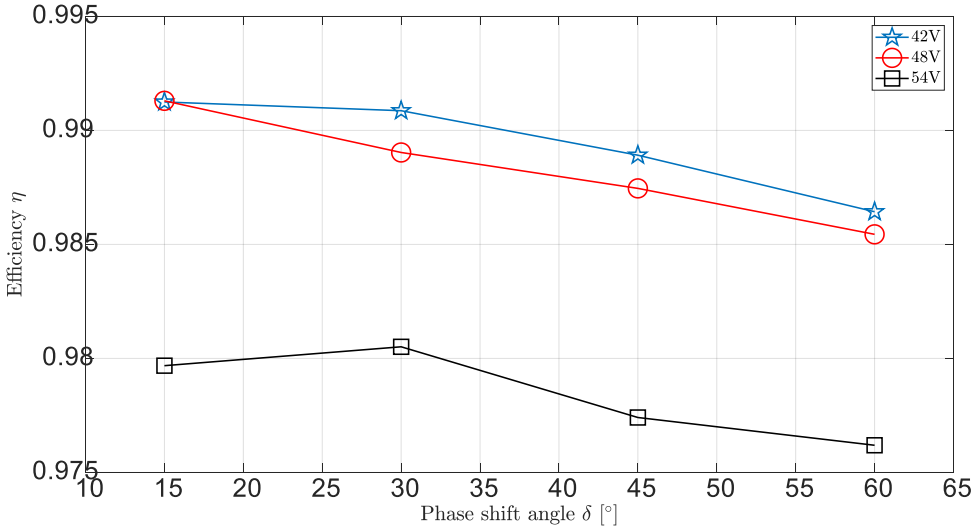

Figure 4-34 Efficiency of the nanocrystalline transformer B at 42 V, 48 V and 54 V with $D = 1.0$.

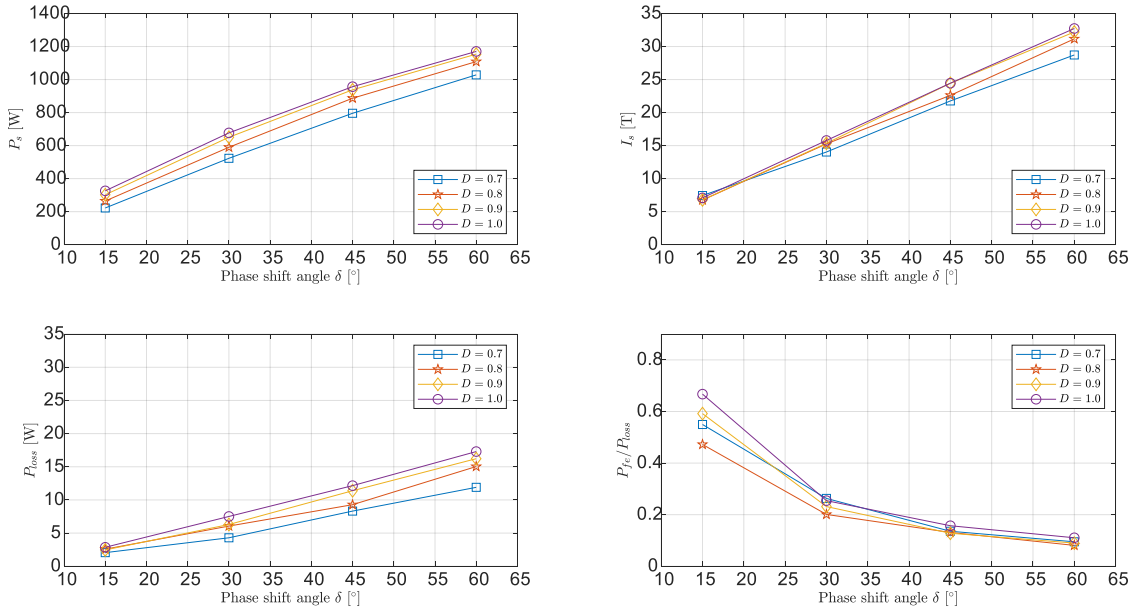

Figure 4-35 Output power, primary current, power loss and core loss to power loss ratio of the nanocrystalline transformer B at 48 V with $0.7 \leq D \leq 1.0$.

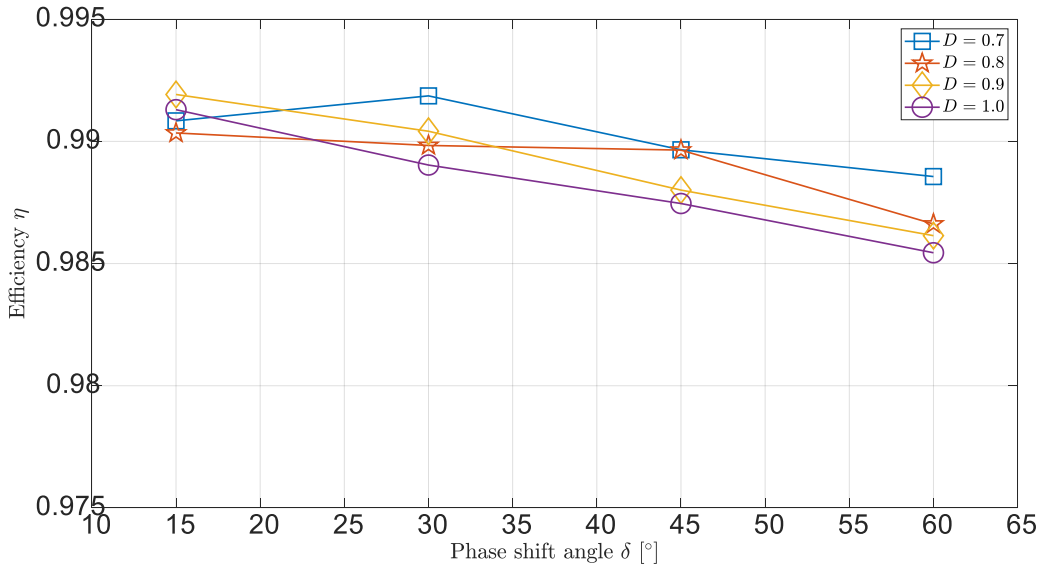

Figure 4-36 Efficiency of the nanocrystalline transformer B at 48 V with $0.7 \leq D \leq 1.0$

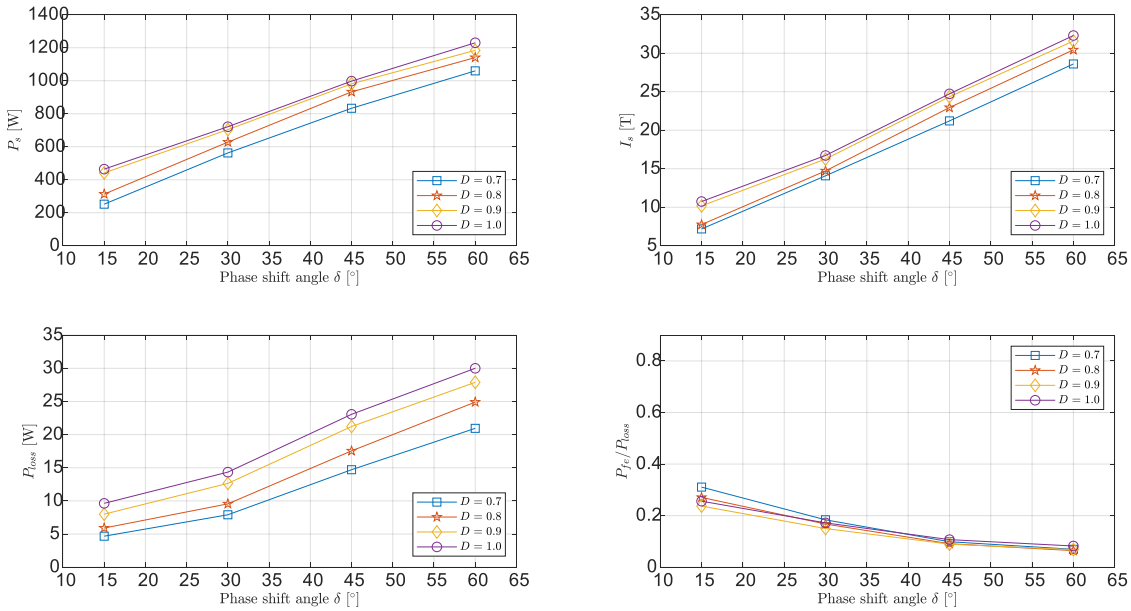

Figure 4-37 Output power, primary current, power loss and core loss to power loss ratio of the nanocrystalline transformer B at 54 V with $0.7 \leq D \leq 1.0$.

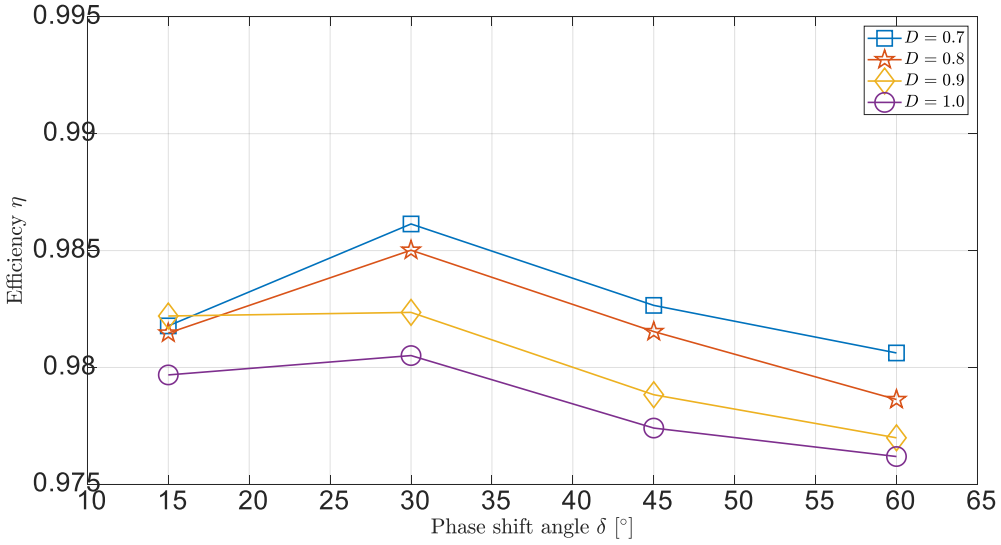

Figure 4-38 Efficiency of the nanocrystalline transformer B at 54 V with $0.7 \leq D \leq 1.0$

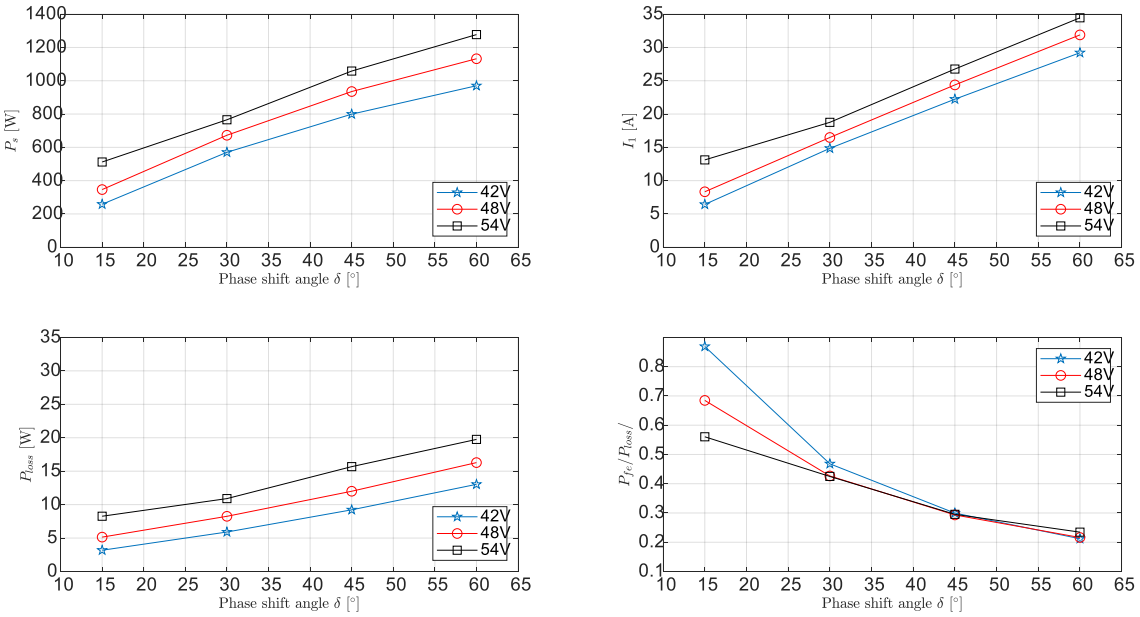

Figure 4-39 Output power, primary current, power loss and core loss to power loss ratio of the nanocrystalline transformer C at 42 V, 48 V and 54 V with $D = 1.0$.

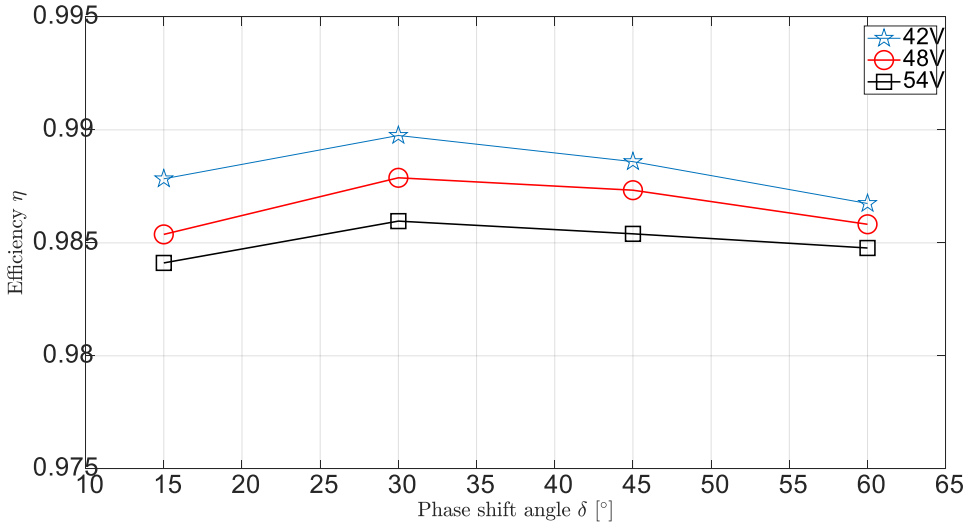

Figure 4-40 Efficiency of the nanocrystalline transformer C at 42 V, 48 V and 54 V with $D = 1.0$.

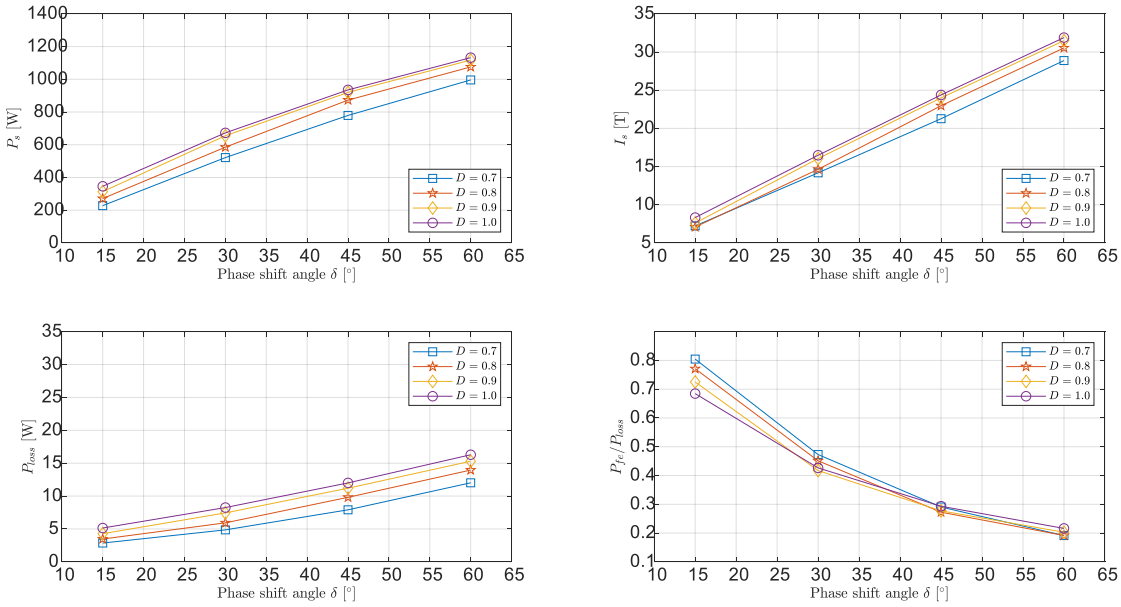

Figure 4-41 Output power, primary current, power loss and core loss to power loss ratio of the nanocrystalline transformer C at 48 V with $0.7 \leq D \leq 1.0$.

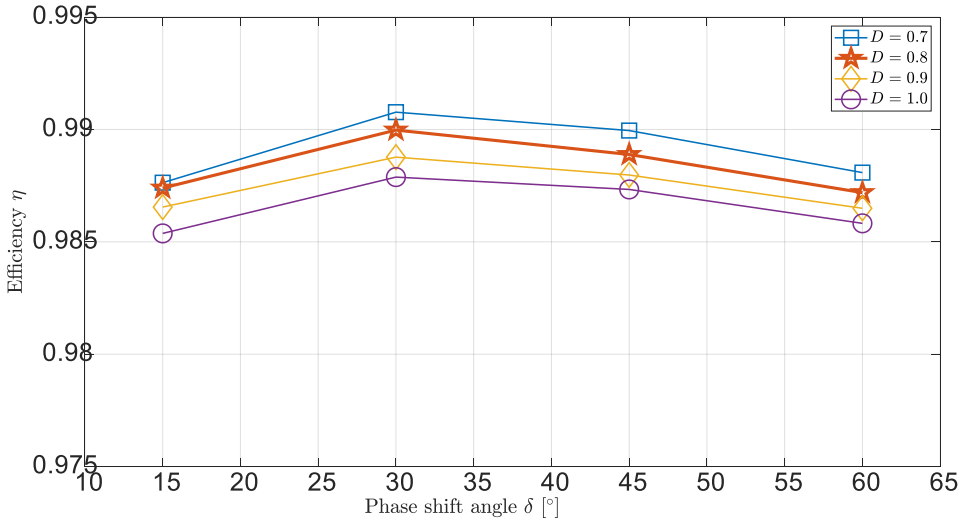

Figure 4-42 Efficiency of the nanocrystalline transformer C at 48 V with $0.7 \leq D \leq 1.0$

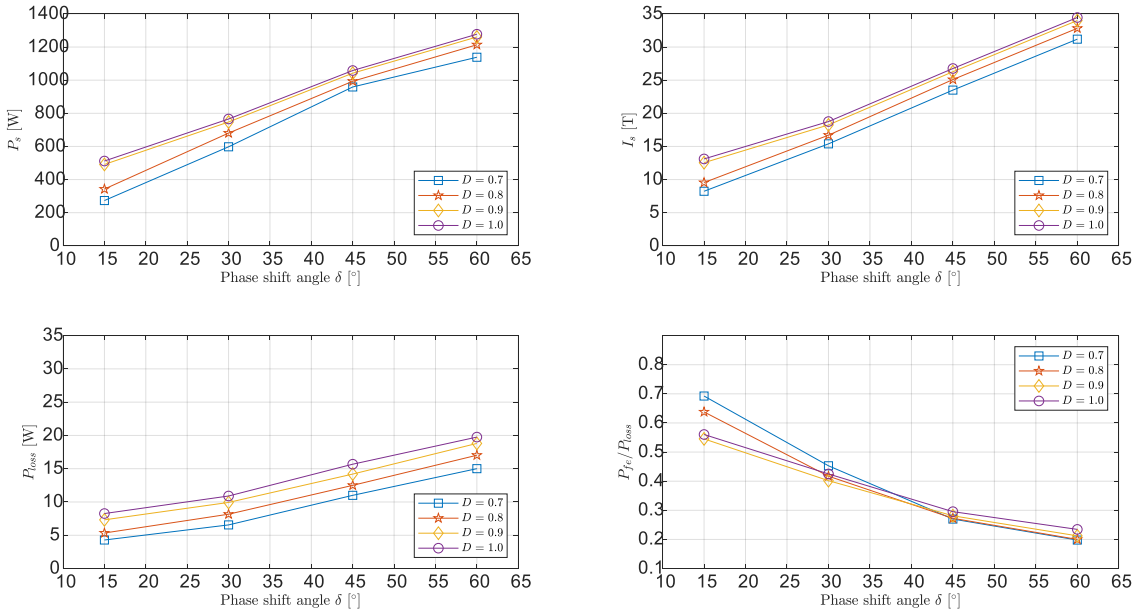

Figure 4-43 Output power, primary current, power loss and core loss to power loss ratio of the nanocrystalline transformer C at 54 V with $0.7 \leq D \leq 1.0$.

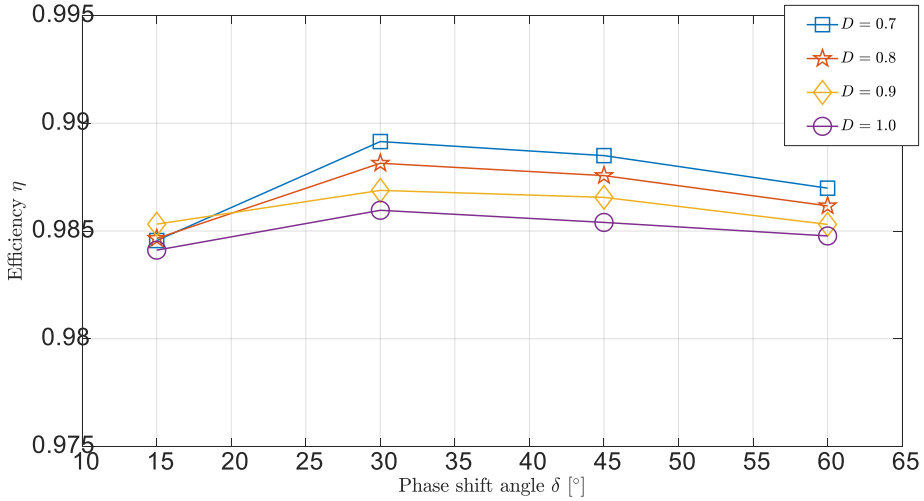

Figure 4-44 Efficiency of the nanocrystalline transformer C at 54 V with $0.7 \leq D \leq 1.0$

4.2.4 Temperature rise

The operating temperature of the prototype transformers and inductors were measured by using an infrared thermal imaging camera. Each transformer and inductor were operated at the nominal power for an hour. After that thermal images were taken. Figure 4-45 to Figure 4-47 shows the thermal images of the transformers A-C which illustrates that the hottest part occurs at the winding. This corresponds to the main loss contribution from the copper loss as given in the previous section. The ferrite transformer A is the hottest with the maximum temperature of 78.5°C and the nanocrystalline transformer B with the maximum temperature of 60°C is the coolest which also agree with the loss measurement.

Figure 4-48 and Figure 4-49 show the thermal images of the ferrite inductor A and the nanocrystalline inductor B. The 67.6°C hottest spot of the ferrite inductor A is also found at the winding. However, the core of the nanocrystalline inductor B is found to be the hottest with the maximum temperature of 78.8°C. A large core is not expected since the inductor is designed at the maximum flux density of 0.3 T. This could be an abnormality from the manufacturing process, which will be investigated in the future.

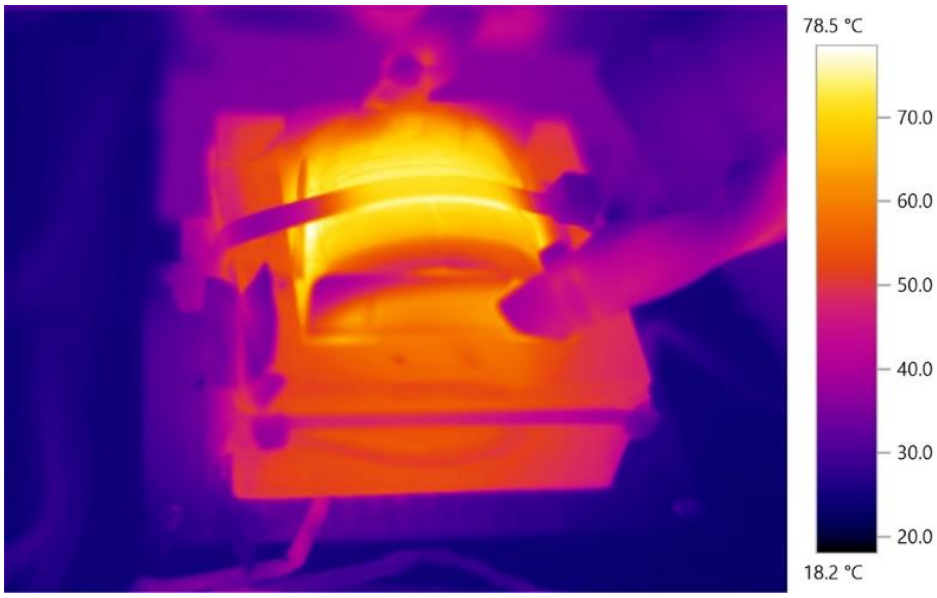

Figure 4-45 Thermal image of the ferrite transformer A after operating at the nominal power 60 minutes.

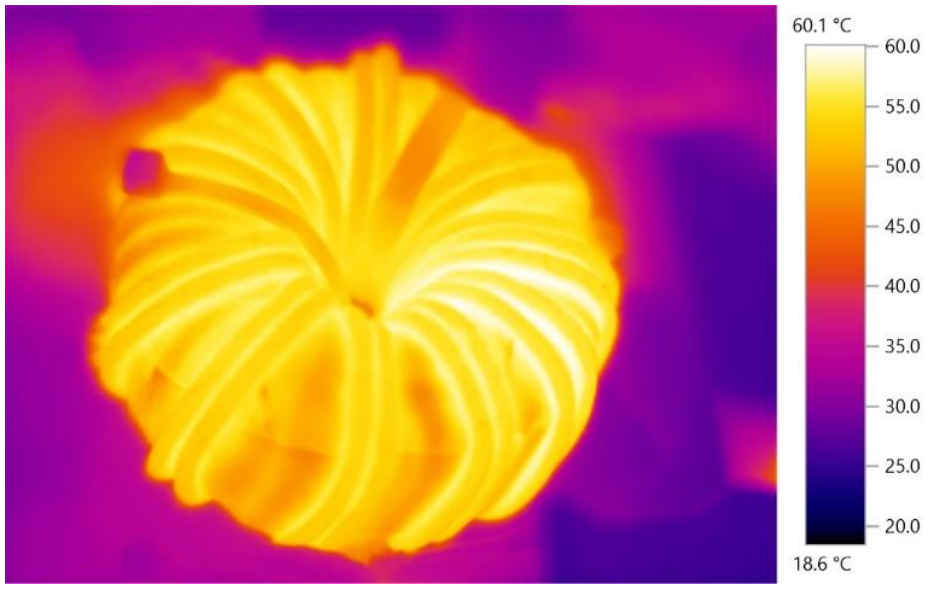

Figure 4-46 Thermal image of the nanocrystalline transformer C after operating at the nominal power 60 minutes.

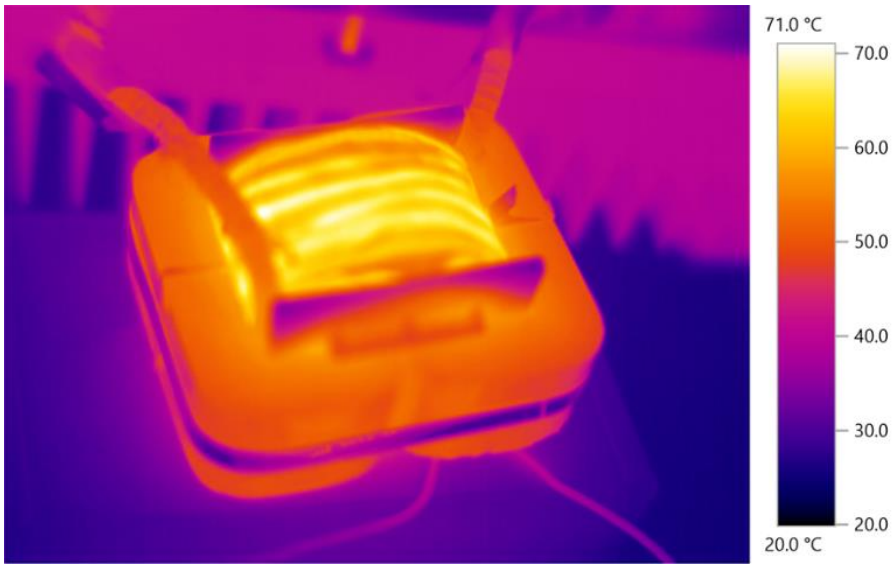

Figure 4-47 Thermal image of the nanocrystalline transformer C after operating at the nominal power 60 minutes.

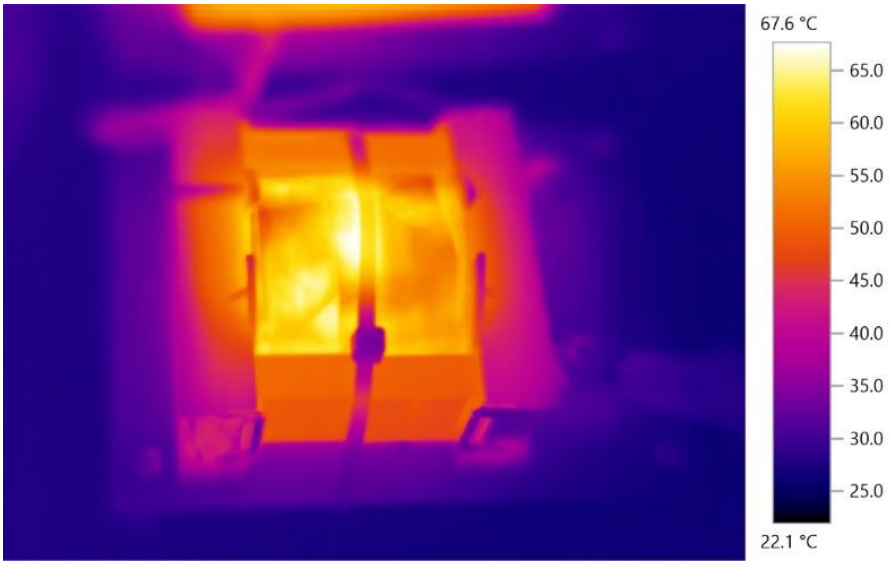

Figure 4-48 Thermal image of the ferrite inductor A after operating at the nominal power 60 minutes.

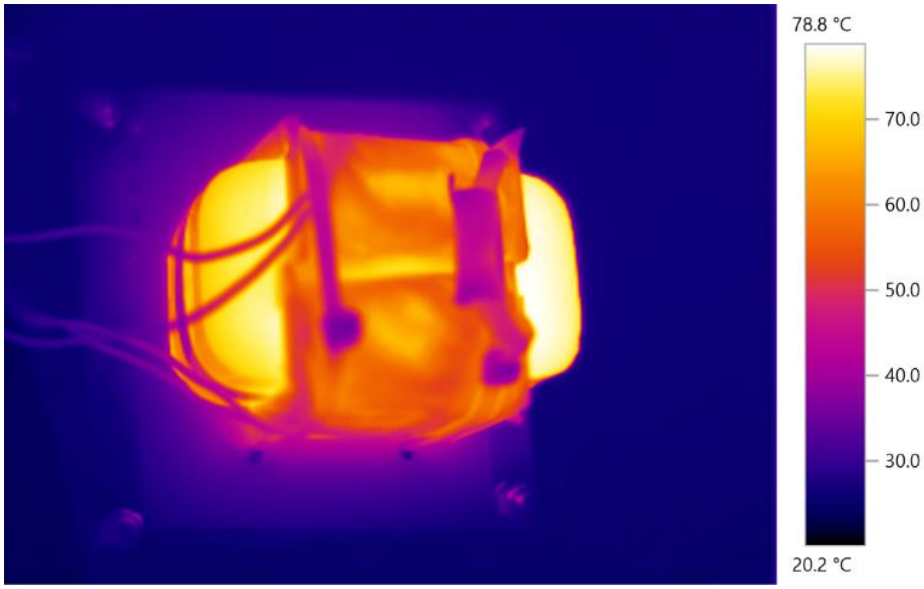

Figure 4-49 Thermal image of the nanocrystalline inductor B after operating at the nominal power 60 minutes.

4.3 Discussion

Table 4-1 summarizes the test results of the prototype transformers. The copper loss dominates the total loss. The maximum efficiency occurs when the core loss is close to the copper. The maximum efficiency points for all the three transformers are around the phase shift angle at 30°, which is not well optimized. This can be improved by reducing the turn number which causes two benefits. The first benefit is that larger and shorter wires are allowed so that the copper loss decreases and handles a greater current. The second advantage is the flux density will be raised which fully utilizes the core. The turn numbers of the ferrite transformer A and the nanocrystalline transformer B can be slightly reduced as the flux density at the maximum voltage is close to 50% of the maximum flux density of each material.

However, the nanocrystalline transformer C has a larger margin to adjust the turn number. According to Table 3-3, the flux density at the maximum voltage is 0.31 T which can be increased to 0.54 T if the primary turn number is reduced from 7 turns to 4 turns. Consequently, the secondary turn number will decrease down to 33 turns to bring the copper loss down.

Although served Litz wires are used in the prototype transformers, the copper loss is considerably greater than the prediction. This is due to the skin effect and the proximity effect. Moreover, the predicted core loss is also smaller than the measurements due to the non-sinusoidal flux density in practice. To improve the loss prediction, Dowell's formula for approximation of the AC resistance and improved general Steinmetz equation should be incorporated in the design [48].

The nanocrystalline transformers have the efficiency and power density better than the ferrite transformer as expected. This is due to its lower core loss and its higher flux density. Relatively small cores can be used. Consequently, it decreases the winding volume so that copper loss can also be decreased. Although the toroid nanocrystalline transformer B has lowest core loss, the overall loss is overshadowed by the nanocrystalline transformer C, which is constructed from 2 pairs of cut C-cores. This due to winding configuration of the toroid that requires a relatively longer wire. For the transformer C, the shell type construction, which is compact around the core in the middle, requires a shorter wire. Although the transformer C draws a relatively large magnetizing current, it seems to have a slight impact on the total loss. Moreover, cut C-cores are more suitable for high power applications. The two nanocrystalline transformers have the efficiency close to the literature which was designed at 1 kVA 1 kHz with the efficiency of 99.1% [49].

Table 4-1 Experimental results of the prototype transformers

Parameters	Transformer A	Transformer B	Transformer C
Material	Ferrite N87	Nanocrystalline King Magnetics	Nanocrystalline MK Magnetics
Nominal power at 48 V	1,054 W	1,170 W	1,132 W
Maximum power at 54 V	1,201 W	1,230 W	1,277 W
Power density	6 W/cm^3	12 W/cm^3	9 W/cm^3
Total loss at nominal power	24.2 W	17.3 W	16.3 W
Core loss at nominal power	5.0 W	1.9 W	3.5 W
Copper loss at nominal power	19.2 W	15.4 W	12.8 W
Efficiency at nominal power	97.8%	98.5%	98.6%
Maximum efficiency	98.8%	99.2%	99.1%
Minimum efficiency	97.6%	97.6%	98.4%
Maximum temperature	78.5°C	60.1°C	71.0°C

Chapter 5
Conclusion

5.1 Conclusion of the Findings

This research investigates application of high frequency magnetic materials for a dual active bridge (DAB) DC-DC converter. This converter is designed for connecting a home battery storage with the input voltage ranges from 42 V to 54 V. to a constant DC bus voltage of 400 V. The nominal power of the prototype is 1.1 kW with a peak power of 1.2 kW with the switching frequency of 20 kHz. A high frequency transformer plays important roles in adjust the voltage levels and in transferring power bidirectionally between the two sides.

MnZn ferrite model N87 from TDK was selected for construction a 20-kHz transformer and auxiliary inductor for the DAB DC-DC converter. A 48V/400V 1.2-kVA 20-kHz was built on a pair of EE65 N87 ferrite cores. Two transformers with the same specification as the ferrite transformer were constructed from tape wound nanocrystalline cores. The first nanocrystalline transformer was built on a KMN503220T toroidal core from King magnetics, a china-based company. Another nanocrystalline transformer was assembled from 2 sets of cut c-cores SC2043M1 from MK magnetics, a US-based company (equivalent to Hitachi Finemet F3CC0.63). Served Litz wires were used as the windings of the transformers.

The nanocrystalline transforms were found to efficiency and power density better than the ferrite transformer. The cut C-core nanocrystalline transformer has efficiency between 98.4% to 99.1% with the nominal power density of 9 W/cm^3. The maximum operating temperature of 71.0°C. The toroidal nanocrystalline transformer has the efficiency range of 97.6%-99.2%, the power density of 12 W/ cm^3 and the maximum operating temperature of 60.1°C. The efficiency range, power density and the maximum operating temperature of the ferrite transformer were found to be 97.6%-98.8%, 6 W/ cm^3, and 78.5°C respectively.

Tape wound nanocrystalline materials have core loss and maximum flux density relatively better than ferrite materials. Tape wound nanocrystalline materials not only reduce the core loss, but also decrease the copper loss due to smaller copper windings. Nanocrystalline cut C-cores is suitable for high power applications due to the increased efficiency and ease of transform manufacturing.

5.2 Future Works

1) Improve design methodology of the transformers and inductors.
2) Thoroughly study the transformer and inductor losses under the unified phase shift modulation to allow an efficiency optimized operation.

References

[1] R. H. Lasseter, "Smart Distribution: Coupled Microgrids," *Proceedings of the Ieee,* vol. 99, pp. 1074-1082, 2011.

[2] V. A. Boicea, "Energy Storage Technologies: The Past and the Present," *Proceedings of the Ieee,* vol. 102, pp. 1777-1794, 2014.

[3] A. G. Boulanger, A. C. Chu, S. Maxx, and D. L. Waltz, "Vehicle Electrification: Status and Issues," *Proceedings of the IEEE,* vol. 99, pp. 1116-1138, Jun 2011.

[4] M. Falahi, H. M. Chou, M. Ehsani, L. Xie, and K. L. Butler-Purry, "Potential Power Quality Benefits of Electric Vehicles," *IEEE Transactions on Sustainable Energy,* vol. 4, pp. 1016-1023, 2013.

[5] M. Kezunovic, J. D. McCalley, and T. J. Overbye, "Smart Grids and Beyond: Achieving the Full Potential of Electricity Systems," *Proceedings of the IEEE,* vol. 100, pp. 1329-1341, May 2012.

[6] D. o. A. E. D. a. Efficiency, "Alternative Energy Development Plan: AEDP2015," 2015.

[7] M. o. Energy, "Thailand Smart Grid Master Plan (2015-2036)," 2015.

[8] M. Liserre, T. Sauter, and J. Y. Hung, "Future Energy Systems: Integrating Renewable Energy Sources into the Smart Power Grid Through Industrial Electronics," *IEEE Industrial Electronics Magazine,* vol. 4, pp. 18-37, 2010.

[9] B. M. Grainger, G. F. Reed, A. R. Sparacino, and P. T. Lewis, "Power Electronics for Grid-Scale Energy Storage," *Proceedings of the Ieee,* vol. 102, pp. 1000-1013, 2014.

[10] R. W. A. A. De Doncker, D. M. Divan, and M. H. Kheraluwala, "A three-phase soft-switched high-power-density DC/DC converter for high-power applications," *IEEE Transactions on Industry Applications,* vol. 27, pp. 63-73, 1991.

[11] M. N. Kheraluwala, R. W. Gascoigne, D. M. Divan, and E. D. Baumann, "Performance characterization of a high-power dual active bridge DC-to-DC converter," *IEEE Transactions on Industry Applications,* vol. 28, pp. 1294-1301, 1992.

[12] Y. A. Harrye, K. H. Ahmed, and A. A. Aboushady, "DC fault isolation study of bidirectional dual active bridge DC/DC converter for DC transmission grid application," in *Industrial Electronics Society, IECON 2015 - 41st Annual Conference of the IEEE*, 2015, pp. 003193-003198.

[13] S. Xu, A. Q. Huang, and R. Burgos, "Review of Solid-State Transformer Technologies and Their Application in Power Distribution Systems," *IEEE Journal of Emerging and Selected Topics in Power Electronics,* vol. 1, pp. 186-198, 2013.

[14] X. Lingxiao, D. Diaz, S. Zhiyu, L. Fang, P. Mattavelli, and D. Boroyevich, "Dual active bridge based battery charger for plug-in hybrid electric vehicle with charging current containing low frequency ripple," in *Anual IEEE 28th Applied Power Electronics Conference and Exposition (APEC)*, 2013, pp. 1920-1925.

[15] S. Inoue and H. Akagi, "A Bidirectional DC-DC Converter for an Energy Storage System With Galvanic Isolation," *IEEE Transactions on Power Electronics,* vol. 22, pp. 2299-2306, 2007.

[16] N. H. Baars, J. Everts, H. Huisman, J. L. Duarte, and E. A. Lomonova, "A 80-kW Isolated DC-DC Converter for Railway Applications," *IEEE Transactions on Power Electronics,* vol. 30, pp. 6639-6647, Dec 2015.

[17] F. Z. Peng, L. Hui, S. Gui-Jia, and J. S. Lawler, "A new ZVS bidirectional DC-DC converter for fuel cell and battery application," *IEEE Transactions on Power Electronics,* vol. 19, pp. 54-65, 2004.

[18] M. Cacciato, A. Consoli, R. Attanasio, and F. Gennaro, "Soft-switching converter with HF transformer for grid-connected photovoltaic systems," *IEEE Transactions on Industrial Electronics,* vol. 57, pp. 1678-1686, 2010.

[19] B. Zhao, Q. Song, W. Liu, and Y. Xiao, "Next-Generation Multi-Functional Modular Intelligent UPS System for Smart Grid," *IEEE Transactions on Industrial Electronics,* vol. 60, pp. 3602-3618, 2013.

[20] A. K. Jain and R. Ayyanar, "PWM Control of Dual Active Bridge: Comprehensive Analysis and Experimental Verification," *IEEE Transactions on Power Electronics,* vol. 26, pp. 1215-1227, Apr 2011.

[21] G. G. Oggier, G. O. Garc, and A. R. Oliva, "Switching Control Strategy to Minimize Dual Active Bridge Converter Losses," *IEEE Transactions on Power Electronics,* vol. 24, pp. 1826-1838, 2009.

[22] G. Oggier, G. O. Garc, x00Ed, and A. R. Oliva, "Modulation strategy to operate the dual active bridge DC-DC converter under soft switching in the whole operating range," *IEEE Transactions on Power Electronics,* vol. 26, pp. 1228-1236, 2011.

[23] H. Bai and C. Mi, "Eliminate Reactive Power and Increase System Efficiency of Isolated Bidirectional Dual-Active-Bridge DC-DC Converters Using Novel Dual-Phase-Shift Control," *IEEE Transactions on Power Electronics,* vol. 23, pp. 2905-2914, 2008.

[24] B. Zhao, Q. Song, and W. Liu, "Power Characterization of Isolated Bidirectional Dual-Active-Bridge DC-DC Converter With Dual-Phase-Shift Control," *IEEE Transactions on Power Electronics,* vol. 27, pp. 4172-4176, 2012.

[25] F. Krismer and J. W. Kolar, "Accurate Small-Signal Model for the Digital Control of an Automotive Bidirectional Dual Active Bridge," *IEEE Transactions on Power Electronics,* vol. 24, pp. 2756-2768, 2009.

[26] F. Krismer and J. W. Kolar, "Closed Form Solution for Minimum Conduction Loss Modulation of DAB Converters," *IEEE Transactions on Power Electronics,* vol. 27, pp. 174-188, 2012.

[27] H. Zhou and A. M. Khambadkone, "Hybrid Modulation for Dual-Active-Bridge Bidirectional Converter With Extended Power Range for Ultracapacitor Application," *IEEE Transactions on Industry Applications,* vol. 45, pp. 1434-1442, 2009.

[28] B. Zhao, Q. Song, and W. Liu, "Experimental Comparison of Isolated Bidirectional DC–DC Converters Based on All-Si and All-SiC Power Devices for Next-Generation Power Conversion Application," *IEEE Transactions on Industrial Electronics,* vol. 61, pp. 1389-1393, 2014.

[29] D. Aggeler, J. Biela, S. Inoue, H. Akagi, and J. W. Kolar, "Bi-Directional Isolated DC-DC Converter for Next-Generation Power Distribution - Comparison of Converters using Si and SiC Devices," in *Power Conversion Conference - Nagoya, 2007. PCC '07*, 2007, pp. 510-517.

[30] B. Zhao, Q. Song, W. Liu, and Y. Sun, "A Synthetic Discrete Design Methodology of High-Frequency Isolated Bidirectional DC/DC Converter for Grid-Connected Battery Energy Storage System Using Advanced Components," *IEEE Transactions on Industrial Electronics,* vol. 61, pp. 5402-5410, 2014.

[31] C. H. Zhao, S. D. Round, and J. W. Kolar, "An Isolated Three-Port Biodirectional DC-DC Converter With Decoupled Power Flow Management," *IEEE Transactions on Power Electronics,* vol. 23, pp. 2443-2453, Sep 2008.

[32] G. Waltrich, M. A. M. Hendrix, and J. L. Duarte, "Three-Phase Bidirectional DC/DC Converter With Six Inverter Legs in Parallel for EV Applications," *IEEE Transactions on Industrial Electronics,* vol. 63, pp. 1372-1384, 2016.

[33] T. Mori, K. Igarashi, K. Kanagawa, N. Yamashita, T. Shimizu, and Y. Bizen, "Iron loss evaluation of iron powder core suitable for inductor used in power converters," in *2014 International Power Electronics Conference (IPEC-Hiroshima 2014 - ECCE ASIA)*, 2014, pp. 2983-2987.

[34] M. Rafiq, F. Mohammed, M. Yaqoob, and T. Thiringer, "Analysis of power losses and efficiency up to 60 kW DC-DC converter for hybrid electric vehicle with different inductive core materials," in *2013 IEEE International Symposium on Industrial Electronics*, 2013, pp. 1-5.

[35] M. S. Rylko, J. G. Hayes, and M. G. Egan, "Experimental investigation of high-flux density magnetic materials for high-current inductors in hybrid-electric vehicle DC-DC converters," in *2010 IEEE Vehicle Power and Propulsion Conference*, 2010, pp. 1-7.

[36] A. M. Leary, P. R. Ohodnicki, and M. E. McHenry, "Soft Magnetic Materials in High-Frequency, High-Power Conversion Applications," *JOM,* vol. 64, pp. 772-781, 2012.

[37] E. AG., *Ferrite material N95 boosts the efficiency of power supplies*, 2009.

[38] H. Metals, *Metglass® AMCC Series Cut Core and FINEMET® F3CC Series Cut Core*, 2017.

[39] S. Inoue and H. Akagi, "A bidirectional isolated DC-DC converter as a core circuit of the next-generation medium-voltage power conversion system," *IEEE Transactions on Power Electronics,* vol. 22, pp. 535-542, Mar 2007.

[40] W. T. McLyman, *Transformer and Inductor Design Handbook*, 3rd ed. New York: Marcell Dekker, 2006.

[41] R. W. Erickson and D. Maksimovic, *Fundamentals of Power Electronics*, 2nd ed. New Youk: Kluwer Academic, 2001.

[42] E. AG., *Ferrites and accessories SIFERRIT material N87*, 2006.

[43] K. Magnetics, *Nanocrystalline and Amorphous Cores and Components*, 2017.

[44] V. GmbH&AG, *VITROPERM 500 F and VITROVAC 6030 F Tape-Wound Cores in Power Transformers for Switched Mode Power Supplies*, 2003.

[45] H. Metals, *FINEMET® F3CC Series Cut Core*, 2017.

[46] M. Magnetics, *Tape Wound Core Specialist*, 2017.

[47] [Online]. Available: http://www.bodepower.com/portable-generator-gasoline-generator-set-bge3500/

[48] W. G. Hurley and W. H. Wofle, *Transformers and Inductors for Power Electronics-Theory, design and applications*. Chichester, United Kingdom: Wiley, 2013.

[49] D. Ruiz-Robles, J. Ortíz-Marín, V. Venegas-Rebollar, E. L. Moreno-Goytia, D. Granados-Lieberman, and J. R. Rodríguez-Rodriguez, "Nanocrystalline and Silicon Steel Medium-Frequency Transformers Applied to DC-DC Converters: Analysis and Experimental Comparison," *Energies,* vol. 12, p. 2062, 2019.